1-1-1981

Investigation of vortical motions in the inner region of a turbulent boundary layer.

Stuart Philip Schwartz

INVESTIGATION OF VORTICAL MOTIONS IN THE INNER REGION OF A TURBULENT BOUNDARY LAYER

BY

STUART PHILIP SCHWARTZ

A THESIS

PRESENTED TO THE GRADUATE COMMITTEE

OF LEHIGH UNIVERSITY

IN CANDIDACY FOR THE DEGREE OF

MASTER OF SCIENCE

IN

MECHANICAL ENGINEERING

LEHIGH UNIVERSITY

1981

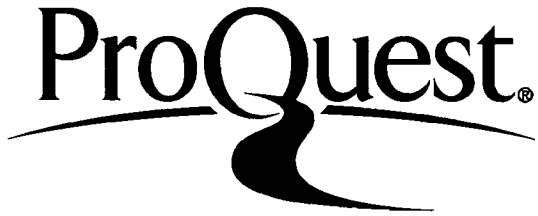

This thesis is accepted and approved in partial fulfillment of the requirements for the degree of Master of Science.

7 May 1981
(Date)

Professor in Charge

Chairman of Department

ACKNOWLEDGEMENTS

I would like to sincerely thank Dr. Charles Smith for allowing me to demonstrate and expand my working and learning ability; I hope I have fulfilled his expectations. His monumental patience and acute knowledge of teaching provided me with much valuable knowledge, a respect for research in general, and for the complexity of turbulence studies.

The efforts of Steve Metzler and Tony Cerra, who were responsible for much of the construction of the laboratory facilities, is sincerely appreciated.

Also instrumental in the completion of this project are my wife, Laurie, and the rest of my family who showed considerable patience while this paper was being written.

The craftsman who helped in the construction of much of the facility contributed considerably to the project. Thanks to Fred Wehden, Dick Towne, and Jim Bunderla, who were involved in actual construction, and who answered many questions thus making my job easier. Thanks also to Tim Nixon for providing the instrumentation and electronics.

I also greatly appreciate and respect the Word Processing Department of Fuller Company for being

able to read the hieroglyphics given to them and making it all look good on paper.

Of utmost importance was the interest of the Air Force Office of Scientific Research in boundary layer studies which stimulated the funding of this project. Their funding was under contract number F49620-78-C-0071.

TABLE OF CONTENTS

LIST OF TABLES

LIST OF FIGURES

LIST OF SYMBOLS

C	Location of vortex center determined by direction visualization.
C_{est}	Location of vortex center determined by indirect method.
CRAV	Counter-rotating Axial Vortices (abbreviation).
D	Diameter.
D_{core}	Diameter of vortex core.
$D_{app.}$	Apparent diameter outside of core.
f	Frequency.
L	Characteristic length.
Re_{θ}	Reynolds number based on momentum thickness.
r	Radius.
r_a	Apparant radius.
r_c	Radius of vortex core.
t	Time.
u,v,w	Velocity components in x,y,z directions.
U_{∞}	Free stream velocity.
U_{τ}	Shear velocity ($\sqrt{\tau_w/\rho}$).
$V_{\theta c}$	Tangential velocity of vortex core.
$V_{\theta o}$	Tangential velocity outside of vortex core.
x,y,z	Spatial coordinates in axial, normal, and lateral direction with respect to U_{∞}.

Greek Symbols

Γ	Circulation strength.
Δ	Designates increment or change in a unit (e.g. Δt).
θ	Angle of rotation.
μ	Absolute viscosity.
ν	Kinematic viscosity.
ρ	Density.
σ	Standard deviation.
τ_w	Wall shear stress.
$\omega_x, \omega_y, \omega_z$	Vorticity in x,y,z directions.
Ω	Rotational speed.

Superscripts

$+$	Designates dimensionless unit (e.g. t^+).
$-$	Designates mean average (e.g. $\bar{C}^+$).

ABSTRACT

Detailed flow visualization studies of axial vortex motions in the wall region of turbulent boundary layers have been done in an open surface water channel using specially designed hydrogen bubble wire probes and a dual-view (underwater end-view and top-view) high speed video system. Observations were done for $1020 < Re_\theta < 2200$ and $y^+ < 60$, with quantitative characteristics of axial flow structure determined from the recorded visualization data.

Observations show the definite existence of axial vortices possessing highly rotational characteristics. Up to 40% of all detected axial flow structures were determined to be definitely rotating structures. The remainder of the detected axial structures were either upwellings and/or downward motions, which are speculated to be the resultant effect caused by the interaction of the rotating structures with fluid near the plate surface. Observations show that pairs of counter-rotating axial vortices appear quite frequently in the detected structures. The spacing between these counter-rotating axial vortices appears to be a minimum at $22 < y^+ < 26$ which is also the most frequently observed location of vortex centers. Direct visualiza-

tion yielded vortex core sizes between 15 and 26 dimensionless units. The circulation strength appears to increase with both distance from the surface and vortex diameter; this is hypothesized to be due to vortex coelescence.

Transverse vortices appeared to have circulation strength consistent with that of the axial vortices. As a result, a stretched and lifted loop vortex model is hypothesized which is consistent with observations of the present investigation. Several observations are made which support this loop vortex hypothesis including the lifting of low speed fluid from the wall region and the induced flow of higher speed fluid toward the wall. This higher speed fluid, as it decelerates due to interaction with the wall, is speculated to provide the source of fluid for low speed streak reinforcement and/or formation, while the lifting of the low speed fluid away from the wall and subsequent interaction with outer region fluid is speculated to be responsible for subsequent loop vortex formation.

SECTION 1

INTRODUCTION AND OBJECTIVES

The beginning of serious studies of turbulent flow is attributed to Osborn Reynolds, who circa 1880, made monumental contributions to this field (see Rubesin, 1978). However, the most important achievement in viscous flow theory was the discovery of the boundary layer by Prandtl in 1904 (see White, 1974). The boundary layer is normally very thin and thus quantitative information is difficult to obtain. The measuring devices are large compared to the boundary layer, thereby compounding the measurement problem. Many measurement techniques have been employed in boundary layer studies including flow visualization, hot film and hot wire anemometry, and laser doppler techniques (some of these will be discussed in detail in a later section). However, despite the vast use of technological innovations which have yielded much valuable information, we still presently lack a complete understanding of the physical phenomena occurring in the turbulent boundary layer.

A major breakthrough occurred in 1956 when Townsend (1956) hypothesized that large, relatively

coherent structures of the boundary layer play a dominant role in maintaining shear flow turbulence. He recognized the importance of the interaction between the inner and outer regions within the boundary layer. According to Townsend's model (see Figure 1), the boundary layer can be divided into two parts: (1) the inner layer where most turbulence production occurs, but is nearly in energy equilibrium, and (2) the outer layer which derives most of its turbulent energy via transport from the inner layer. He based this energy transport theory on the fact that the local production of energy in the outer layer is too small to balance the local viscous dissipation and losses by transport. Townsend finally concluded that two distinct processes make up the interaction between the inner and outer layers of the flow: (1) the transport of mean flow energy from the outer layer to the inner layer at a rate controlled by the gradient of the Reynolds stress in the outer layer, and (2) the transport of turbulent energy from the inner layer to the outer layer.

Townsend's theory led to a division between fluid mechanicians regarding the roles of the inner and outer layers. The three groups of thought could be categorized as: (1) believers that the outer layer dominates the boundary layer occurrences (i.e., the

outer layer occurrences drag the inner layer along), (2) believers that the inner layer dominates (i.e., inner layer occurrences drive the outer flow) and (3) believers that the interaction between the inner and outer layer is a cyclical, complementary process. A few of those who speculate that the outer layer behavior dominates are Willmarth and Tu (1967), Praturi and Brodkey (1978), Blackwelder (1978), and Rao (1971). A belief in inner layer domination has been expressed by Einstein and Li (1957), Hanratty (1956), and Offen and Kline (1973). Kline (1978) has shown, however, using a "negative inference" technique, that the mutual interaction between both inner and outer layers is necessary for continued turbulence production. Most of the controversy over which region dominates involves a sequence of events in which "bursting" events and sweeps events occur. At a workshop on Coherent Structures of Turbulent Boundary Layers held at Michigan State University in 1979, it was generally agreed upon that the inner and outer layers interact and that available data eliminates the hypothesis asserting either inner or outer domination (see Kline and Falco, 1979).

Several important discoveries regarding the structure of turbulent flow must be discussed to set

the stage for a further discussion on this split in theories regarding inner or outer layer domination. Beatty, Ferrell, and Richardson (1955), employing a dye solution pumped through a pipe, showed that residual dye near the wall of the pipe formed into filaments aligned in the streamwise direction. This streaky structure was soon confirmed in the transition experiments of Hama (1956) in which he used dye injection through slots cut into the wall. The streaky structures became commonly known as low speed streaks.

As technological sophistication increased, more experiments were performed concerning the structure of turbulent boundary layers. Runstadler et al (1959 and 1963) proposed a model based on visual observations of dye and hydrogen bubble generation. Similar findings of Schraub and Kline (1965) confirmed Runstadler's model which involved the presence of a coherent, time-dependent, streaky structure in the wall region which interacts with turbulent fluid outside the wall layer (see Figure 2). The wall layer was shown to consist of a relatively regular structure of low and high speeds streaks alternating in the spanwise direction over the entire wall (Runstadler, et al 1959, 1963). This streaky structure has been described as a weak, secondary, longitudinal vorticity (Runstadler, et al 1959, 1963).

Kline's (1967) model (Figure 3) relates the streaks and longitudinal vorticity, and is called the stretched and lifted vortex theory. The model is:

1. Formation of low speed streaks with a dimensionless spacing in the spanwise direction of $\Delta z^+ \cong 100$. This streak formation is speculated to be caused by counterrotating longitudinal vortices which move fluid to and from the wall between pairs of the vortices. The streaks are observed to be uniformly distributed across the flow.
2. The low speed streak lifts-up from the wall causing an unstable inflectional velocity profile.
3. The lifted streak begins to oscillate and wavy motion becomes evident.
4. This wavy motion leads to the break-up of the coherency of the streak.

The above findings have laid the ground work for much of the research in the past fifteen years. It is this bursting process which observers have tried to correlate with subsequent experimental results to determine what role the burst and streak play in inner-outer layer behavior.

Lu and Willmarth (1973, see Willmarth, 1975) conducted conditional sampling experiments of wall pressure behavior below a turbulent boundary layer. They speculated that inertial forces near the wall are sufficiently small such the important terms of the momentum equation become the pressure gradient and stress terms. Therefore, the fluid near the wall should be caused to move outward (burst sequence) as a result of convected large scale vorticity in the outer layer which creates local adverse and favorable pressure gradient condition. These traveling pressure gradients, it is further believed, actually push the slow moving fluid in the sublayer about. Note that Rao, et al (1971), showed that the burst frequency scales with outer flow variables, δ and U_∞. Laufer and Narayanan (1971) also found the bursting frequency approximately the same as the frequency of passage of a large scale structure in the outer region. The fact that the non-dimensional period, $U_\infty \bar{T}/\delta$, is independent of Reynolds number Re_θ, was the main argument for scaling the burst frequency with the outer flow variables.

Other observers such as Brodkey (1978), and Praturi and Brodkey (1978) hypothesize that the outer region is dominant and that the streamwise vortices in Kline's model (1967) are short lived compared to the

outer region transverse vortical motion. Using anemometry and stereoscopic visualization, Brodkey proposes a model in which the streamwise and transverse vortices in the wall region appear to be the result of the shear zone at the front between the wallward moving high speed fluid and the trapped, but outflowing, low speed fluid moving around the "fingers" of a high speed front. This is in direct contrast to several other models (to be discussed) which presume the axial (streamwise) vortex pairs are the cause of the outflow of low speed fluid. Praturi and Brodkey go on to state that the outer region motions give rise to the conditions necessary for the dominant wall region activity of ejections and axial vortex motions. Figure 4 represents Praturi and Brodkey's interpretation of the events occurring in the boundary layer.

Nychas et al (1973) photographed suspended solid particles in the outer region. He observed that the most important event was a transverse vortex due to an instability interaction between accelerating and decelerating fluid, and that the vortex is associated with the wall region ejection. Could this transverse vortex be caused by the ejection of low speed fluid into the outer region causing lower momentum fluid to retard higher momentum fluid thus resulting in the

development of a free shear layer? Smith (1978) suggests that the passing of a large scale motion (possessing transverse rotation) seemed to initiate an upwelling from the wall region, which is fed with fluid both from upstream and from the wall region. As this upwelling is formed, it could be observed to interact with thick, long vortices which could be traced up from the wall to large scale motions as far from the wall as $y^+ \cong 300$. It was speculated that these longitudinal vorticies are connected with large transverse vortices observed in the outer region.

Nychas, however, goes on to observe that the transverse vortices induce outflow conditions at the wall and that streamwise vortices as such were not observed. Nychas' experiment was set up for outer region analysis, but he claims that the inner region was also observable. Perhaps the inner region was not as clearly visible as necessary in order to detect axial vortices.

Offen and Kline (1973 and 1974) used a combination of dyed fluid at the wall of one color, hydrogen bubbles (vertical wire), and another color dye above the wall to observe the interaction between the inner and outer parts of the boundary layer. This interaction was explained in terms of vorticity and, from another

point of view, in terms of pressure-velocity interactions. The vorticity produced during the bursting sequence was observed to emerge from the wall region as it is carried downstream. This vorticity often interacted with other similar accumulations of vorticity to make larger accumulations of vorticity. These larger accumulations were found in the outer wall region. They proposed that the slow speed streaks acts as a boundary layer within a boundary layer and lift-up occurs due to a temporary local adverse pressure gradient being imposed on the streak. Offen and Kline further speculate that this pressure gradient is in some way connected with a wallward moving disturbance that originates in the logarithmic region ($y^+ > 30$-40, but less than the wake matching point) of the boundary layer. This wallward moving disturbance is termed the sweep. As the sweep reaches the wall, it spreads out sideways and is retarded. Sometimes when the high speed fluid moves toward the wall downstream of the outward moving low speed fluid, a transverse vortex results. A new low speed streak is formed by the arriving fluid. The lifted fluid finds its way back to the wall from some region farther away from the wall and a new adverse pressure gradient results and causes another lift-up.

Two types of vortical motions are believed to be connected in some way to the bursting phenomonon and to streak formation. These vortical motions are those described by Kline (1967) as longitudinal vortices and those presented by Offen and Kline (1973) as transverse vortices. The relative importance of each type of vorticity as well as their connection, if any, to a specific flow phenomena and each other is still unclear.

Bakewell and Lumley (1967) proposed a definition of a large Eddy based on orthogonal decomposition of the turbulent velocity field. The dominant structure, within the wall region, according to their model, consists of randomly distributed counter-rotating eddy pairs of elongated streamwise extent whose evolution and destruction are governed by nonlinear mechanisms of vortex stretching. Further, they found that most energetic velocity fluctuations were consistent with axial vortices. Lee, Eckelmann, and Hanratty (1974) arrived at similar conclusions using the regular quasi-periodic variations of the velocity gradients at the wall.

Turbulence generation in the wall region was investigated using pressure-velocity and velocity-velocity correlations by Tu and Willmarth (1966). In their proposed model, they view the wall region as a turbulence

generation region filled with random vortex lines. Strong shear layers develop as a result of these vortex lines and are believed to eventually become unstable and break up. This mechanism serves to produce turbulence. Further, the pattern of lift-up of the low speed streaks from the inner layer (sublayer as Tu and Willmarth call it) is regarded merely as vortex stretching. They feel this explains the strong concentration of both mean and fluctuating vorticity near the wall found by Kline (1967), and Corino and Brodkey (1969).

Tu and Willmarth (1966) measured the correlation between streamwise velocity at a fixed point near the wall just outside the "sublayer" and streamwise vorticity at various points. They used a probe consisting of four hot wires, but the probe was too large to detect small scale vorticity in the sublayer. However, they did conclude that downstream of the point where streamwise velocity was measured, there was an antisymmetric pattern of highly sweptback streamwise vorticity emanating outward from the wall. These findings are consistent with Figure 3 where ω_x (streamwise vorticity) emerges outward from the wall.

Utilizing the above findings, Tu and Willmarth speculate:

> "the evidence indicates that the burst mechansim consists initially of a pair of counterrotating vortices with primarily a streamwise vorticity component that are stretched during the lift-up phase of the bursting process."

As such a vortex pair moves away from the wall, they will be convected downstream more and more rapidly as their distance from the wall increases. The result would be a severe stretching of the vortex pair, with a correspondingly rapid increase in vorticity which will cause an even more rapid movement from the wall. This is suggested as the fundamental process involved in the last stage of the burst sequence, i.e., the ejection phase.

Some observers have attempted to find the connection between the transverse vorticity and the longitudinal vorticity. The sublayer streaks of Kline (1967) and Schraub (1965) are believed to be formed by streamwise vorticity and have been observed as close as $y^+ = 15$ with hydrogen bubbles and $y^+ = 0$ with wall dye slot injection. Streamwise vortices and sometimes transverse vortices are often associated with lifted low speed streaks. As was previously mentioned, Kline speculates that the low speed streak lift-up is actually a result of streamwise vorticity. Further, it was speculated that the upward tilted streamwise vortices

have their origin in the transverse vortices that have formed and lifted off the wall by some perturbation, and stretched in the shear flow. However, it is important to keep in mind that the connection made here between the transverse vortices and axial vortices along the wall as well as the upward tilted vortices is not definite.

Kim, et al (1971) similarly conclude that the lifting of low speed streaks is slow and over a large length since streamwise vorticity is small at first, i.e., outward motion is a cumulative effect over long distances of small streamwise vortices. When the slowly lifting streak reaches a critical distance from the wall, it turns away more sharply (see Figure 5). Kim conceives the dominant mode in a description of the oscillatory growth stage (see Kline 1967) of the bursting process is streamwise vortex motion in which the vortex size grows and its strength increases as the motion proceeds downstream. Two less common modes of oscillatory growth were also reported by Kim: (1) a transverse vortex and (2) repeated oscillation he calls wavy motion. Although no quantitative investigation was made of the vortex dynamics, Kim notes that streamwise vortex size and rotational speed both increased simultaneously; therefore, vortex stretching, which requires

an increase in rotational speed as diameter decreases, is not the only mechanism at work. He believes that some kind of energy is being transmitted to the vortex, but this was not investigated.

Kim et al (1968) drew attention to the similarities between free shear layer type velocity profiles in turbulent boundary layers (i.e., the inflection points in longitudinal profiles due to low momentum fluid lift-up obstructing the higher velocity outer flow) and those occurring during laminar to turbulent boundary layer transition. Hama and Nutant (1963), using the hydrogen bubble technique, studied the transition process and found that an originally two dimensional wave warps its front, acquiring longitudinal vorticity which forms into a Λ-shaped vortex (as Hama calls it) open at its tip (i.e., downstream; closed end of the vortex). This vortex structure is further observed to create a strong upward fluid motion inside its legs. A high shear layer results and breaks down to form a secondary Λ-shaped vortex of great concentration. The secondary vortex develops into a Ω-shaped vortex which is "snatched" away from the main body of the Λ-vortex. It was noted by Hama that a tertiary Λ-vortex forms following the secondary vortex formation. It is these

three instabilities which Kim compared to streamwise and spanwise vortices of free shear layer flow.

Offen and Kline (1973) believe that the dye and bubble patterns observed in their pictures combined with the conditionally processed results from anemometer experiments suggest that the three kinds of oscillatory growth reported by Kim (1971) are associated with just one type of flow structure . . . the stretched and lifted vortex described by Kline (1967). The streamwise and transverse vortical patterns are conceived of as the passage of different portions of the stretched and lifted vortex. They further suggest that large scale motions in the outer layer are a consequence of vortices, associated with bursts, pairing as they move into the outer region.

An investigation to determine the connection between the bursting phenomenon and large scale motions in the outer region was done by Brown and Thomas (1977). This work is discussed here because the observers speculate as to the origin of longitudinal vorticity in the wall region. Using hot film anemometry and wall shear stress probes, Brown and Thomas describe a bursting model in terms of a rotational instability. The model (see Figure 6) represents a stretched horseshoe vortex in a moving reference frame (moving at .8 U_∞). Region

A is believed to be the origin of longitudinal vorticity in the wall region and assists in "breakup" of the burst cycle at higher Reynolds numbers. They note that this a secondary flow is similar to Taylor vortices between rotating cylinders or Görtler vortices in a boundary layer on a concave surface. They further suggest that as the longitudinal vorticity is convected into Region B, longitudinal straining motion will intensify the vorticity and return it toward the wall thereby assisting in the formation of a new streak. It is questionable, to the author, how this straining motion would cause the vorticity to return to the wall. During vortex stretching, one would expect the vortices to indeed become intensified, but from the model shown in Figure 6, mutual inductance would cause the vorticity to move away from the wall. (Willmarth (1975) points this out also.)

The horseshoe vortex model has been presented by many observers as a model for a key structure in the wall region of a turbulent boundary layer, and thus far there has yet to be found evidence contradicting such a model. Several investigations have provided more data regarding such a structure and have drawn a more detailed picture of the horseshoe vortex structure and its connection with other flow phenomena.

Smith (1978) notes that the lift-up of a streak is believed to be connected with a concave forward front which sweeps across the streak and eliminates it (Figure 7). It was speculated that the flow pattern resulting from a vortex loop lift-up induces a retardation of fluid at the surface and the front subsequently is formed. The formation of the front is preceded by an influx of outer region fluid toward the wall. Of importance, are the "kinked" regions, as Smith calls them (refer to Figure 7), trailing the front. These kinked regions which move toward each other, as the initial streak was eliminated by the front, are the result of counterrotating axial vortices. "Note that these counterrotating longitudinal vortices are essentially the 'legs' of the lifted vortex-loop model of a burst proposed by Offen and Kline (1973)." The fact that the vortices move together supports Willmarth's (1975, see Figure 8) idea of mutual inductance, which would result in the vortices moving together and away from the wall. Combined with vortex stretching effects due to the strong velocity gradient near the wall, this mutual inductance may strongly contribute to the bursting phenomenon or may actually be the bursting phenomenon. The convergence of these side portions appeared, as seen by Smith, to form a new streak. The

streak, it was pointed out, seems to become more concentrated due to stretching and intensification of the longitudinal vortices. The longitudinal vortices appear to originate near the plate surface, with the diameters of the vortices increasing and angular velocity decreasing as the vortices move away from the wall.

Another experimentalist, Falco (1977), using oil fog visualization, has observed flow modules he calls "pockets." These fluid motions were observed to be more vigorous than those associated with the streaky structures. Falco says that the wavy motion and break-up of streaks was a result of their being pushed around by the pockets. He showed that vortex ring-like Eddies (created by the turbulent wake of a shedding cylinder) could be observed to cause pocket-like structures to form in a laminar boundary layer. However, it has yet to be shown that similar Eddies can cause pockets to form in a turbulent boundary layer. It is speculated by Falco that the pocket could be the result of wall layer and outer layer interactions (i.e., high speed fluid approaching the wall). Of importance to the present investigation, is that Falco states that the pockets appeared to evolve into a pair of streamwise vortices each of which results in lift-up of sublayer fluid. Figure 9 shows Falco's speculation of how "a

fully developed pocket has a stretched laminar vortex tube which can be seen to extend from one side, around its upstream boundary to the other side." The side (streamwise) vortices revolve as a counterrotating pair and bring fluid towards the wall between them and away from the wall outside the pocket. It is interesting to note that a pair of counterrotating axial vortices is not necessary to move fluid away from the wall as suggested by Smith (1978), Kline (1967), and others.

Falco believes that the formation of the pockets is the origin of the turbulence production process and it is not the disturbance of the long streaky structure which initiates the production process. The streaks appear to be remnants of previous pocket evolutions. Vortex stretching and vortex/wall interactions were believed by Falco to be dominant mechanisms not shear layers and their instabilities.

Several experiments have been cited which attempted to resolve the uncertainity regarding inner and outer layer interactions. Axial vorticity is a factor in most of the descriptions of the bursting and streak phenomena. Some experimentalists have investigated the axial vortices in hopes of gaining more quantitative, as well as qualitative information about the vortices.

Brodkey's (1978) films yielded some quantitative information as to the location of axial vortices. The axial vortices he states, were always very close to the wall. They were closer than a $y^+ \cong 25$ to 100, but it was found from Corino's pictures that they center around $y^+ \cong 5$ to 15, which is consistent with Kline's findings that the vortices are located just outside the sublayer. Brodkey estimated a diameter of $50\ell+$ and a length of $100\ell+$ for the axial vortex structures. Smith (1978) has observed "connecting" longitudinal vortices as far out as $y^+ \cong 200$. These connecting vortices were observed to extend from one transverse vortical structure forward to a previous transverse vortical structure, seemingly forming a connecting link between them.

Blackwelder and Eckelmann (1977 and 1979) using flush mounted sensors (.75 mm long x .15 mm wide) to measure du/dy and dw/dy, gained insight on how the axial vortices are related to the bursting process. Results of the correlation of the spanwise velocity component measurements normal to the wall suggest the the vortices "pump" low speed fluid toward $z+ = 0$ and away from the wall leading to the formation of new streaks which are broad near the wall and narrower at higher y^+. The strength of these vortices was estimated to the approximately an order of magnitude less than

the mean spanwise vorticity at the wall. They showed that there are counter-rotating streamwise vortices in the wall region that are intermittently disturbed by high speed sweeps (see Figures 10 and 11).

The same researchers (1979) found that the origin of the system of counterrotating streamwise vortices is difficult to determine and thus remains unknown. They also found it difficult to explain what happens to the vortices when a sweep arrives at the wall.

> "The vortex lines are shown to have an abrupt ending at the occurence of the sweep, although it is known that this is not physically realizable."

The distribution, strength, height, and other characteristic parameters of the vortices were assumed to be random variables with fluctuations about their mean values. Available quantitative data of past observers is summarized in Table 1. As can be seen, there is little agreement regarding the physical character of axial vortices, much less the role they play.

Besides experimentalists, analysts are also studying the structure of turbulent boundary layers. The objective of such analysts is twofold. First, they try to explain methematically the physical mechanisms observed by experimentalists. Second, the analyst

tries to use a particular model of the structure to predict the behavior of the turbulent flow. Unfortunately, the analysts' predictions can be judged as correct only if the predictions can be observed in a physical (usually experimental) application. Thus, analysts and experimentalists must work hand-in-hand when studying turbulent boundary layers. However, oftentimes, as is noted by Kovasznay (1971, see Rubesin 1978), experimentalists do not want to know about predictions or predictors do not want to know about turbulence. It seems quite obvious, to the author, that further progress in turbulence studies can be accelerated and possibly eased if experimentalists and analysts "pool" their resources.

Early analysts used truncated forms of the linearized momentum equations to relate the velocity field to the pressure field. However, this approach did not account for Reynolds stress terms. Such notables as Taylor (1936), Sternberg (1965), Shubert and Corcos (1967), and Gurkham and Kader (1970) developed linear models using the linearized momentum equation. However, linear theory fails to describe the flow from the wall and the low frequencies of elementary disturbances (when Reynold's stress terms become important). A

review of linear models and analyses is given in Hatziavramdis (1978).

More recent models have retained the non-linear terms of the Navier-Stokes equations, with numerical solution of the statistical Reynolds-averaged equations presently the basis of most modern analytical methods. The difference between most methods is the varying complexity of the methods they use to establish the Reynolds stresses (Rubesin, 1978). It should be noted that Rubesin points out that these methods do not account for the organized structure observed in the experiments other than in a statistical manner. For a greater detailed explanation of present trends in analytical prediction the reader is referred to Rubesin (1978).

Some attempts have been made to try to relate the dynamical processes in a fully developed turbulent flow to those studied in hydrodynamic stability theory. Bark (1975) extended Landahl's wave guide model to describe the flow close the wall. According to Landahl's theory, bursting is associated with the main flow through a non-linear feedback mechanism. Bark's theory hypothesizes that the statistically dominant velocity fluctuations in the wall region consist of wave packets containing a significant amount of streamwise vorticity.

It was discovered (Landahl, 1975) that other types of disturbances must be incorporated in order to properly model the fluctuation field. Bark based much of his model on the experimental data of Kim et al (1971).

Landahl (1975 and 1977) adds that other types of disturbances besides waves of the Tollmein Schlichting type must be present in order to properly model the fluctuating field. Landahl (1973) assumed that the main non-linear interaction occurred through small and large scale eddy motion mixing. A large scale eddy produced by the mixing will contain a convected part which will move downstream with the local mean velocity. This eddy is sheared and this leads to the formation of a new shear layer further downstream. Finally, the new shear layer causes a new inflectionally unstable region downstream of the original burst and thus makes burst regeneration possible.

Fortuna (1970, see Hatziavramdis 1978) presents a theory that is dominated by pairs of eddies close the the wall. According to this theory, fluid with a large component of axial momentum would be moved toward the wall by the eddies. The fluid exchanges momentum with the wall and is carried from the wall region deficient in axial momentum. He concludes that a pseudo-steady state assumption could be made by assuming that the

eddies close to the wall were of low frequency. As a result of this assumption, the transient term was neglected in the axial momentum equation. Hatziavramdis points out that the energy containing eddies cannot be truly represented by a pseudo-steady state assumption and that the transient term must be included in the axial momentum equation.

Coles (1978) hypothesizes longitudinal vortices in the sublayer to be of a Taylor-Görtler type. He describes three mechanisms at work in the sublayer:

1. At the wall, the mechanism is purely visious.
2. Below $y^+ = 15$, sublayer vortices account for all of the momentum transport by fluctuations, but not for all of the fluctuating energy. These vortices provide a smooth transition between the viscous transport at the wall and the eddy transport in the outer region.
3. Between $y^+ = 15$ and $y^+ = 50$, the mechanism shifts from transport by sublayer vortices to transport by large eddies in the outer flow. These outer eddies are assumed to drive the Taylor-Görtler instability. Coles speculates that the sublayer streaks are longitudinal counter-rotating vortices resulting from an instability of the Taylor-Görtler

type although he has yet to prove this quantitatively. This model finds its weakness at large Reynolds numbers, since he believes that the Taylor-Görtler instability must occur only intermittently in order to energize the sublayer vortices. At the large Reynolds numbers, the instability may become too numerous and thus the model is not applicable.

A very different theory based on the behavior of a two-dimensional vortex convected in a shear flow is proposed by Doligalski and Walker (1979). Figure 12 shows their proposed three phase vortex regeneration mechanism. In the first phase, a "parent" vortex is introduced into the outer region of the boundary layer. Downstream of the vortex, the boundary layer is found to respond to the initial vortex motion. This response, termed upwelling, continues and actually penetrates into the inviscid region. The cross flow in the inviscid region leads to an overturning of the upwelling and an inviscid-viscous interaction takes place representing the second phase (Figure 12c). A new vortex, labeled S, results. The third phase consists of the new vortex and its interaction with the flow. This vortex regeneration and eruption model is being examined experimentally by Smith using flow-visualization. Preliminary results

reveal phenomena which appear very similar to the phenomena presented in Walker's theory (Doligalski, Smith, and Walker, 1980).

Most of the researchers cited shared a common belief that the bursting phenomenon is the predominant mode of turbulence production, yet no definitive cause of this phenomenon has been determined. In many cases, it is speculated that a vortical structure with streamwise alignment plays an important part in the bursting process. The connection between these streamwise vortices and the bursting process, as well as other flow phenomenon, is uncertain.

> "What needs to be established is the presence of vortex-like structures (streamwise vortices, hairpin vortices, etc.) in the wall region and how they relate to other coherent events (ejections, sweeps, etc.)" (Praturi and Brodkey, 1978).

Thus, the objectives of the present research were established as follows:

1. To establish the presence or absence of vortical structures in the wall region, in particular, axial vortical motions.
2. To determine the physical characteristics of the vortical structures.
3. To determine the frequency of occurrence of revolving vortical structures versus

upwellings and downward motions which may contain vorticity, but are not true vortices.

4. To determine how axial vortices "fit" into the bursting process. Are these vortices a cause or an effect of other phenomena?

The investigation will be carried out through use of a recirculating, free-surface water channel. The hydrogen bubble technique combined with flow visualization will be utilized to gain both quantitative and qualitative information and is basically the same technique employed by Runstadler (1963), Kim, et al (1971), and Offen and Kline (1974). Both stationary and moving reference sequences will be employed. A high speed video recording/playback system will be used to record all events under investigation. A special fiber optic lens which mounts to a conventional video camera will be employed to provide underwater end views of the hydrogen bubbles. A complete explanation of the experimental technique is provided in section 4 and describes all the above-mentioned equipment and its use in a much more thorough manner.

A brief summary of the problems researchers have encountered using various experimental techniques

is presented in section 2. In section 3, a description of the coordinate system and hydrogen bubble-wire orientations used in the present study is given. A glossary of terms used throughout the remainder of the text is also presented in section 3. Section 4 describes the experimental apparatus and procedures. For ease of understanding and to eliminate redundancy, results and discussion have been combined and are presented in section 5. Finally, a summary and conclusions are presented in section 6.

TABLE 1

QUANTITATIVE EXPERIMENTAL DATA CONCERNING AXIAL VORTICITY

OBSERVER	METHOD	CONDITIONS	ADDITIONAL INFORMATION	FINDINGS
Kastrinakis, Wallace & Willmarth (1975) See Willmarth (1977)	Vorticity probe measurements in wall region	N/A		Peak RMS ω_x at $y^+ \cong 20$
Falco (1977, 1979)	Smoke visualization probe measurements	$Re_\theta \cong 1000\text{-}4000$		Diameter of axial vortex - $20D^+$ Length of axial vortex - $100x^+$ Spacing between counterrotating pairs -$80z^+$
Smith (1978)	H_2 bubble visualization	$Re_\theta \cong 1200$ $U_t \cong .8$ cm/s		Longitudinal vortex penetrated up from wall to $y^+ \cong 300$ Spacing between pairs $50z^+$ at $t^+ = 0$ then reduced to $25z^+$ at $t^+ = 50$
Praturi & Brodkey (1978)	Stereoscopic visualization of tracer particles dye injection	$Re_\theta \cong 900$	Field of view $950x^+$ x $1000z^+$ x $850y^+$ moving reference frame	Diameter of vortex - $50z^+$ Length of vortex - $100x^+$ Center of vortex - $y^+ = 5\text{-}15$ but extends to $y^+ \cong 10\text{-}25$
Lee, Eckelmann, & Hanratty (1974)	Electro-chemical probes - flush mounted	$Re_D = 34700 - 40900$	Measured S_x and S_z patterns (longitudinal and transverse components of turbulent fluctuating velocity gradient at the wall) $\lambda^+ = 9.4$ between adjacent stations leading to poor spatial resolution of $\partial s_z/\partial z$,	Wave length $\lambda^+ = 106$ at R=34700 $\lambda^+ = 105$ at Re=37200 $\lambda^+ = 107$ at Re=40900 $\Delta z^+ = 50$ between vortices
Blackwelder & Eckelmann (1979) Blackwelder (1978)	Hot film 90° V probe wall sensors.	$U_\infty = 21$ cm/s Re width $\cong$ 7700	Oil used to magnify viscous region correlated spanwise fluctuations to obtain vortex locations and spacings. Streamwise fluctuation correlations to find length. Used quadrant analysis.	Vortices are quasi-periodic in spanwise direction Center of vortices $y^+ = 20\text{-}30$ Length - $\Delta x^+ > 1000$ Strength is an order of magnitude less than spanwise vorticity at the wall. 1 revolution every $1000x^+$

TABLE 1

QUANTITATIVE EXPERIMENTAL DATA CONCERNING AXIAL VORTICITY

Kreplin & Eckelmann (1979)	Same as Blackwelder & Eckelmann (1979)	Same as Blackwelder & Eckelmann (1979)	Vortex center average $y^+ = 30$ Counterrotating pairs with separation of centers $\Delta z^+ = 50$ Length of inclination to wall decreases as vortices move downstream.
Falco & Kline (1979) Summary of M.S.U. conference			ω_x vorticity (not considered a revolving vortical structure) exists in a zone of $0<y^+<7\text{-}10$ Stronger streamwise vortical motions in a zone $7\text{-}10<y^+<30\text{-}50$ Moin & Kim - using large Eddy simulation found long zones of ω_x do not exist and that ω_x maximum is at $y^+ = 0$

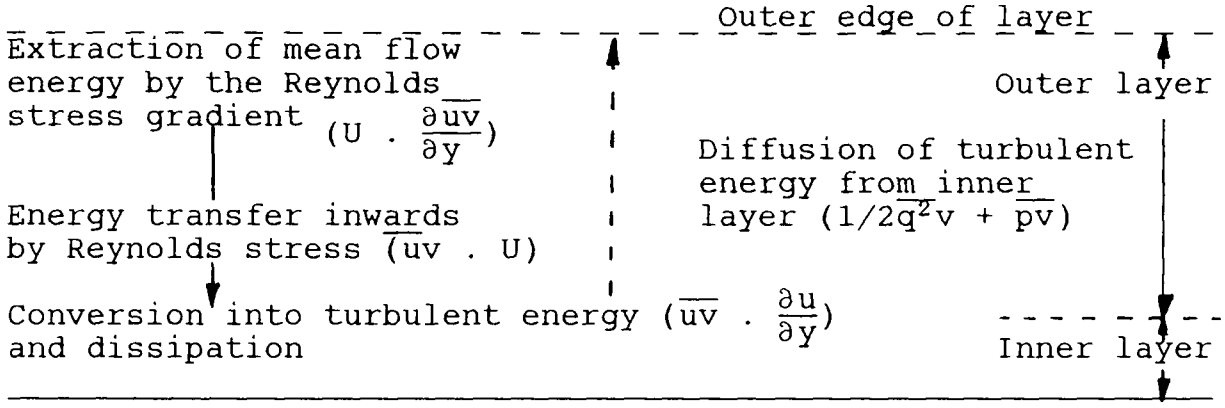

FIGURE 1 - Townsend's Two Layer Model and Energy Flow in a Boundary Layer (1956)

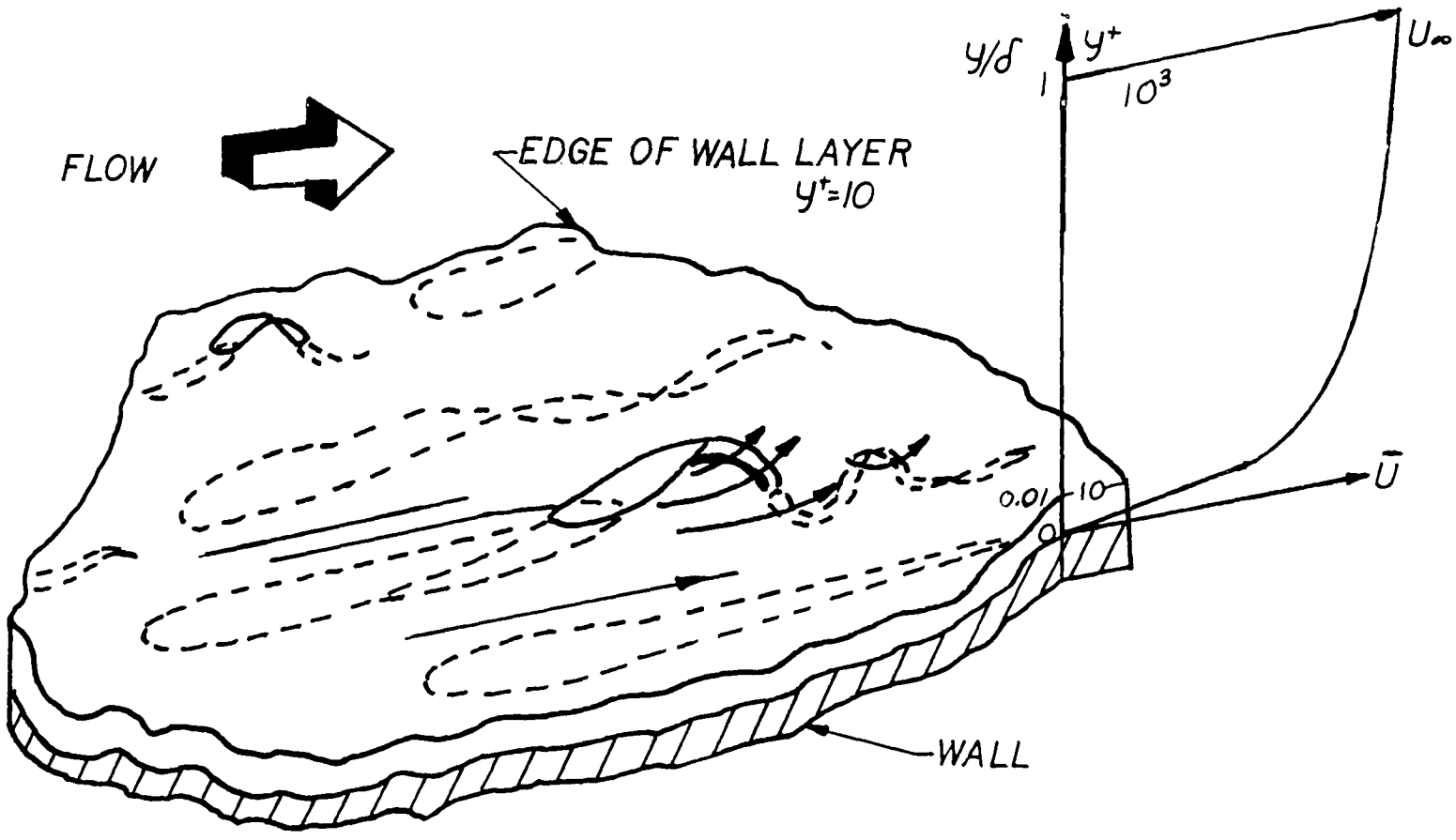

FIGURE 2 - Sketch of Wall Layer Flow. Figure illustrates the projection of a low speed streak through a plane bounding the wall layers and located at $y^+ = 10$. The loops of the streak external to the wall layers represent the configuration of an element of the wall layer structure at the start of the ejection process. The scale of the layers near the wall has been exaggerated. (Runstadler, 1963)

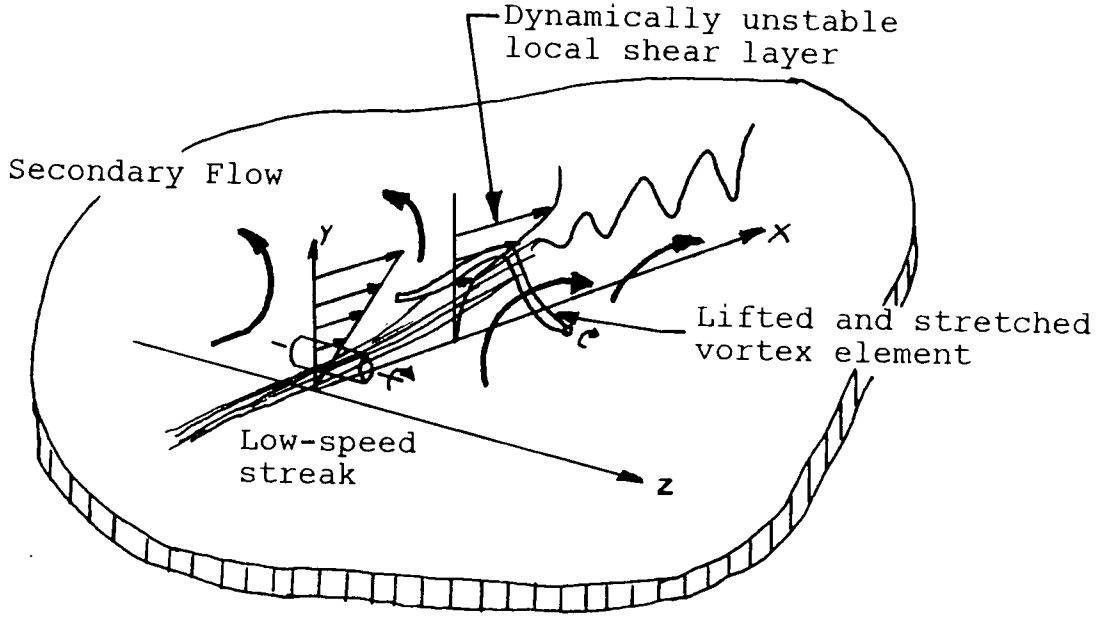

FIGURE 3 - Mechanics of Streak Break-up (Kline, 1967)

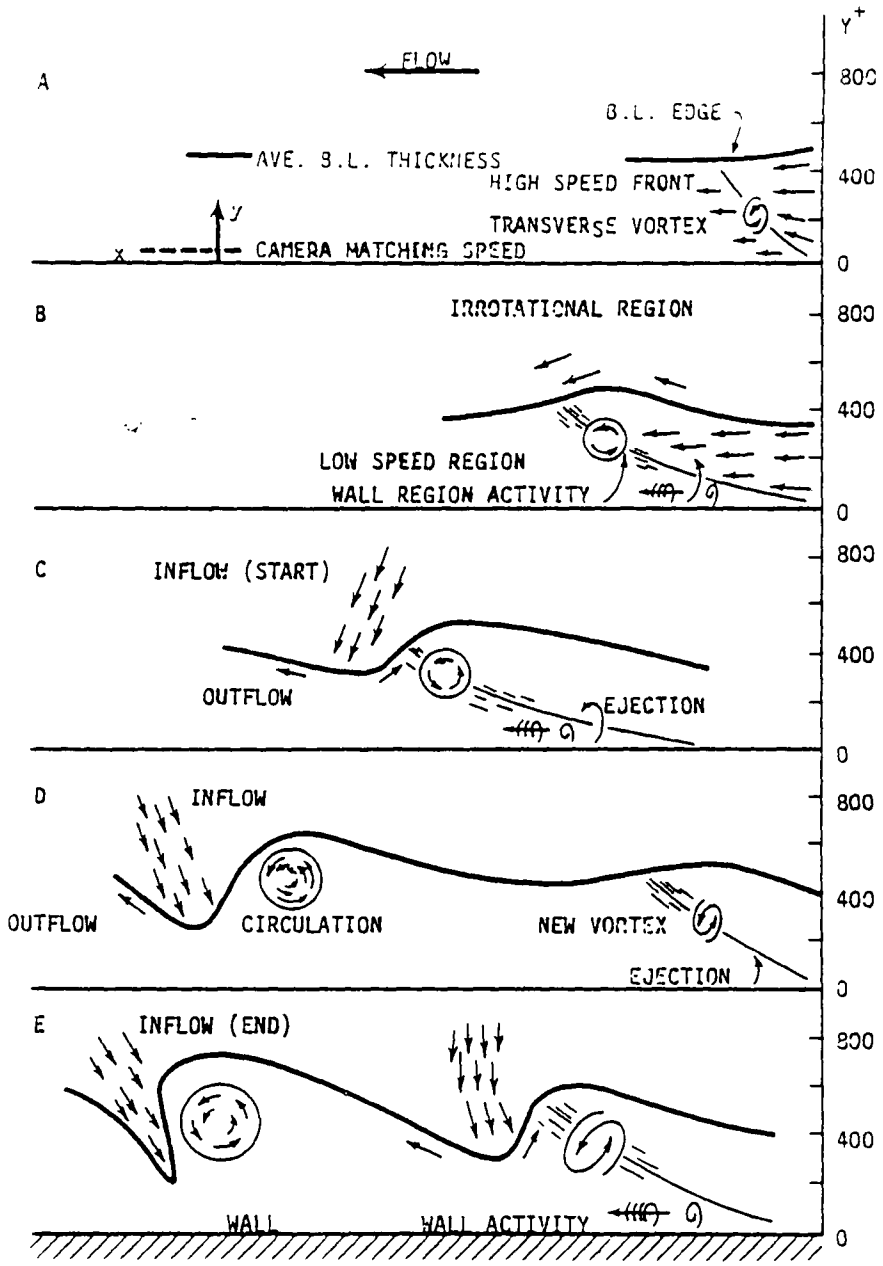

FIGURE 4 -Sketch of the progression of the flow. (Brodkey, 1978)

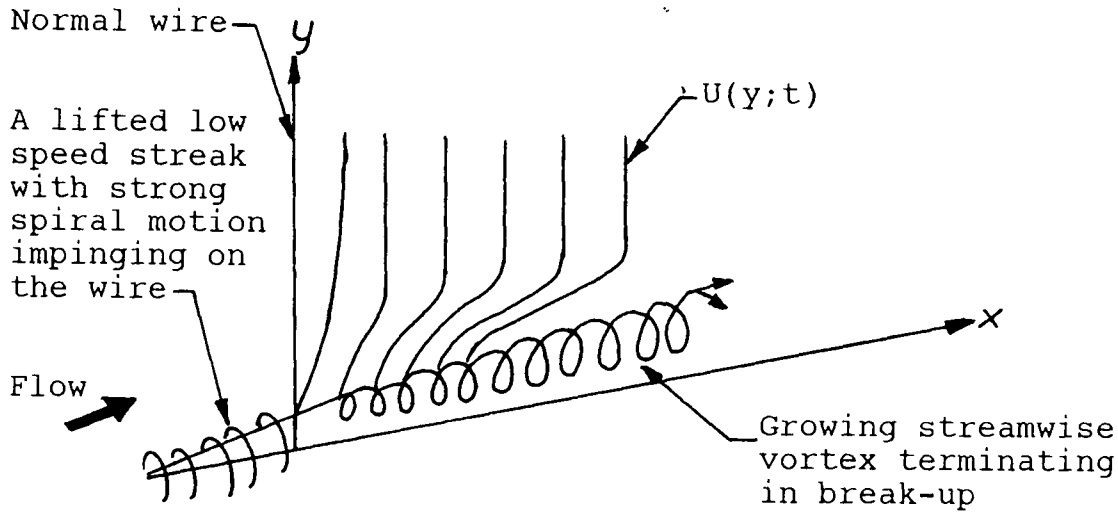

FIGURE 5 - Schematic Illustration of the Formation of Streamwise Vortex Motion During Bursting (Kim, 1971)

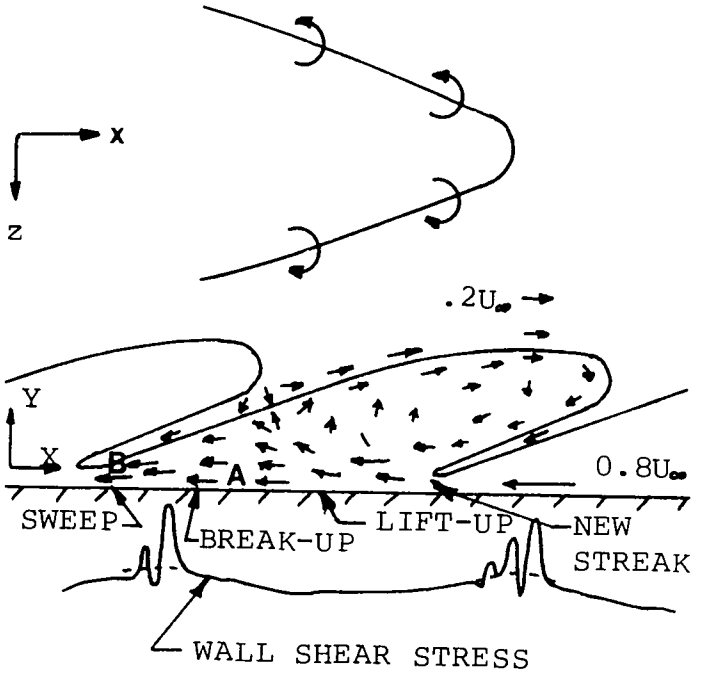

FIGURE 6 - Proposed flow pattern that might be seen by an observer moving at a speed of 0.8 U_∞ and the associated wall shear stress distribution (Brown and Thomas, 1977)

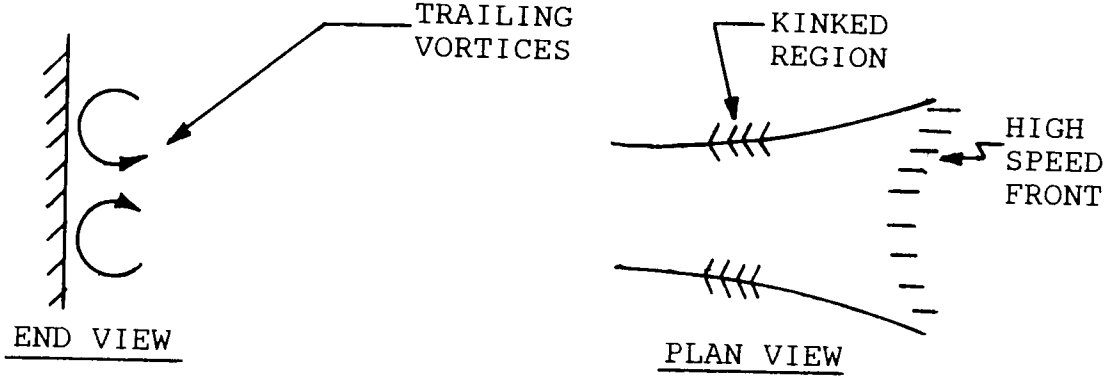

FIGURE 7 - High Speed Front Formation (Smith, 1978)

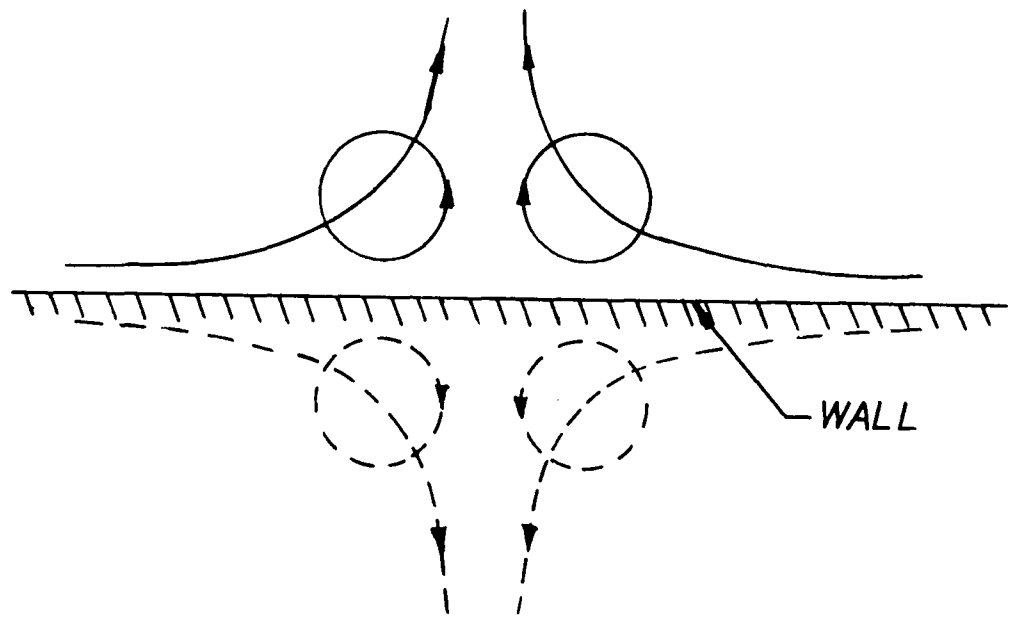

FIGURE 8 - Sketch of Vortex Pair Near the Wall. Image of pair below the wall. Dashed lines are vortex centers (Willmarth, 1975)

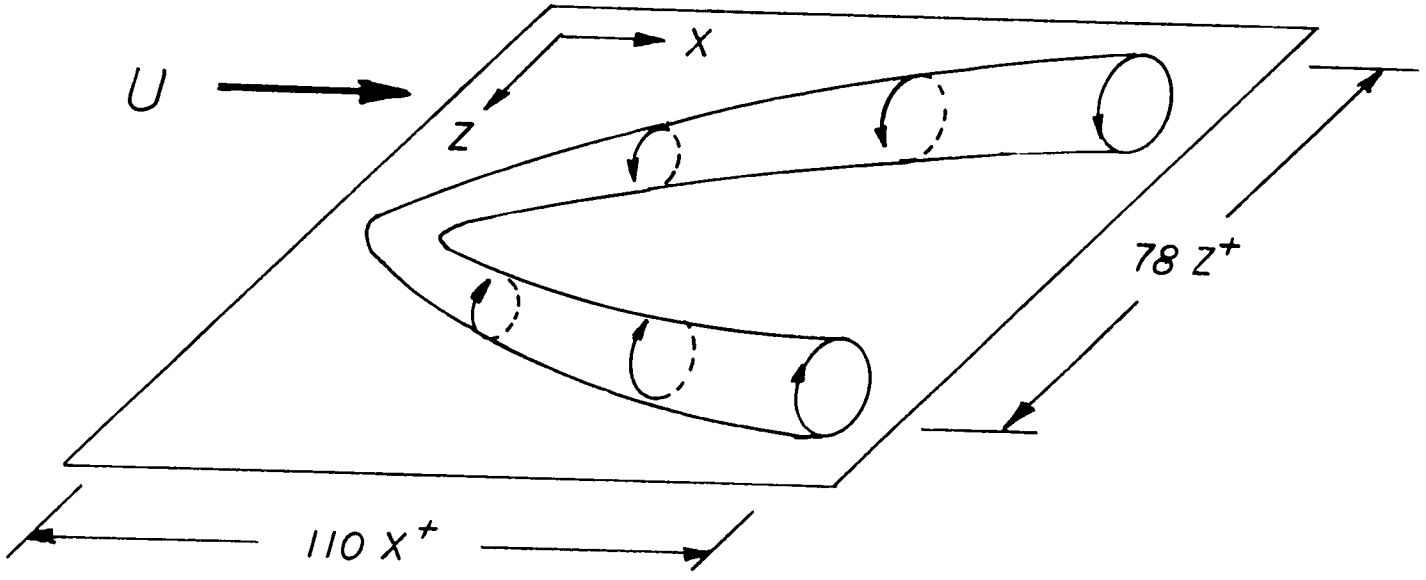

FIGURE 9 - An isometric sketch of a pocket, showing the often visible streamwise portions of the vortex which lies along the boundary. These streamwise vortices are connected at the upstream end of the pocket, where the radius of curvature of the vortex tube is very high. The segments have a circulation which brings fluid towards the wall between them (Falco, 1979)

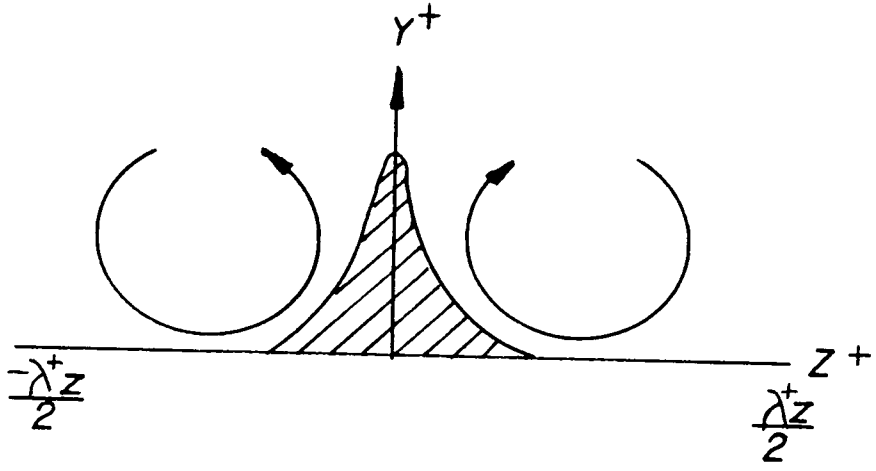

FIGURE 10 - Cross Sectional View of a Low Speed Streak Lying Between Two Counter-Rotating Streamwise Vortices (Blackwelder, 1978)

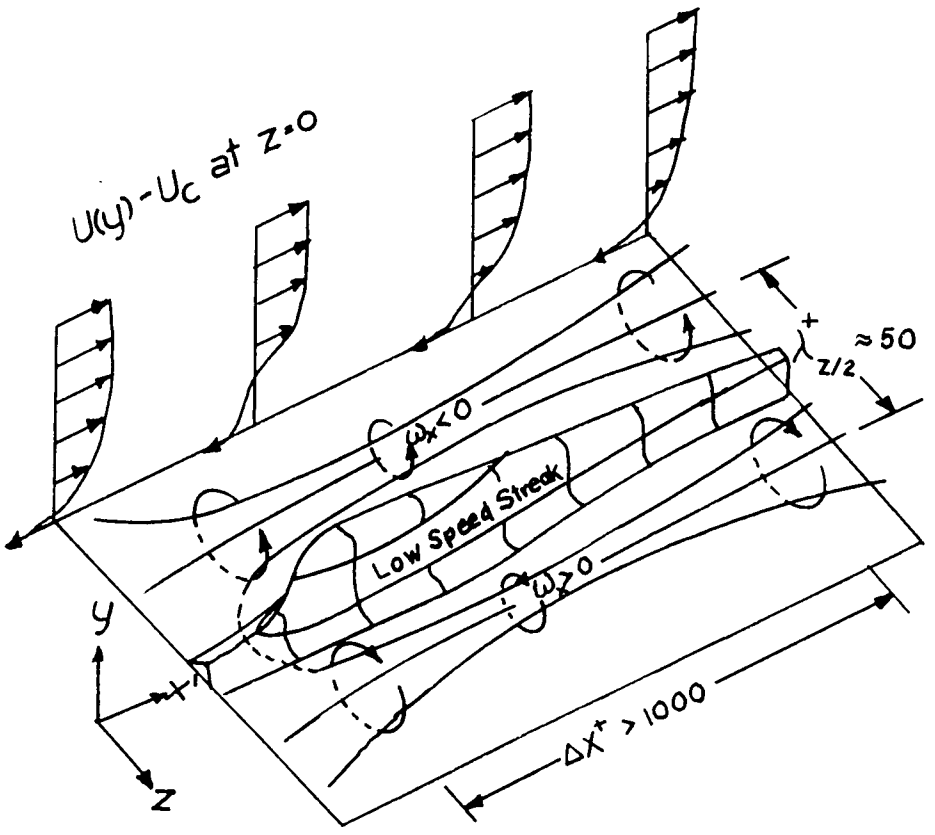

FIGURE 11 - Model of the Counter-rotating Streamwise Vortices with the Resulting Low-speed Streak. (Blackwelder, 1978)

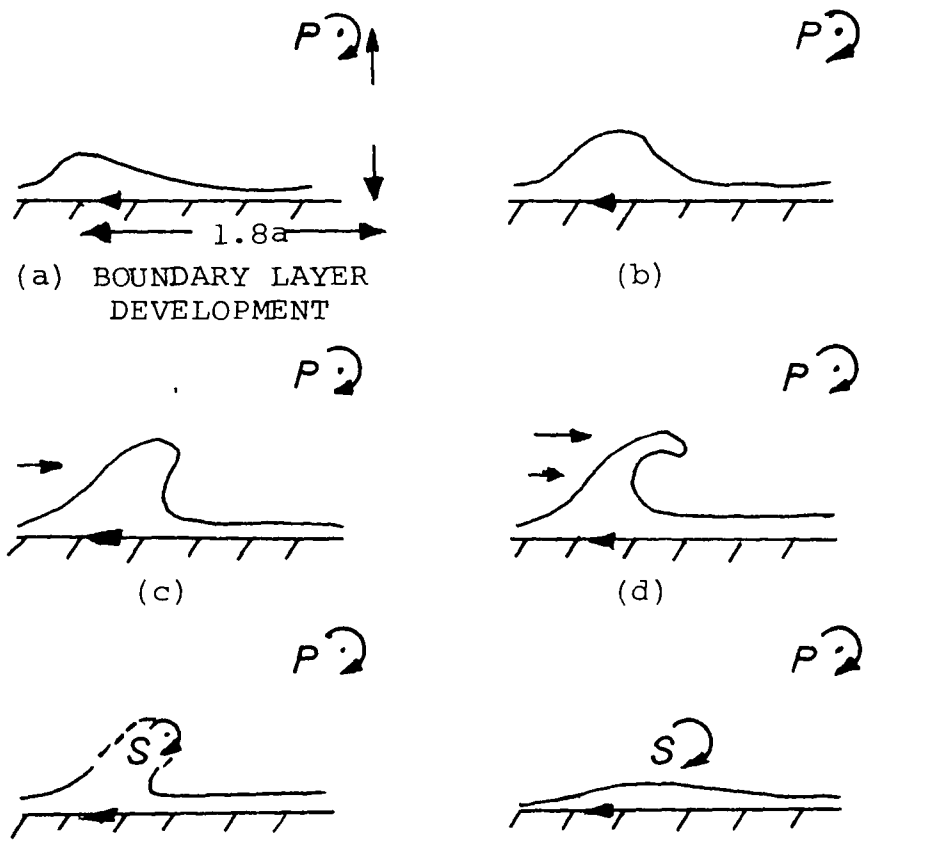

FIGURE 12 - Proposed Three Phase Regeneration Mechanism (Doligaski, 1980)

SECTION 2

BRIEF SUMMARY OF THE DRAWBACKS OF PREVIOUS RESEARCH EFFORTS

2.A General

There is no perfect method for measuring turbulence. All methods at present, which include flow visualization techniques, probe usage, and laser doppler techniques, have their respective advantages and disadvantages. Some of the problems with the visualization and probe methods will be discussed briefly. It should be noted that many observers such as Kline (1978), Kim (1974), and others believe that the use of probes and flow visualization simultaneously offset, to a large extent, each technique's individual weaknesses.

2.B Probe Measurements

Probe measurements have been shown to have large errors near boundaries. Wyngaard (1969, see Willmarth, 1979) analyzed the spatial resolution of a streamwise vorticity probe exposed to isotropic turbulence and showed that measurement errors are large unless probe sizes are on an order of magnitude smaller than the turbulence scales they attempt to measure. The error generally arises from the fact that there is an

acceleration of fluid between the probe and the wall caused by the probe as it nears the wall. This problem is somewhat minimized by the use of boundary layer probes.

Schraub (1965) believes probes cannot provide velocity information over a large area without interfering with the flow field. Similar conclusions were drawn when Eckelmann (1978) stated that the presence of the probe in his experiments resulted in severe alterations of the flow structure characteristics in the viscous sublayer. Based on the experiments of Blackwelder and Eckelmann (1979), Kreplin, Eckelmann, and Wallace (1974), and Eckelmann (1970, 1974), Eckelmann concluded that a two-wire V-probe causes a change in existing flow structure by its mere physical presence. The streamwise velocity and wall gradient components seemed to be unaffected by the change. However, a 180° phase shift was noted in the spanwise velocity and wall gradient components. This could be misinterpreted as a new vortex structure in the sublayer but is actually a structure generated by the probe. It is worth noting that the above observers used oil to magnify the viscous region yet still encountered problems in close proximity to the wall.

In an effort to detect small scale motions near the wall, Willmarth and Bogar (1977, see Willmarth, 1978) developed an "X" hot wire array with wire length and spacings on the order of 2.5 viscous lengths. They found that the probe was so small that it was difficult to align and orient the hot-wire arrangement. To compensate for this lack of precision, a special calibration scheme was developed. Willmarth and Bogar determined that the X-probe could be used if the flow over the probe was uniform, and they determined that for $y^+ > 400$ their data was in agreement with classical methods. However, for $y^+ < 400$, it was believed that non-uniform flow resulted in invalid results. These results indicate that even if probes are made quite small, thus alleviating some of the interference problem, other problems can arise.

The need for averaging to extract turbulent structure poses an interesting problem in use of probes. Usually data is taken with large noise backgrounds which facilitates the need for averaging. The fact that the observer cannot actually "see" a structure or phenomenon makes it extremely difficult to obtain relative measurements and compounds the averaging problem. As Kline (1978) points out, there is the danger that an important phenomenon will be missed. He

sites examples of how probe measurements of the outer portion of the viscous sublayer (taken prior to the 1950s) failed to pick up the alternating high and low speed streak structures. The probe size was speculated to be the culprit (the sensing portions were larger than the structure itself). Due to the large sizes, the probes averaged over a large region, simply averaging the structures right out of the picture. Another example is the pairing process in free shear flows, which was not revealed in the works of Browand and Mollo-Christensen because of averaging, but was clearly revealed in later, detailed visual studies (Winant and Browand, 1974).

Single hot wire probes register the magnitude of the vector normal to the wire, meaning that large V components are often read as changes in U. As a result, larger vorticity probes consisting of up to ten wires have been developed to more accurately detect proper velocity components. Unfortunately, these are again generally too large to detect small-scale vorticity. In addition, the point-by-point data obtained through probe measurements makes a large region difficult and costly to analyze.

One final difficulty encountered when using a probe technique is that of tracking a structure.

Although it is possible to obtain phase relations for some points, it is not possible to follow the Lagrangion motion of particles.

2.C Flow Visualization

Visualization techniques also have several limitations. In the past, most observers used motion picture film. Thus, it was almost impossible for the experimentalist to observe what was actually being recorded on film. Many runs were often required to obtain a minimal amount of usable footage. Today, closed circuit television using video tape playback has alleviated the above-mentioned problem since the tapes can be instantly viewed and corrections to an experiment can be made immediately.

However, visual techniques only show spatial and temporal relationships between motions of particles or structures. They cannot show actual causality. Offen and Kline (1973) demonstrated that their visualization could not show that the outer disturbance actually caused a lift-up near the wall. Three-dimensional effects are also difficult to perceive. Praturi and Brodkey (1978) pointed out that a side view makes it very deceiving when trying to sense the direction of rotation of longitudinal vortices. Offen and Kline (1973) also found detection of upward tilted streamwise

vortices a challenge when observations were done only from a side view.

Another drawback of the visualization technique is that there is a relatively high uncertainty in numerical values obtained. This is partially due to resolution problems. The use of synchronous strobes (synchronized with camera shutter speed) partially eliminates resolution problems by providing very short exposure times. The strobe produces very short, light pulses (on the order of 10 microseconds) and thus gives the effect of having a very short exposure time (Helmig and Sluijter, 1972).

One of the most criticized points of the visualization method is that streaklines rather than pathlines or streamlines are observed. One must relate the streaklines to actual physical processes via mental processes. Much of this difficulty is alleviated by using combined-time-streak markers such as Shraub (1964) and others have employed. Extraction of quantitative data is extremely time-consuming and tedious. Smith (1978) found this problem is simply compounded when using more than one view.

A less obvious problem mentioned by Smith (1978) is that vorticity cannot be visualized directly. Only the effects of vorticity can be observed. If a

vortex is weak, it may appear only as a small disturbance or flow irregularity when convected in a strong mean flow and observed in a laboratory reference frame. It is felt that a moving reference frame (cameras move with the flow) can accentuate the effects of convected vorticity.

SECTION 3

COORDINATE SYSTEMS AND GLOSSARY OF TERMS

3.A Coordinate System (see Figure 13):

Streamwise - in direction of flow; also termed axial and longitudinal; denoted x-direction.

Normal - perpendicular to surface of the water channel; denoted y-direction.

Transverse - across the plate, perpendicular to the flow; denoted z-direction.

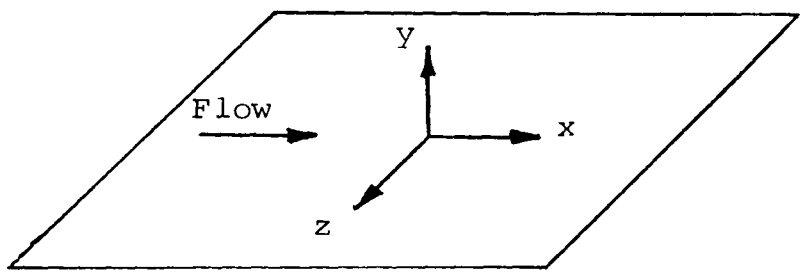

FIGURE 13 - COORDINATE SYSTEM

3.B Wire Directions:

Normal - a wire stretched in y-direction.

Transverse - a wire stretched in z-direction.

3.C View Directions (see Figure 14):

Plan-View - line of sight is in y-direction.

Side-View - line of sight is in z-direction.

End-View - line of sight is in x-direction.

3.D Glossary of Terms

A glossary of terms is provided to familiarize the reader with terms used throughout the remainder of the text. Most terms were defined at the Coherent Structures of Turbulent Boundary Layers Workshop in 1978 held at Lehigh University. Other, new terms will be added as is necessary in the text.

1. Streak: A high speed or low speed (relative to the mean) region in the linear sublayer, greatly extended in the streamwise direction.
2. Linear Sublayer: y^+ less than 7-10. Region is not sharply defined but in which the mean viscous stress is nearly constant.
3. Lift-up: Outward movement of fluid in the low speed streak to a point outside the linear sublayer.
4. Streak Oscillation: Apparent amplifying three-dimensional oscillation in side and plan view of a lifted low speed streak.
5. Wall Scales: $\ell = \nu/u_\tau$, $u_\tau = \sqrt{\tau_w/\rho}$
6. Breakdown: An abrupt event in which the streak oscillations terminate in the formation of a large region containing a wide range of small scales.
7. Bursting: Process which carries the fluid from a relatively quiescent wall region to a more chaotic, turbulent outer region.

8. Quiescent Period: Period between bursting processes.

9. Sweep: Large-scale inward motion of faster moving fluid, observed as a local acceleration in flow field.

10. Log Region: y^+ greater than 30-40 but less than wake matching point.

11. Bulge: A large-scale, three-dimensional structure, which dominates the visual appearance of the outer layer, with scales of the order of the boundary layer thickness.

12. Coherent Structure: A confined region in space and time in which definite phase relationships exist among flow variables.

3.E Scales

The Workshop of Coherent Structures of Turbulent Boundary Layers held in 1978 at Lehigh University defined the following scales applicable to boundary layer studies (where L is the actual size of the coherent motion):

1. Large-scale: Order of boundary layer thickness; also called integral scale.

2. Medium-scale: $50 < LU_\tau/\nu < 300$; also called Taylor microscale.

3. Small-scale: $1 < LU_\tau / \nu < 10$; also called Kolmogorov scale.

3.F Vortex Motions (refer to Figure 15):

Most vortical motions have vortex lines with components in all three coordinate directions. A streamwise vortex shall be vortical motion which is aligned principally in the flow direction. The path of an individual particle appears as a helix since it is being carried with the flow as rotation occurs. A transverse vortex has its axis of rotation along the z-axis. Positive rotational motion is termed when the vortical structure revolves counterclockwise as viewed from downstream (i.e., in the negative x-direction) in the case of the streamwise vortices and viewed in the negative z-direction in the case of the transverse vortices.

At the Stanford Meeting in 1978 (see Falco 1978), some observers felt that streamwise vortices should be thought of as upwellings and downward motions not revolving vortical structures because the streaks only possess streamwise vorticity after lift-up. There was also speculation by some that there is a zone above the linear sublayer where revolving vortical structures do exist ($7\text{-}10 < y^+ < 30\text{-}50$).

To distinguish between revolving vortical structures and upwellings and downward motions in the video pictures,

the mathematical definition of vorticity in the stream-wise direction is needed and can be written as:

$$\omega_x = \frac{\partial w}{\partial y} - \frac{\partial v}{\partial z} \qquad (1)$$

As is well known, this equation is a measure of angular velocity. Therefore, only motions containing both of the velocity gradient components in equation 1 will be considered revolving vortical structures. This situation is shown in Figure 16a. If only one component, say $\partial v/\partial z$, is present, this will be appropriately defined as an upwelling or downward motion. This is represented in Figure 16b.

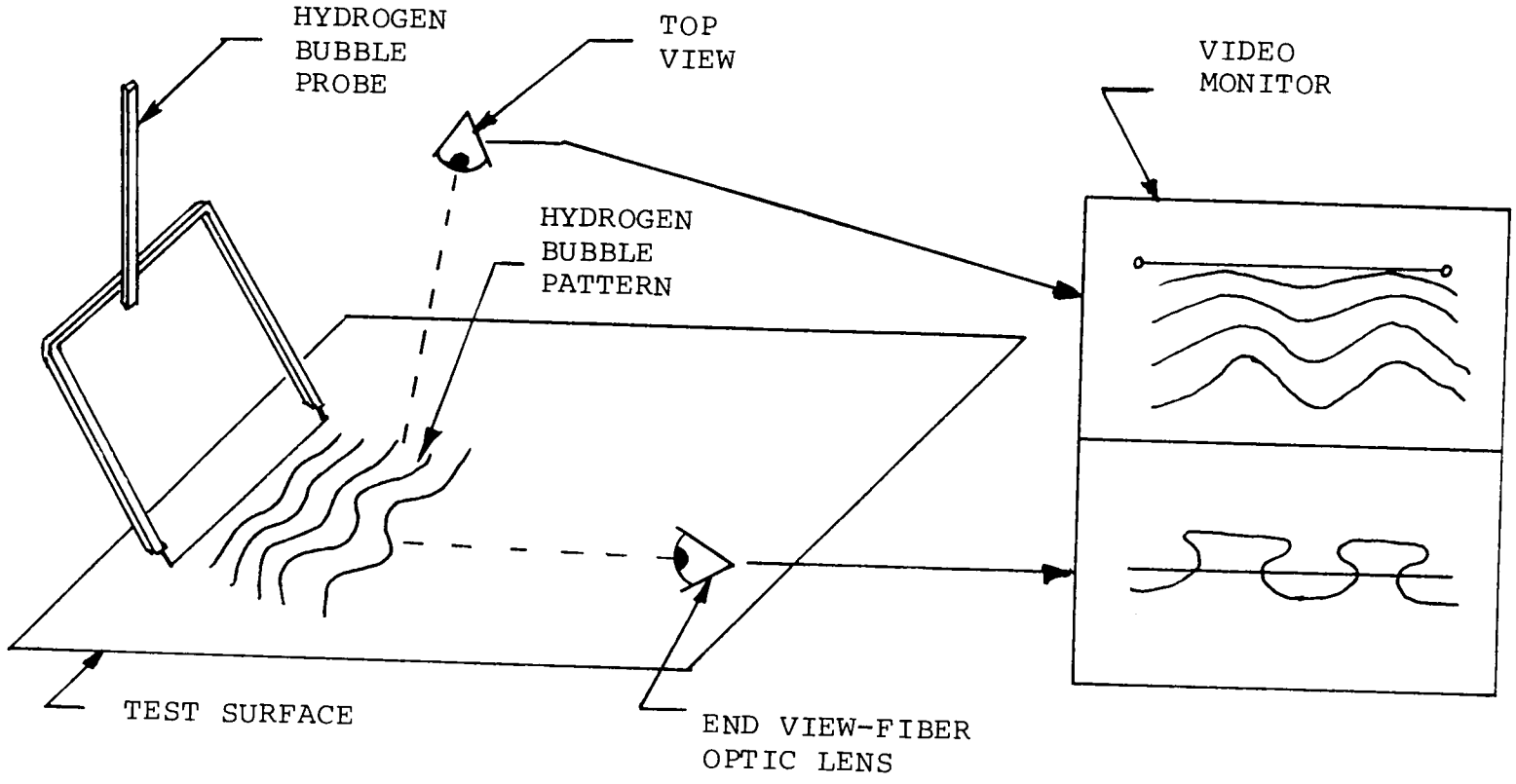

Figure 14 - Viewing Directions

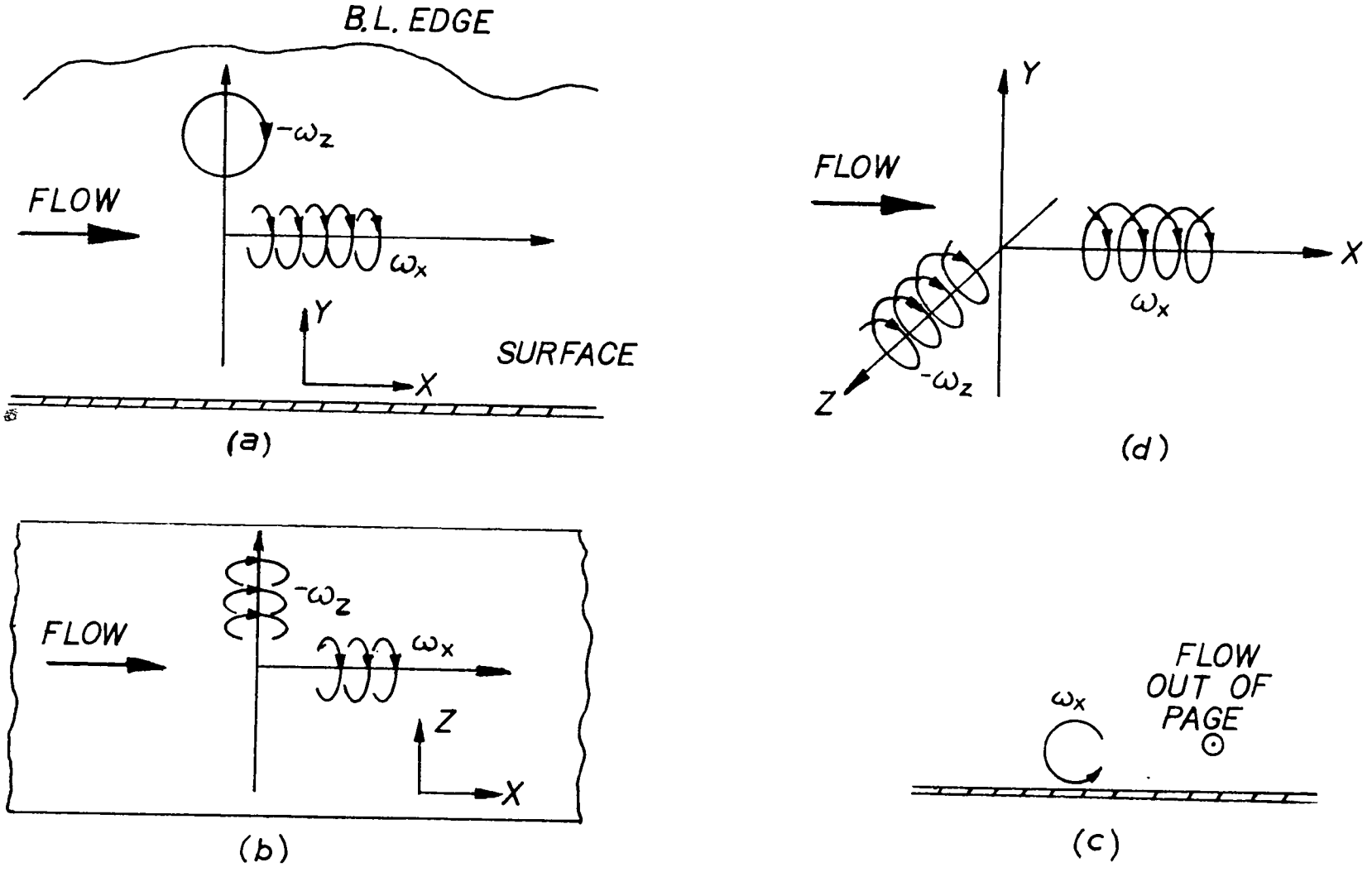

FIGURE 15 - Coordinate System for Vortex Motions. (a) Side View (b) Top View (c) End View (d) Three Dimensional View (Adapted from Praturi and Brodkey, 1978)

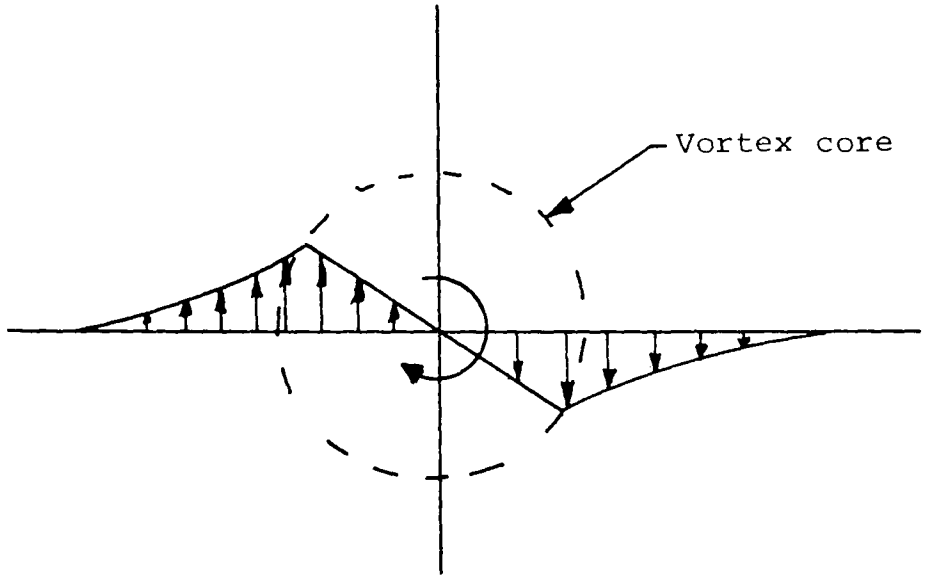

Figure 16a - Rotating Structure Velocity Profile

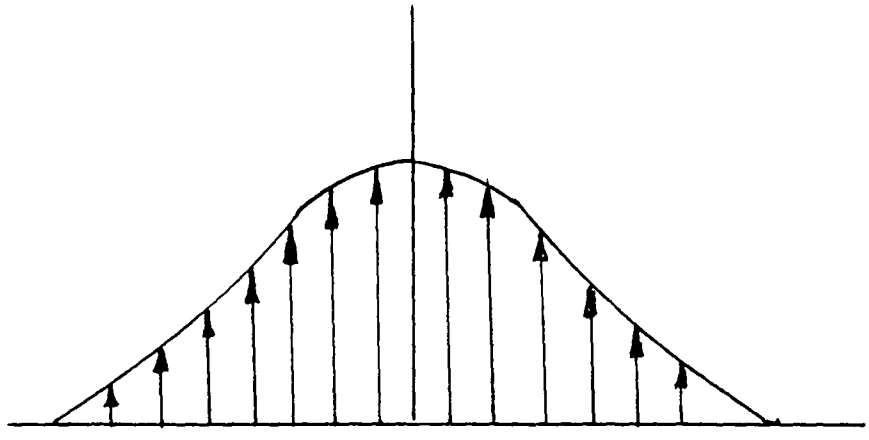

Figure 16b - Upwelling Velocity Profile

SECTION 4

EXPERIMENTAL APPARATUS

4.A General

A recirculating, free-surface water channel is used to carry out the desired experimental objectives. The flow is essentially zero pressure gradient with free stream velocities attainable to 0.63 m/s. The system is located in the Fluids Research Laboratory, Department of Mechanical Engineering, Lehigh University. This section describes the total facility in terms of the major constituent systems, consisting of the: (1) water channel, (2) moving reference platform, (3) flow visualization system, and (4) video system.

4.B Water Channel

Figures 17 and 18 are respectively a schematic and photograph of the water channel system. The channel has a 5.0 m x 0.86 m x 0.3 m working section made of 1.9 cm thick plexiglas. The inlet flow enters a large inlet tank from .15 m diameter pipe through a distribution manifold, which distributes the flow evenly in the spanwise direction. The flow then passes through a 10 cm thick settling sponge which further distributes

the flow and lowers free-stream turbulence intensity. Following the settling sponge, the flow is straightened by a honeycomb/screen system consisting of 7.6 cm thick fiberglass honeycomb having 0.48 cm cell size, followed immediately by a #20 mesh stainless steel screen (Loehrke and Nagib, 1976). The flow then passes through a 1.75:1 inlet contraction (Morel, 1976) and enters the test section. A 3 mm trip rod is located at the exit of the inlet contraction and insures transition to turbulence. The flow rate in the channel is variable, can be varied from 1 cm/sec to 63 cm/sec, and is controlled using a Peerless Pump, Type 6AD8-1/2, driven by a Westinghouse 7-1/2 hp d-c variable speed motor. Using this system, it is possible to achieve Reynolds numbers of up to 3.4×10^6 based on length and 5.26×10^3 based on momentum thickness. By use of an auxiliary heating system, the water temperature can be raised to 35°C thus raising the achievable Reynolds numbers to 4.37×10^6 and 6.98×10^3, again based respectively on location and momentum thickness.

In order to minimize vibration effects from the pump, 15 cm sections of pipe leading to and from the pump were replaced by flexible rubber couplings which served as dampers. No direct measurements of vibration characteristics were taken, but no noticeable

vibration due to pump characteristics were evidenced in the test section.

4.C Moving Reference Platform

The advantages of using a moving reference platform have been noted previously by several experimentalists (such as Kim, 1971; Smith, 1978; Praturi and Brodkey, 1978). Smith (1978) discussed the fact the convected vorticity in a flow may be weak and thus appear only as a small disturbance when observed in a fixed, laboratory (Eulerian) reference frame. Smith felt that the use of a moving (Lagrangian) reference frame will accentuate the effects of the convected vorticity since the observer can then "follow" the vortex during its evolution.

Thus, a moving reference platform as shown in Figure 18 is utilized. The platform is a 1.22 m x .71 m rectangular frame constructed of 5 cm square aluminum tubing. A series of stainless steel support shafts provide for equipment attachment. The platform rides on a pair of 3.8 cm diameter hardened steel shafts mounted directly on the water channel frame. The platform is guided on one shaft by two linear motion bearings while the other side is supported on two cam followers. A second cart, to carry lighting equipment beneath the channel, rides on four low friction ball

bearing wheels. The two platforms are driven by a 1 hp power matched/d-c type electric motor coupled to a 20:1 gear reducer. Figure 19 shows the platform drive system. Aircraft cable used to activate the traverse cart runs the length of the channel between the gear reducer and a pulley mounted at the entrance to the test section. A chain drive, similar to that of a bicycle, connects the upper cable drive to an identical lower cable drive. This lower cable drive activates the lower cart, while the chain drive synchronizes the speeds of the lower and upper carts. The speed of the platforms is controlled using a Reliance Flex Pak V*S drive system, with platform speeds of up to 0.50 mps attainable.

4.D Flow Visualization

The hydrogen bubble technique was the primary method used for flow visualization. This method, which allows both quantitative and qualitative data to be obtained, is basically the same as that used by Runstadler (1963), Kim et al (1971), and Offen and Kline (1974).

The hydrogen bubbles were generated using a power pulse generator which can supply controlled square wave power pulses to 90 V and 250 mA, and at frequencies up to 340 Hz. Two types of hydrogen bubble probes were constructed and employed. The first, which

allows combined end and plan views to be taken, consisted of one horizontal platinum wire soldered to the two supports as shown in Figure 20. The reader is referred to Metzler (1980) for complete construction procedure of the single wire probe. In addition to the single wire probe, a probe consisting of three horizontal platinum wires was constructed (see Figure 21). The three horizontal wires allow simultaneous studies to be done over a larger range of y^+ values. The wires are located 5 mm apart, corresponding to a separation distance of $\Delta y^+ = 28$ at $U_\infty = .13$ mps and water temperature of 22°C. Of course, this non-dimensional separation will vary depending on flow velocity and temperature. The probe is constructed of brass tubing of 3 mm and 1 mm diameters. The span between legs is 16 cm which is equivalent to approximately 900 viscous lengths.

Construction of the three-wire probe proved difficult since it involved applying equal tension to all three wires. If one wire was too slack, it was observed to vibrate in the flow. A scheme utilizing one continuous platinum wire of .25 μm thickness was finally found to work satisfactorily. The wire was soldered at point A (see Figure 21) and stretched across to point B. Rather than soldering at this point, the wire was wrapped around the leg and wound

down to point C. From point C, the wire was again stretched across the span to point D where the winding was done again. Thus the wires could be adjusted to equal tension before final soldering was done at point E. As a finishing touch, the bottom wire was carefully moved to the extreme bottom of the support at point F and soldered.

Twenty gauge wire was wrapped around the legs of the probe to minimize vibration caused by vortex shedding. The probe was sprayed with an insulating non-reflective paint and the tips were insulated with GC Electronics Red GLPT insulating varnish in order to eliminate spurious bubble formation, a problem of past research on this and other projects (Kline, 1967, etc.).

Mobility of the bubble wire probes in the y-direction was of utmost importance as was accuracy in locating the wire in the y-direction. A traversing mechanism which allowed the wire to be located within ± 0.1 mm of a desired y^+ location was built. This traversing mechanism consists of a fine tooth worm to which the probe holder is meshed. By turning the adjustment knob, the holder is moved up or down along the screw. Cam followers are mounted on both sides of

two vertical pieces of drill rod in order to steady the holder.

4.E Closed Circuit Television System

For viewing and recording the flow visualization data, a Video Logic INSTAR (Instant Analysis and Replay) video recording and display system was employed, with a framing rate of 120 frames per second. This system allows simultaneous viewing and recording of two separate views utilizing two identical video cameras and a split-screen capability. This feature proves invaluable in detecting rotational behavior. Figures 22 and 23 show the camera set-up for dual view (top and end view) recording (refer to Figure 14).

To allow end view studies, which requires a waterproof means of viewing, a 1 m long fiber optic lens was attached to one of the conventional video cameras (see Figures 22 and 23). Figure 24 shows the fiber optic lens which consists of a large number (bundle) of light transmitting fibers enclosed in a watertight, flexible casing. The lens is 1.10 cm in diameter and houses a focusing lens which is manually controlled.

The fiber optic lens allowed under-water pictures to be taken from downstream. The range of focus of the fiber optic lens was found to be somewhat

limited causing a problem with depth of field. Therefore, measurements taken while utilizing the fiber optic lens were done while the bubbles were as close as possible to the hydrogen bubble probe. Once the bubbles were carried downstream towards the lens, they quickly passed out of the depth of field; however, it was possible to accurately observe the bubbles for up to 400 viscous lengths. No interference of the flow due to the lens' presence was observed in the viewing region. The distance between the hydrogen bubble probe and the viewing end of the lens was normally $575 < \Delta X^+ < 715$ (where ΔX^+ changes as the flow velocity changes). The lens was usually mounted at a 4 to 5° angle to the test surface. Thus, the hydrogen bubbles appear to move slightly downward as they move toward the lens.

The television cameras are equipped with 6:1 zoom lenses. With the addition of a Canon 2X extender and/or one of several close-up lens, total fields of view as small as 1 cm x 1 cm can be observed from distances of 0.5 m. Thus, with this system it is possible to study very small flow structures and areas of interaction.

The output from the cameras can be viewed on a 250 line direct overlay monitor and recorded on 1" magnetic tapes. Playback can be viewed at normal (real

time) speed or in forward or reverse slow motion. Slow motion speeds can be adjusted continuously from 15% of real time to a single frame mode (stop action). Any frame can be frozen and analyzed for as long as required.

Illumination is provided via two synchronized (to framing rate) strobe lights of 90 W output with illumination time of 10 μ seconds, yielding an effective frame exposure time of 10^{-4} s. The use of strobe lights in effectively "freezing" each frame was discussed in Section 2 on Drawbacks of Previous Experiments.

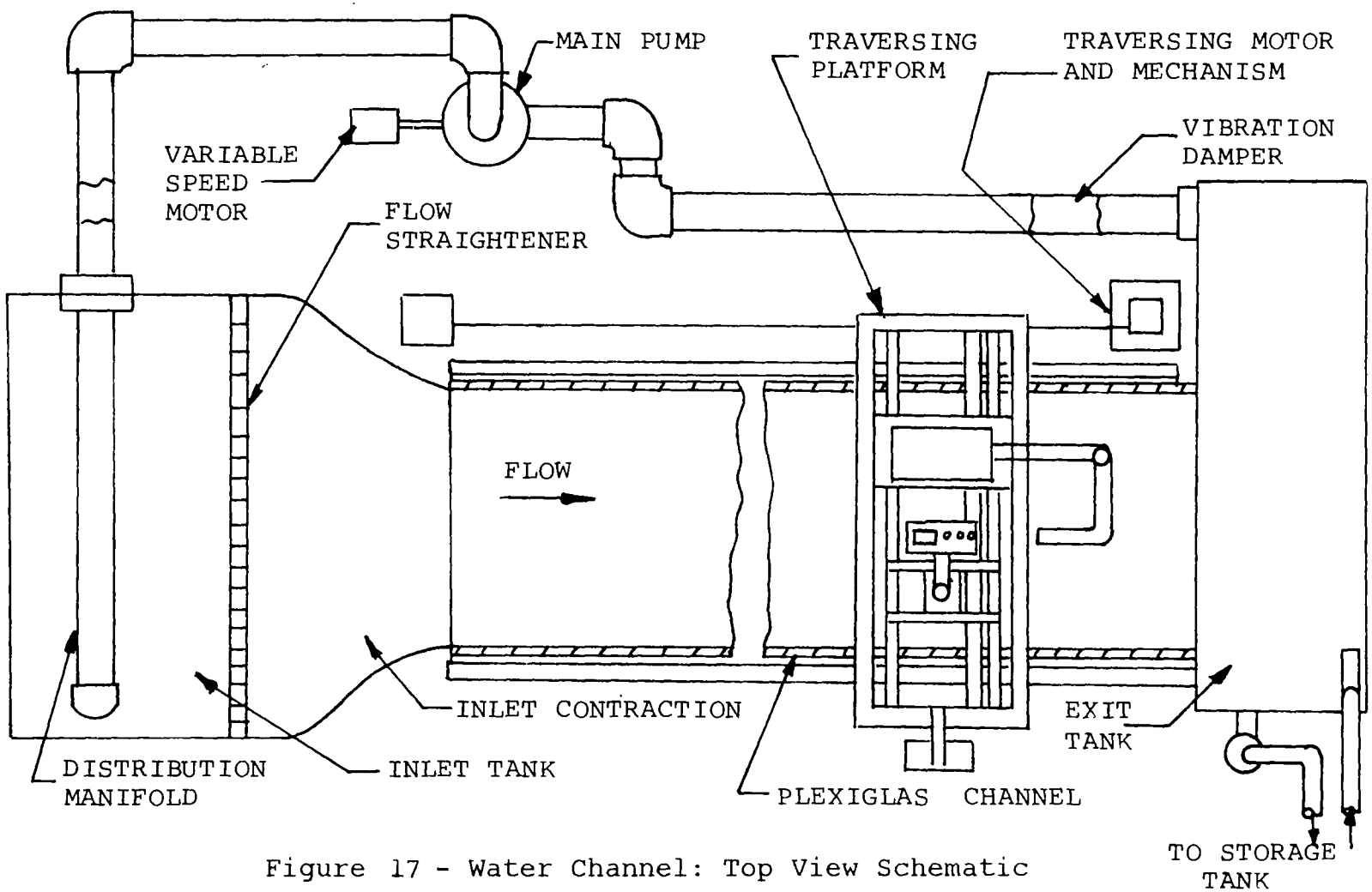

Figure 17 - Water Channel: Top View Schematic

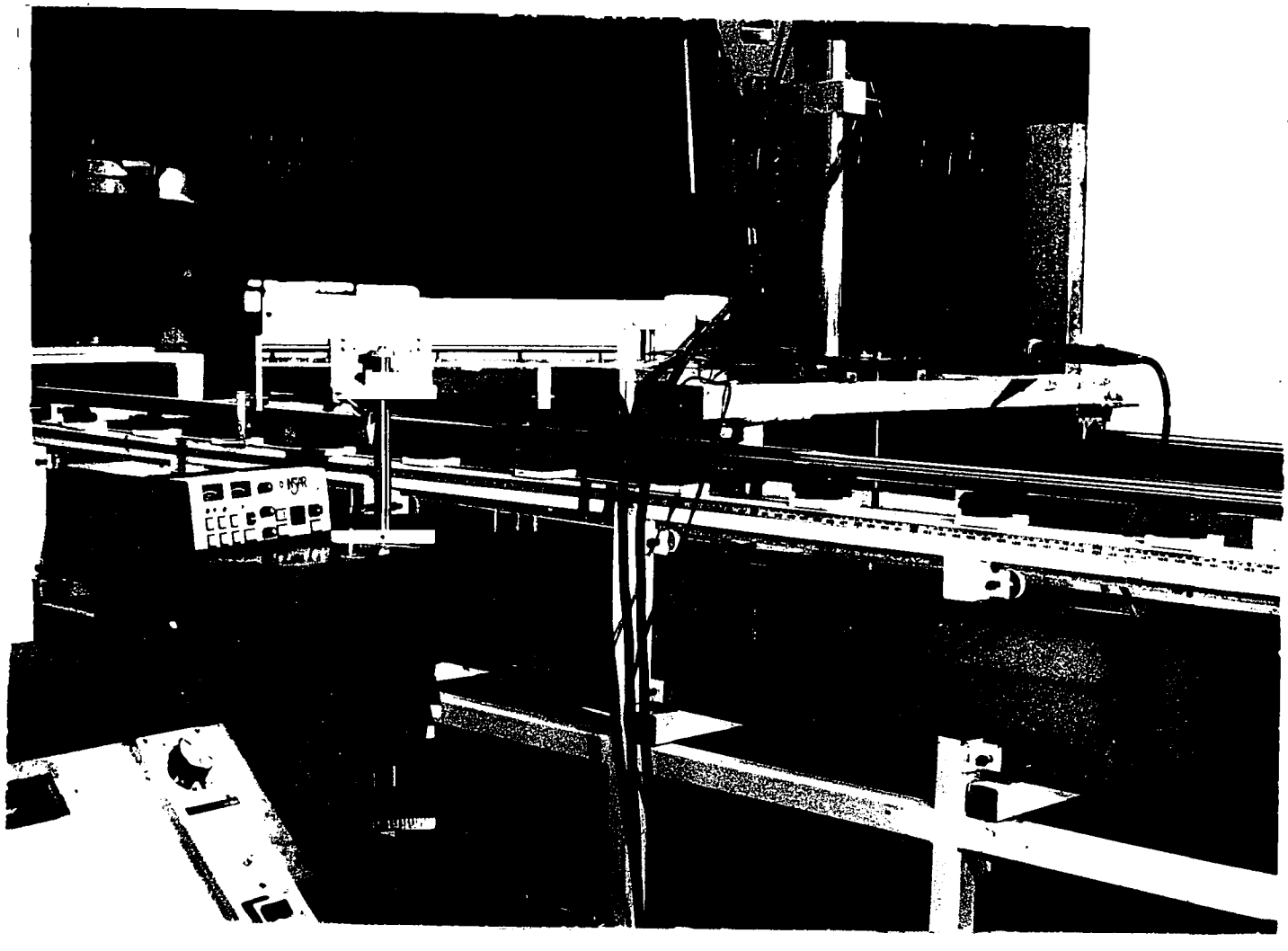

Figure 18 - Water Channel: Set-up for Dual View (top-end) Studies.

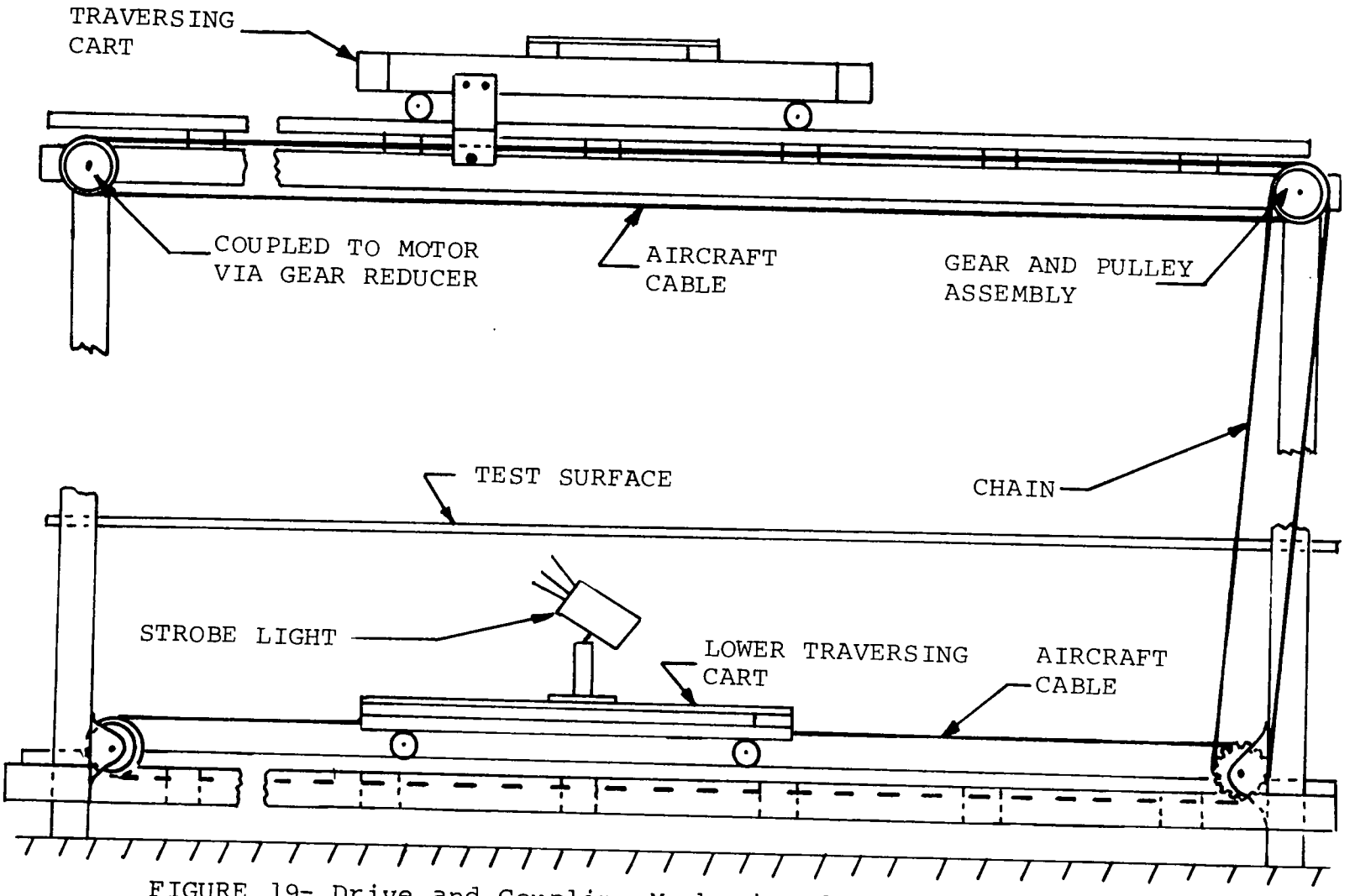

FIGURE 19- Drive and Coupling Mechanism for Traversing Carts

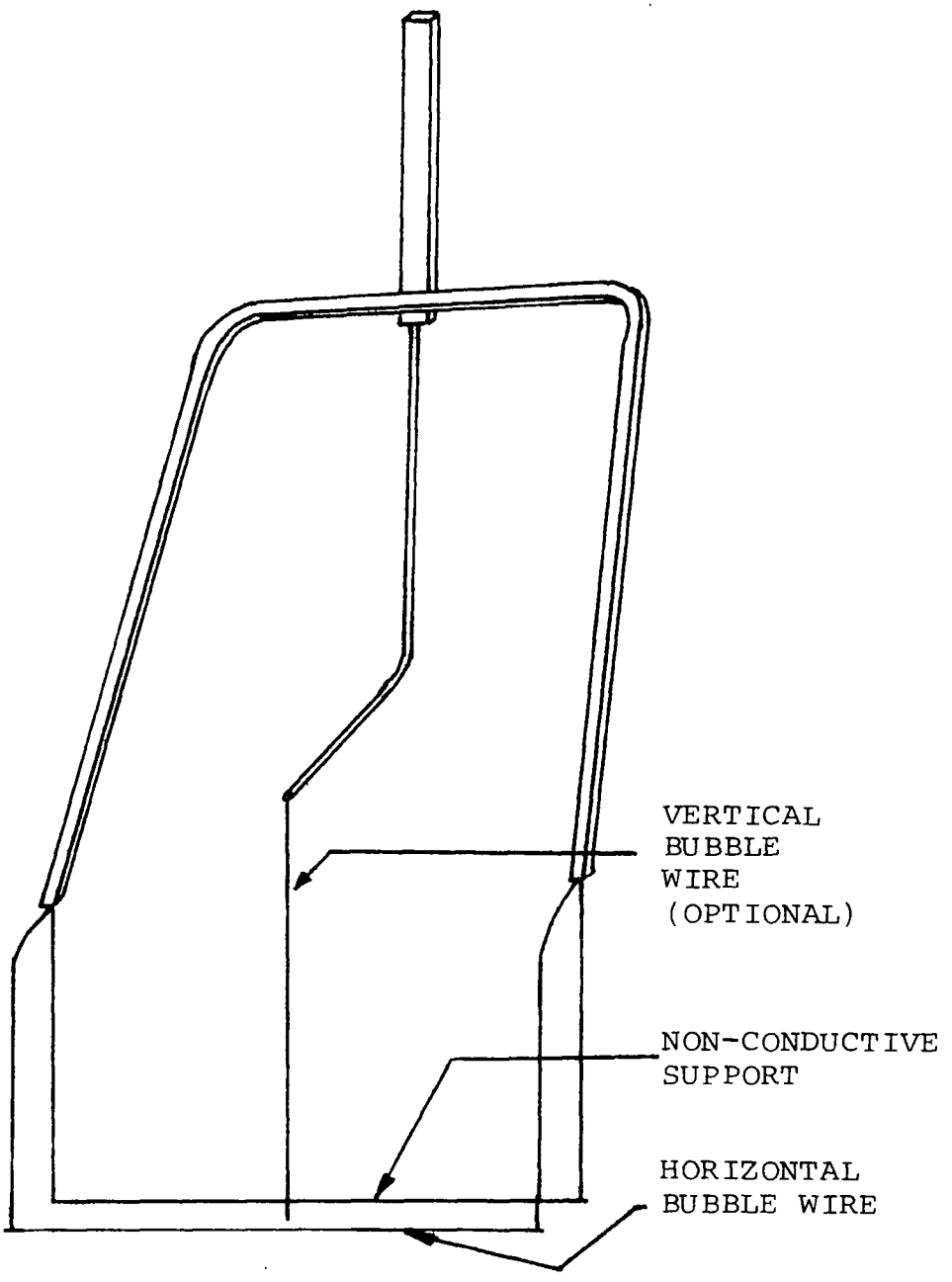

FIGURE 20- Hydrogen Bubble Probe

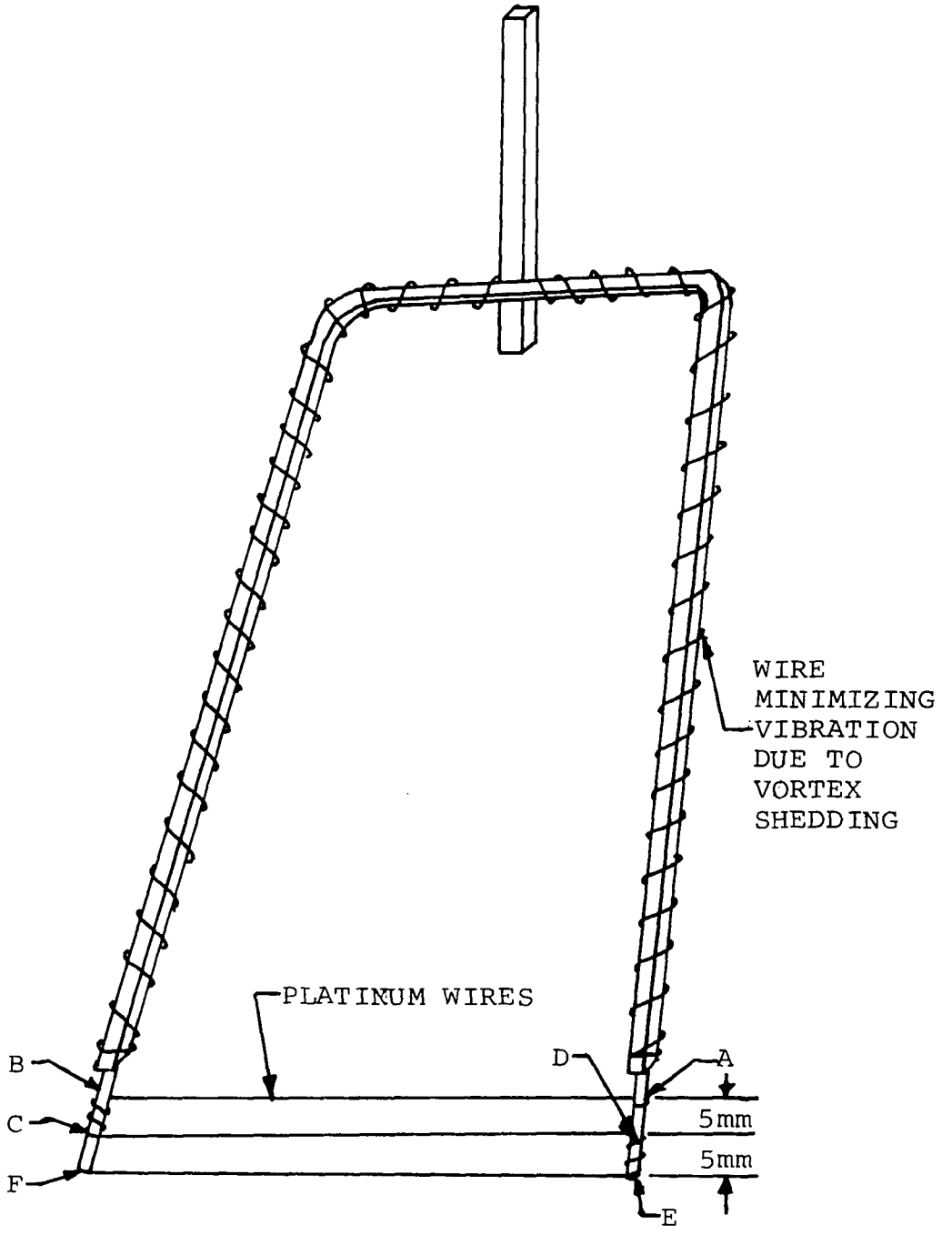

FIGURE 21- Three Wire Hydrogen Bubble Probe

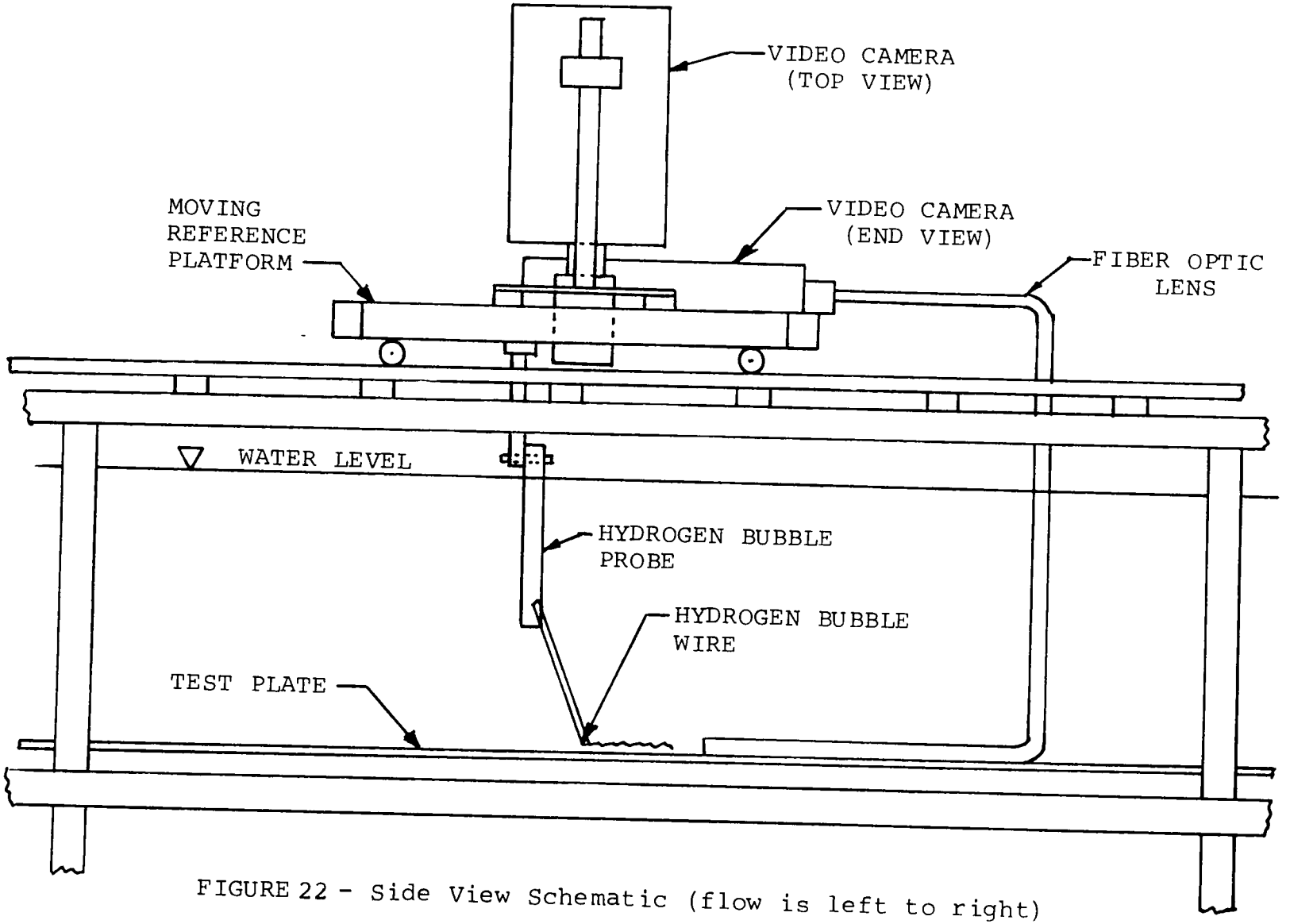

FIGURE 22 - Side View Schematic (flow is left to right)

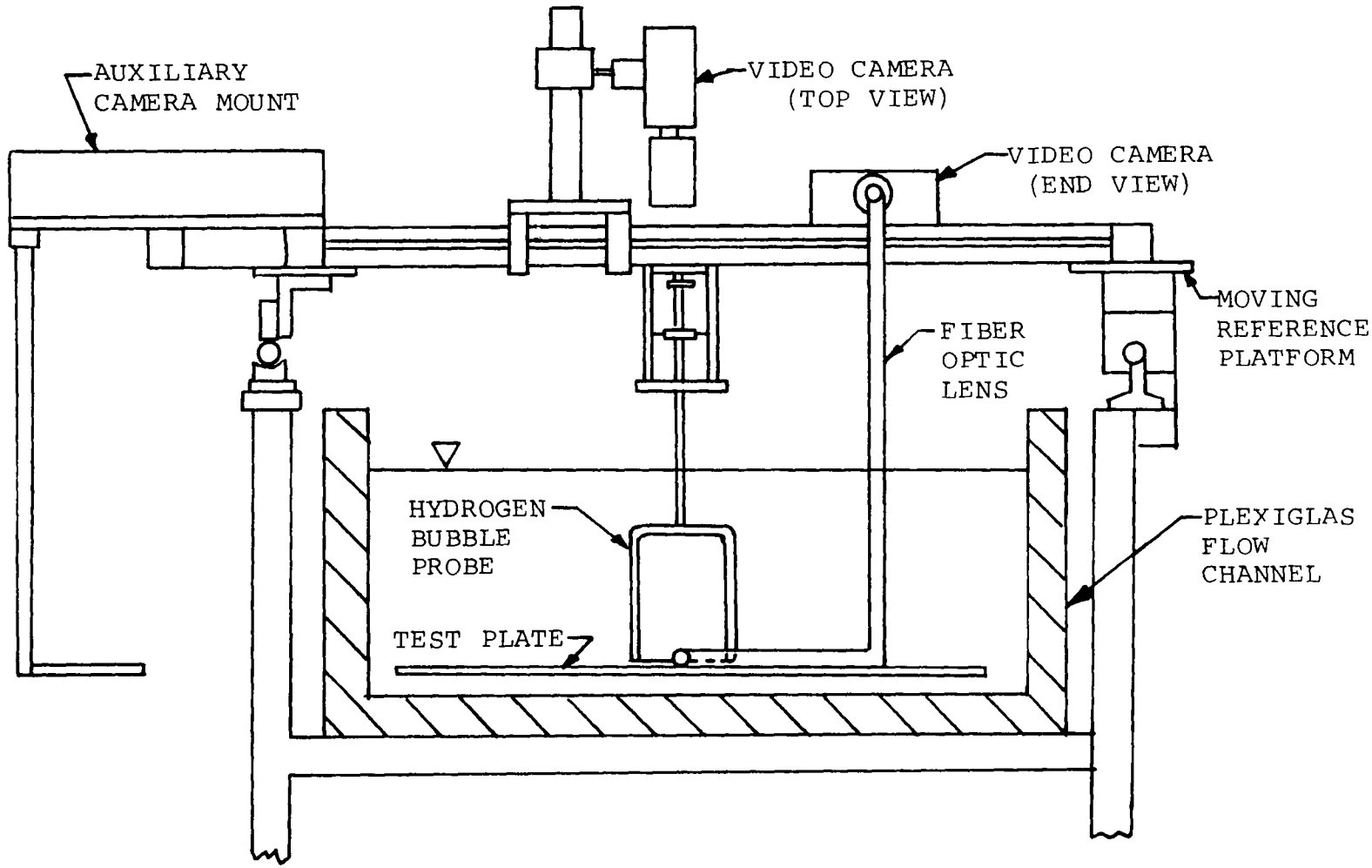

FIGURE 23- End View Schematic (flow is out of page)

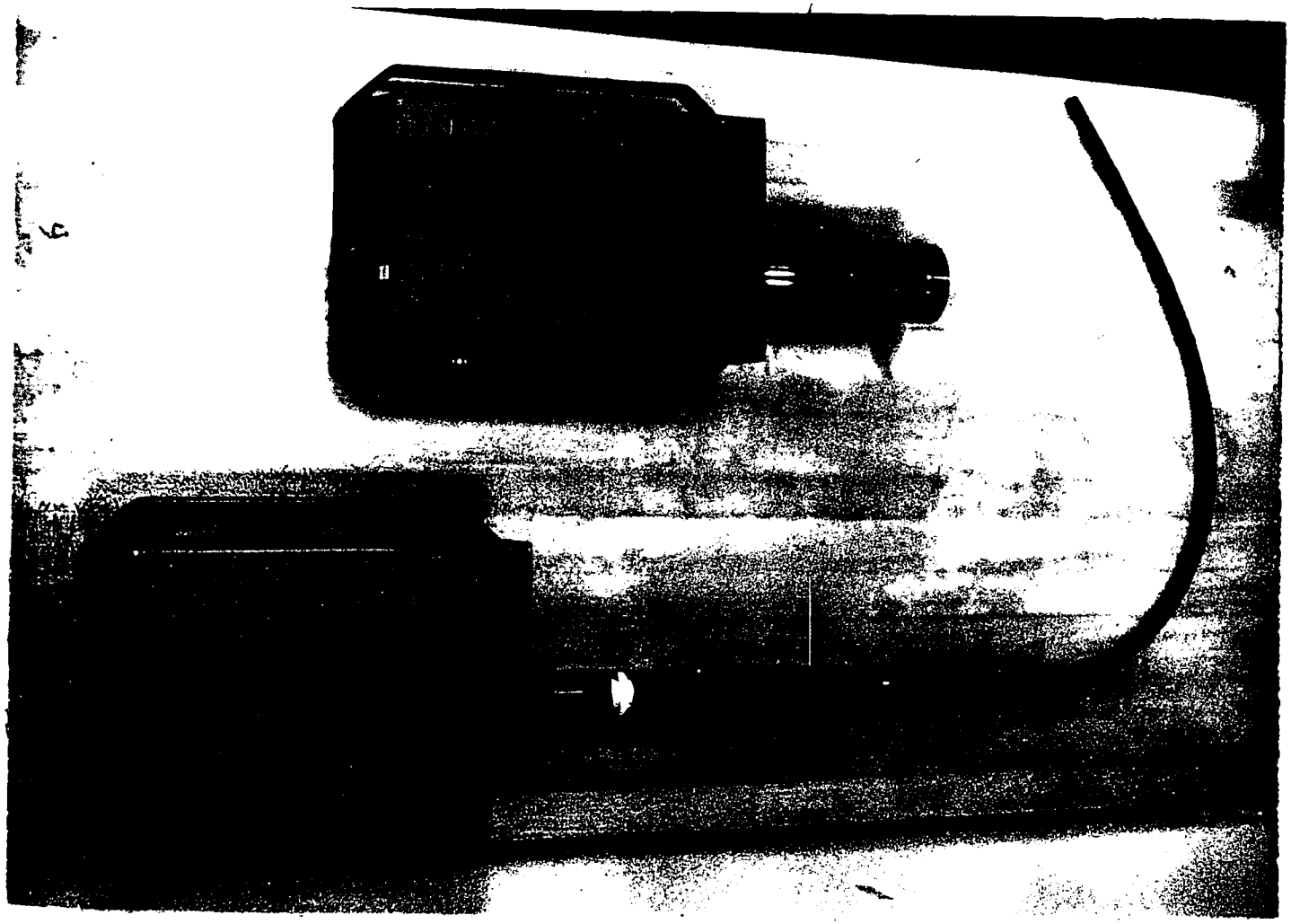

Figure 24 - Comparison of Fiber Optic and Conventional Camera Lenses. Both lenses are mounted on identical cameras.

SECTION 5

RESULTS AND DISCUSSION

5.A Introduction

Several experiments were conducted utilizing both vertically and horizontally oriented hydrogen bubble wires. Most of the visual studies in this investigation employed the end view (refer to Section 3 for view description), which was sometimes combined with a plan view (i.e., split screen). Preliminary side view and plan view combinations were also examined. Both fixed reference frame and moving reference frame sequences were recorded for free stream flow velocities ranging from 0.12 m/s to 0.30 m/s, with the location of the tests varying from 2.1 m to 3.96 m downstream of the inlet to the test section. Reynolds numbers based on momentum thickness ranged from 635 (at x = 2.1 m and U_∞ = .12 mps) to 2200 (at x = 3.96 m and U_∞ = .30 m/s).

Approximately four hours of recorded information were analyzed and the results, both qualitative and quantitative, are summarized in this section. Presentation of the results is basically an integration of the qualitative and quantitative findings. The qualitative results serve to describe the physics of

the flow phenomena in the inner region of the boundary layer while the quantitative results provide the actual physical dimensions of the flow structures (both spatial and temporal) such as rotational speed of vortices, diameters, locations, etc. Discussion of physical characteristics is done in terms of non-dimensional parameters such as x^+, y^+, z^+, and t^+ (representing streamwise, normal, spanwise, and time dimensions, respectively) as well as other parameters found in the list of symbols.

Finally the observed flow events and their relationship to existing flow models will be discussed when appropriate. These comparisons will be done throughout the results presentation rather than in a separate section in order to avoid redundancy.

Note that a description of distances relative to the boundary layer thickness is generally avoided since the flows examined were of $Re_\theta \leq 2200$, which is below the value of Re_θ considered necessary for fully developed conditions (Smith, 1978). These conditions are, however, felt to be more than adequate for study of turbulent structure in the wall region, since the velocity profiles in the downstream half of the channel were shown to be in appropirate agreement with accepted law of the wall correlations (see Metzler, 1980). Note

that the range of Re_θ examined is essentially the same or greater than the ranges examined in the works of Runstadler et al (1963), Kim et al (1973), and Falco (1974). It should also be kept in mind that for convected camera studies the boundary layer is continually growing as the cameras and probe are convected with the flow.

The photographs used in this section are taken directly from the video screen. In several cases, tracings from the video screen are used when the picture quality was poor. When a tracing is presented, it will be noted as being such.

5.B Flow Visualization

Flow visualization using the end-on view was somewhat hampered by the limited depth of field of the fiber optic lens. This means that objects only remain in focus over short distances (approximately one-half the distance from the bubble wire to the lens) in the direction with which the lens it aligned (x-direction). Usually the lens was approximately 572 to 715 viscous lengths downstream of the bubble wire and thus a single pulse of bubbles could only be observed for about 300 to 400 viscous lengths in a stationary reference frame. The pulse frequency at which the hydrogen bubble lines were generated was found to be of critical importance

in the end-on views. If the frequency of generation was too high (i.e., rapid pulses), the individual bubble lines leaving the generating wire would be obscured by previously generated bubble lines which were approaching the lens. Of course, the higher the pulse frequency, the more difficult the viewing of individual bubble lines became. The optimum frequency for bubble line generation varied with flow conditions since at higher flow velocities and/or higher y^+ the spacing between bubble lines (generated at a fixed pulse frequency) was larger. Since a different pulse frequency was used for each set of conditions, the actual frequencies used will be noted throughout the section, as is appropriate.

In the moving reference frame, the problem of appropriate pulse frequency became even more complicated. When the lens was convected downstream, the relative speed of the bubbles decreased compared to the stationary reference frame, thereby necessitating a further reduction in pulse frequencies. A problem which has yet to be resolved occurred when the traversing speed of the lens was greater than the local flow velocity. The bubbles in the lower speed regions then appeared to move away from the lens and went quickly out of focus. This problem generally arose when the convection speed

of the lens was .8 U_∞ or greater. At this speed, the high speed regions of fluid often appeared to remain stationary with respect to the bubble wire and lens and sometimes acted as "obstructing" bubbles.

It was found that maximum clarity could be obtained by minimizing the duration of the individual bubble pulses. By doing this, the bubble lines were crisp and discrete, whereas when the pulse was too long the picture often became obscured with too many bubbles.

Determination of the mean wall shear stress and turbulence intensity was done using hot film anemometry measurements, employing several different methods for shear stress evaluation. For details concerning the measurements, the reader is referred to Metzler (1980), where a complete description is given of measurement techniques and data reduction procedures.

5.C Interpretation of Video Pictures

Analysis of video tapes, or any other medium used for recording visualization data, is very difficult unless one understands what each piece of data represents. This point was illustrated by Kline in an analogy comparing turbulent boundary layer studies to a herd of elephants (Kline, 1978). Kline noted that the observer who is standing in the middle of the herd of elephants must realize what he or she is looking at and

not mistake one piece of an elephant for the whole elephant or even the entire herd. This, of course, is true when trying to piece together the boundary layer "puzzle" from bits and pieces of measured or visualized data. In the present study, a great amount of time and energy was spent deciding how to properly interpret particular bubble line patterns. For example, the question of upwellings and downward motions versus rotating vortical structures arose. Were these two phenomena different parts of one structure, or possibly the same type of structure viewed in different stages of development, or were they even two separate types of structures? Two observers could look at the same films and draw totally different conclusions as to the overall behavior unless they knew what the pictures represented and how they were obtained. Most of the confusion arises from the fact mentioned earlier, that only the effects of a vortex (and vorticity) on bubble lines can be observed, not the actual vortex itself. This subsection explains how the observable effects of a vortex on the bubble lines can be related to the characteristics of the vortex itself.

The effects of the vortex will be visualized differently for different locations of the vortex relative to the bubble lines. In all cases, the bubble

lines start as a discrete row of bubbles (usually horizontal in these experiments). Before the bubbles leave the bubble wire, they appear as a horizontal line passing across the entire video screen.

Once a bubble line leaves the wire, it may evolved into one of several different patterns. Each pattern, although different in appearance, is speculated to be generally representing a different aspect of one dominant flow structure, namely longitudinal vortices. This point is dramatized shortly in Figures 26 and 27 where bubble patterns are shown to differ depending on the distance the bubble wire is from the vortex core. In each case, as will be shown, the patterns appear drastically different yet are a result of the same axial vortex.

By oversimplifying the three-dimensionality of the axial vortex motions, much relevant information can still be gained. Assume a combined Rankine type vortex in an otherwise irrotational flow field as shown below.

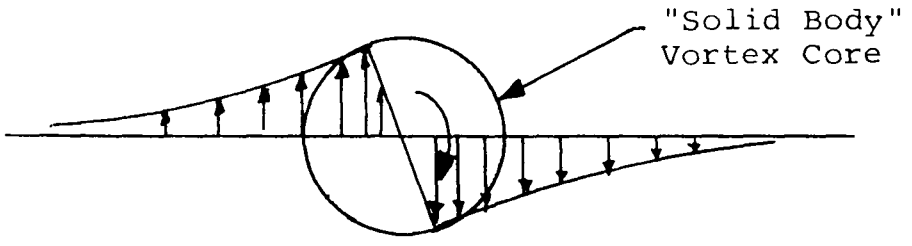

FIGURE 25 - Rankine Vortex

The core of the vortex, (the region $0 < r < r_c$, where r_c is the radius at the outer edge of the core), can then be written as:

$$V_{\theta c} = \Omega r$$

where $V_{\theta c}$ = tangential velocity

Ω = angular velocity

Outside the core of the vortex, it is then assumed that the flow behaves as a free vortex where:

$$V_{\theta o} = C/r$$

where $V_{\theta o}$ = tangential velocity

C = constant

r = radius

At the outer edge of the core, where $r = r_c$, the tangential velocity of the core must match that of the region outside the core, thus:

$$V_{\theta c} = V_{\theta o} \quad \text{at} \quad r = r_c$$

or

$$\Omega r_c = C/r_c \ .$$

Solving for C: $C = \Omega r_c^2$.

Now: $V_{\theta o} = \Omega r_c^2/r$ for $r > r_c$.

In the core, which rotates as a solid body, the distance traveled along an arc for a given radius is:

$$\Delta s = r\Delta\theta_c$$

where Δs = arc length

$\Delta\theta_c$ = change in angle .

Rearranging: $\Delta\theta_c = \Delta s/r$.

Since by simple dynamics: $\Delta s = V_\theta \Delta t$, where Δt is a time interval .

It can be written that: $\Delta\theta_c = V_\theta \Delta t/r$.

Simplifying: $\Delta\theta_c = \Omega\Delta t$ for $r < r_c$.

Similarly for the region outside the core:

$$\Delta\theta_o = V_{\theta o}\Delta t/r$$

or

$$\Delta\theta_o = \Omega(r_c/r)^2\Delta t$$

$$= \Delta\theta_c(r_c/r)^2. \qquad (1)$$

This equation can now be used to simulate the bubble line patterns which one would expect to observe in end view when an initially horizontal bubble line is affected by a vortex aligned in the direction of the flow. For example, if the bubble wire happens to pass directly through the center of the vortex, the simulated pattern in Figure 26a would be expected to result. Several points on the bubble line are numbered in order to make the tracking of each point (bubble) easier. It should be remembered that this simulation of the bubble line pattern is only an idealization and does not reflect the complexity or exactness of the bubble line deformation patterns which actually occur in the boundary layer. It is important to note that strongly similar patterns were observed in the present study, and use of this graphical simulation technique greatly aided in the understanding and quantitative interpretation of

axial vortex phenomena. Figure 26b shows a picture taken from the video screen in which the bubble wire does indeed pass through an axial vortex center. Note the striking similarity between the bubble pattern in this picture and the simulated pattern in Figure 26a.

Several other examples comparing simulated results with experimental observations are shown in Figures 27a through 27d, with the location of the bubble wire varying from 1/2 radius away from the vortex center to 3 radii away. Note that when the wire is 2 radii or more away from the center, the resulting pattern is very much like that of an upwelling (or downward motion if the wire is above the vortex). More will be said on this point later.

5.D Experimental Results (Quantitative)

5.D.1 Presence of Axial Vortical Structures

The presence of axial vortical structures was established using the end view visualization scheme. The end view combined with the plan view alleviated a problem encountered by past researchers (Offen and Kline, 1973; Praturi and Brodkey, 1978) which was an inability to determine the sense of rotation of axial vortex structures when using a single side or plain view scheme alone. Viewing the axial vortices along their axis of rotation is equivalent to studying

transverse vortex motions using a side view, where the sense of rotation was observed by Nychas (1973) to be quite easy to detect.

It was discovered that much of the axial vorticity in the region $y^+ < 60$ is manifested in the appearance of upwellings and downward motions as was suggested by some observers at the Stanford Meeting in 1978. This statement must be taken with caution for two reasons: (1) the upwellings and downward motions appear to be caused by axial vortices which are relatively far away, (say greater than 2 core radii), from the wire location and thus are regions which do not reveal the effects of the rotating core as strongly as points closer to the core (see Figures 26 and 27); and (2) while approximately 60% or less (depending on Reynolds number) of the wall region flow structures observed did not possess a noticeable w-component velocity gradient normal to the wall, i.e. $\partial w/\partial y$, at least 40% or more of the axial structures, in the region $y^+ < 60$, were observed to be true rotating vortical structures possessing both $\partial v/\partial z$ and $\partial w/\partial y$ vorticity. Figures 28 and 29, respectively, show typical sequences where both upward motions and revolving vortical structures can be observed.

Figure 28 is an end view sequence for Re_θ = 1020 with the hydrogen bubble wire located at y^+ = 34. Since it has been hypothesized that the so-called upwellings may merely be the appearance taken on by the hydrogen bubbles which are affected by the part of the vortex fairly far (say, 2 radii away) from the center, the reader should compare Figures 28 and 27c. Note the similarity between the bubble patterns in these pictures. In Figure 28, the bubble pulse frequency was set at approximately 1/2 Hz in order to eliminate extraneous bubbles which obscure the picture. The bubble pattern observed in Figure 28 is believed to be the result of a pair of counter-rotating axial vortices centered at approximately y^+ = 50. The vortex rotating in a clockwise sense is located at the extreme right, just out of the picture while the vortex with a counterclockwise sense of rotation is located slightly to the right of the center of the picture. Flow structures of the type shown in Figure 28 are commonly observed at all y^+ locations (as will be discussed shortly) and for all Reynolds numbers examined.

The hydrogen bubble line pictures shown in Figure 29, taken at Re_θ = 1020, reveal a rotating structure rather than an upwelling behavior. The wire is located at y^+ = 14, but the patterns observed here

are typical of those observed at most other y^+ locations. In this figure the wire appears to pass through a vortex center, similar to the configuration shown in Figure 26. The core is visible in this sequence and is approximately 25 dimensionless units in diameter (the measurement technique used to establish vortex diameters is discussed in the section on vortex diameters). Note that the differences between a rotating structure and an apparent upwelling are readily apparent even though both phenomena are believed to be manifestations of axial vortices occurring in the wall region of a turbulent boundary layer.

Since rotating axial vortical structures are present a substantial percentage of the time, a tabulation was done to determine the y^+ locations where such structures occur most frequently. Rotational structures, upwellings, and downward motions were categorized according to bubble line appearance. If the bubble line appeared as in Figure 26 or Figures 27a or 27b, the pattern was considered to indicate the immediate presence of a rotational structure, whereas if the bubbles took on an appearance similar to Figures 27c or 27d, this was felt to be indicative of an upwelling or downward motion. Since the field of view was normally $200 < z^+ < 450$, more than one bubble

pattern was frequently detected on a single bubble line. In this case, each pattern was classified separately according to the above guidelines.

Figure 30 shows the distribution of rotating axial vortical structures compared to upwellings and downward motions, as observed for $3 \leq y^+ \leq 60$. It can be observed from Figure 30 that the greatest percentage of rotating axial vortical structures coincided with the maximum Reynolds number examined, i.e., $Re_\theta = 2200$. For this Reynolds number, the greatest degree of vortical action was observed with the bubble wire located at $y^+ = 6$, where 86% of the total samples were observed to represent rotating vortices. Since each bubble pattern was only categorized as depicting either (1) a rotating structure or (2) an upwelling or downward motion, the percentage of upwellings and downward motions is the remainder not determined to represent rotational structures. Since the pulse frequency at which bubble lines were generated was only about 0.5 Hz, which was a necessary condition for optimum end view visualization, the total number of data samples comprising each data point in Figure 29 usually varied from 20 to 30 depending on how long each sequence was recorded.

Although there is an apparent increase in observed vortical activity at the higher Reynolds numbers, all three data bases shown in Figure 30 indicate that the region for $6 < y^+ < 30$ displays the most active vortical behavior. From Figure 30 it appears that recognizable vortices become less apparent as y^+ is increased beyond 30. Generally, for $y^+ > 30$ the observed behavior changes from one where vortical structures are dominant or at least equally probable, to one where upwelling and downward motions are the more dominant flow structure. The percentage of vortical structures observed at a given y^+ location can be noted to vary quite substantially (often by a factor of 2) from one Reynolds number to the next. This is felt to be attributable not to a true Reynolds number change but to the effect the time-scales of activity (which decrease with increasing Reynolds number) have on the interpretation of the bubble line patterns. For a fixed viewing distance from the bubble wire, more activity can be observed in the camera field of view for each bubble line as the Reynolds number increases. Thus, at higher Reynolds numbers many patterns which initially appear characteristic of an upwelling or downflow will evolve into a pattern illustrating rotation during the period that the bubble-line is in

view. In the course of the counting procedure precedence was given to the rotational patterns, which would explain the apparent predominance of vortical patterns at higher Reynolds numbers.

5.D.2 Location of Axial Vortex Centers

Having established axial vortices to be present, the data was examined to determine the location of the vortex centers. This was accomplished by observing the bubble patterns and determining if the pattern observed was similar to the rotational patterns depicted in Figures 26a and 26b. If the patterns were similar, then it was assumed that the bubble time-line had been generated when the bubble wire passed through or very near a vortex center and thus the pattern could be used to locate the approximate center of an axial vortex. Results summarizing the bubble patterns observed are given in Tables 2, 3, and 4. The location of directly identifiable vortex centers is the C^+ column in these tables. In general, the location of the vortex centers varied from $y^+ = 11$ to $y^+ = 37$, with the greatest percentage of vortex centers being observed for $17 < y^+ < 31$. The mean average C^+ location varied from $\bar{C}^+ = 22.2$ for $Re_\theta = 1020$ to $\bar{C}^+ = 25.9$ for $Re_\theta = 2200$, with $\bar{C}^+ = 22.8$ for $Re_\theta = 1600$. It is clear from the results that the centers of the

vortices do not occur consistently at the same y^+ location. This is believed to be a result of the axial vortices migrating away from the surface as they are stretched downstream (see discussion of this point in Section 5.F.5).

In the results discussed above, only those bubble line patterns which revealed a directly identifiable axial vortex were used to establish the locations of vortex centers. To check the consistency of that data, a method was devised which utilizes all bubble line patterns which indicate the presence of an axial vortex (but which may not allow the direct identification of a vortex) to establish the approximate distribution of the locations of all detectable axial vortices.

Using the bubble line pattern data in Tables 2 through 4 and the average apparent radii measured for each bubble line pattern which reflects rotational behavior, an approximate center location was determined by subtracting or adding the appropriate number of apparent radii either from or to the wire location. For example, for Re_θ = 1020 at y^+ = 3 several structures appeared to be 2 radii below the vortex center. By referring to Table 5, the apparent average radius at y^+ = 3 is 9.17 dimensionless units. Thus by adding two

radii (i.e., 2 times 9.17) to $y^+ = 3$, the estimated center of the vortex is given by:

$$C^+_{est} = 3 + (2*9.17) = 21.3.$$

Using the above method, the approximate centers for all the pattern data listed in Tables 2, 3, and 4 were determined and are presented as histograms in Figures 31, 32, and 33, respectively.

For $Re_\theta = 1020$, the probable location of the vortex centers is seen in Figure 31 to be in the range $y^+ = 21\text{-}25$. The mean average C^+, found by the second method, is $\bar{C}^+_{est} = 21.9$ at $Re_\theta = 1020$, which agrees quite well with $\bar{C}^+ = 22.2$ determined by method 1. Figure 32 indicates the most probable location for C^+ for $Re_\theta = 1600$ to be in the range $y^+ = 15\text{-}35$ with a relatively uniform distribution over this region. The average C^+ for $Re_\theta = 1600$ is $\bar{C}^+_{est} = 25.6$, slightly higher than the mean C^+ of 22.8 determined using the direct visualization method. For $Re_\theta = 2200$, C^+ values appear to be more uniformly distributed over a range of y^+ values, as shown in Figure 33. The most probable region for C^+ is the range $y^+ = 26\text{-}30$, while $\bar{C}^+_{est} = 29.1$ which again is slightly higher than $\bar{C}^+ = 25.9$ determined by the direct identification method. The

variation in the average location of the vortex centers determined by the two methods is believed to be attributed to both the use of average apparent vortex diameters to calculate the C^+ values by method 2, and the limited sample sizes available for method 1. Note that the apparent vortex diameters are not true vortex core diameters, and use of the averaged values may bias method 2. The concept of apparent diameters (sizes) is explained in Section 5.D.5. It should be pointed out, however, that the average identifiable core locations are within ±13% of each other for the worst case comparison of the two different methods.

Several other researchers have estimated the location of axial vortex centers. From their probe correlation data, Blackwelder and Eckelmann (1979) speculated the centers of axial vortices to be located in the region $20 < y^+ < 30$, which is consistent with the present investigation. Kreplin and Eckelmann (1979) also speculate that the average y^+ location of the vortex centers should be approximately $y^+ = 30$. Praturi and Brodkey (1978) estimated the locations of axial vortex centers to be in the range $y^+ = 5\text{-}15$ but extending out to $y^+ = 10\text{-}25$. Their results do not compare well with the present study, since the present work observed essentially no vortex centers to be

present in the region $5 < y^+ < 11$, although a high concentration of centers was observed in the region $11 < y^+ < 25$. Since the Reynolds numbers for the results of Praturi and Brodkey were close to the $Re_\theta = 1020$ of the present study, one is inclined to suspect that their method of visualization and observation may have influenced their results. It is felt that their visualization technique may have made it difficult to accurately locate the wall boundary in their pictures, and thus may have biased their estimated locations of vortex centers. Additionally, as was mentioned above, the definition of a vortex center is difficult with the bubble time-line visualization, and it would appear to be even more subjective when evaluating single particle motion in an axial direction using a side view. Possible misinterpretation of the flow behavior in the wall region and viscous sublayer could have strongly influenced their description of observed vortex behavior.

5.D.3 Pairs of Counter-Rotating Axial Vortices

The definite establishment of rotating vortical structures aligned in the streamwise direction led to an investigation of the hypothesis (Kline, 1967; Willmarth, 1977; Blackwelder and Eckelmann, 1979; and others) that axial vortices occur in counter-rotating pairs, and as such strongly influence flow behavior

near the wall. Bubble line patterns revealing such a system of counter-rotating vortices are shown in Figures 35 and 36.

Before examining Figures 35 and 36 in detail, a brief qualitative description of the bubble line patterns one expects to result from a counter-rotating vortex pair will be given. Assume a pair of counter-rotating axial vortices to exist, and to be observed in end-view. Referring to Figures 26 and 27, one can predict the appearance of a line of bubbles under the influence of such a pair of vortices. Figure 34 depicts how a bubble line will be affected by a pair of counter-rotating vortices when the bubble wire is located approximately one radius below the vortex centers. As shown in Figure 34a, the axial vortex pair causes low speed fluid near the surface to be swept together and upward between the vortices. During the early stages of this lift-up, the bubble line pattern develops a horseshoe shape. As the low-speed fluid is lifted past the vortex centers, the bubble line pattern begins to take on a mushroom shape as shown in Figure 34b. Normally, the lifted low-speed fluid does not have sufficient momentum to continue straight upward, and thus when it moves beyond the vortex cores it spreads in the spanwise direction as shown in Figure 33c. Note

the similarity between Figures 34c and 26b. Variations in the initial location of the bubble wire will result in different bubble line patterns, but as was shown in Section 5.3, these variations in patterns can be simulated, anticipated, and related to the visualization data to detect the presence of vortex pairs. A more detailed qualitative discussion of the evolution of a loop vortex will be found in Section 5.F.5.

Figure 35 is a combination top and end view picture at Re_θ = 1600. The two views are scaled identically and are oriented such that they represent an orthographic projection as shown in Figure 14. The flow is top to bottom in the top view and out of the paper in the end view. The top view of Figure 35a shows the alternating low- and high-speed regions associated with low- and high-speed streaks. Note that in the top view the bubble wire is the white line passing under the frame and sequence numbers. The low-speed regions are those closest to the bubble wire. As can be observed in the corresponding end view, higher speed regions move downward (as seen in the end view) toward the surface, whereas the low-speed regions move outward, away from the surface. This strong vertical movement was observed to be universal for all low- and high-speed regions. In this two picture

sequence, the development of two pairs of axial vortices can be observed. In Figure 35b, taken 0.16 seconds after Figure 35a, the effect of one pair, labeled "A", is seen observed in the bubble line pattern at the center of the picture which appears as a "horseshoe" shape. The other pair, labeled "B", occurs at the extreme right of the picture and causes the appearance of a "mushroom" shape in the bubble pattern. Recall that it is commonly observed that a "mushroom" pattern normally occurs in a bubble line under the extended influence of a CRAV, as previously discussed. Generally, a "horseshoe" pattern will evolve into a "mushroom" as low speed fluid is lifted away from the surface by a CRAV.

Figure 36, another combined top and end view, shows once again the effects on the bubble line pattern of a pair of counter-rotating axial vortices, labeled "A". The bubble wire is at $y^+ = 14$ and is believed to be approximately one radius below the vortex centers. The appearance of the vortex centers to move slowly downward is a result of the angle at which the fiber optic lens was oriented relative to the surface. The line of sight of the lens, as previously mentioned, is oriented at approximately 4° to the plate surface, thus giving the illusion of a slow downward shifting in the

bubble pattern. Of importance is that the observer can see the entire "mushrooming" process described in Figure 34. The size of these vortices is approximately $D^+ = 30$, with a core vorticity of approximately $\omega^+ = 0.4$ and a circulation of about $\Gamma^+ = 280$. The effects of another pair of vortices, labeled "B", are also seen but not as clearly as "A." However, the low-speed region is again seen to be associated with these vortices as well as the same lifting of low-speed fluid between them.

In order to determine how commonly counter-rotating axial vortex pairs occur, bubble line patterns were examined and the percentage of the total observations which clearly revealed pairs of counter-rotating axial vortices was established as a function of wire location, y^+, for $Re_\theta = 1020$, 1600, and 2200. The presence of the CRAV (counter-rotating axial vortices) was found to be somewhat dependent on Reynolds number. By referring to Figure 37, a general trend is noted where the observed percentage of CRAV for a given y^+ location increased with increasing Re_θ. For example, at $y^+ = 17$-19, the percentage of CRAV observed at $Re_\theta = 1020$ is 20%, increasing to 26% for $Re_\theta = 1600$, and finally to 33% for $Re_\theta = 2200$. This observed increase in the percentage of CRAV with Re_θ is felt to most

probably be the result of scale and strength changes. First, as Re_θ increases, the strength of the vortices increases and the scale decreases. Since the viewing field was of a constant dimensional size, this means that the non-dimensional size of the viewing field increases with Re_θ. Thus, it may be possible to observe more vortices than at lower Reynolds numbers and, due to the increased strength, they develop faster and the pairs are more easily detectable. It is generally felt that the CRAV is probably a more dominant structure than shown by Figure 37, and that if sufficient development distance were available for observation at all Re_θ, the percentage of CRAV would probably approach or exceed 50%.

5.D.4 Spacing Between Counter-Rotating Axial Vortices

The spacing, Δz^+, between adjacent axial vortices was determined by visual measurement as soon as the vortices were detectable after the bubbles left the wire. Figure 38 is a schematic of a typical bubble pattern (similar to Figures 35 and 36). By estimating the center location of each vortex (with the aid of Figures 28 and 29), the distance between these two center points could be established.

The average spacing, Δz^+, between two adjacent counter-rotating vortices reveals an interesting pattern

for most Reynolds numbers tested. As illustrated in Table 5 and Figures 39 through 41, the most evident characteristic is that the minimum average Δz^+ spacing occurs very near the most probable location of the vortex centers as determined previously (Section 5.D.2). For Re_θ = 1600, Δz^+ = 45 at y^+ = 23 and is actually the least spacing observed for this Reynolds number. Recall that the greatest frequency of vortex centers also occurred at essentially the same y^+. As the y^+ location of the bubble wire is varied from y^+ = 23, the spacing becomes greater, reaching local maxima at the lowest and highest y^+ tested. For y^+ = 9, Δz^+ was approximately 58 and for y^+ = 32, Δz^+ was found to be 62.

For Re_θ = 2200, the results are rather similar to those at Re_θ = 1600. The local maxima Δz^+ again occur at the lowest and highest y^+ tested. At y^+ = 6, Δz^+ is 69 and at y^+ = 49, Δz^+ is 85. The minimum Δz^+ is 51 and was found at y^+ = 31. Again, this minimum spacing is in the region where the frequency of vortex centers was found to be the greatest, i.e., $19 < y^+ < 31$.

Both Figures 40 and 41 show clearly that identifiable vortex pairs move together as y^+ increases up to the most probable location of the vortex centers and then move apart again, generally supporting

Willmarth's theory of mutual inductance in loop vortices in a turbulent boundary layer, which was discussed in Section 1.

The average spacings between vortex centers determined for Re_θ = 1020 generally support Willmarth's theory of mutual inductance, although it appears that these are two regions of minimum spacing (at y^+ = 9 and 20), and a very sharp increase in spacing as y^+ is increased to 30. It should be noted that y^+ = 20 is the location where vortex centers were observed most frequently for Re_θ = 1020. The reason for this more irregular pattern of vortex spacing is uncertain, but it is speculated that a lack of data and/or difficulties in data acquisition and pattern interpretation may be responsible.

Some other researchers have estimated the spacing between centers of counter-rotating vortices. Blackwelder and Eckelmann (1979) and Kreplin and Eckelmann (1979) estimated, based on wall behavior, the spacing to be approximately Δz^+ = 50 at y^+ = 30. This result is quite close to the data of the present investigation, e.g., Δz^+ = 51 at y^+ = 31 for Re_θ = 2200.

Lee, Eckelmann, and Hanratty (1974) reported the results of tests performed at several different Reynolds numbers. A single value of Δz^+ = 50 was

reported for estimated spacing between vortex pairs, although no y^+ value could be specified for the location of the vortex centers. The author wonders if the implication is that Δz^+ is constant for all y^+ or if the data was insufficient to allow determination of vortex locations. Another question which arises regarding Lee's investigation is whether or not Δz^+ varied with Reynolds number.

One observer, Smith (1978), using top view hydrogen bubble wire visualization of streaks in a moving reference frame was able to observe spacings between axial vortex pairs which varied from $\Delta z^+ = 50$ to 25 over non-dimensional time periods of $\Delta t^+ = 50$. Smith's study, done at $Re_\theta = 1200$, appears to be consistent with the results of the present study which indicates a minimum Δz^+ of 31 at $Re_\theta = 1020$.

5.D.5 Sizes of Axial Vortices

Measurement of the diameters of the vortical structures (not necessarily CRAV) proved to be more difficult than one would expect. For example, if a bubble line pattern appeared as shown in Figure 27, originally a measurement was taken across the entire visible (apparent) diameter. Unfortunately, this apparent diameter is not the actual diameter of the vortex core. It was determined that unless a bubble

line was generated in the center of a vortex, there is no accurate way to measure the actual vortex core size and/or the size of the entire region under its influence. These apparent diameters are, however, useful in estimating the vortex circulation strength as will be described in Section 5.D.7. The use of a three-wire hydrogen bubble probe (see Section 4.D) allowed more accurate and meaningful measurements to be done, but did not entirely eliminate the problem of determining vortex core sizes.

A typical end view picture obtained using a three-wire bubble wire probe is shown in Figure 42. The wires are located 28 dimensionless length units apart. Thus, in this picture, the bottom wire is located at y^+ = 6, the second (middle) wire at y^+ = 34, and the top wire at y^+ = 62. One can see that the middle wire passes nearly through a vortex center (the dotted line indicates the relative location and size of the vortex core), while the configuration of the bubble line leaving the top wire indicates the top wire to be approximately two and a half radii away from the vortex center. A similar but less developed pattern is seen on the lower wire. The pattern on the lower wire is less developed due to the viscous effects near the wall, with the pattern representing a typical upwelling

type behavior. The reader can see that the determination of vortex core sizes is subject to substantial uncertainty, but the existence of vortex cores is clear. The vortex core represented by the patterns shown in Figure 42 was determined to be approximately $D^+ = 22$. Note that the effects of the vortex are felt over a region at least from $y^+ = 0$ to $y^+ = 65$. Although the actual region of influence is probably even greater, the total extent could not be determined from this picture.

The most accurate measurements of vortex core sizes were obtained when the bubble wire passed through the center of a vortex core as a bubble line was generated. In this situation the true core diameter can be measured since the effects of the entire core are reflected in the bubble line patterns (e.g. see Figures 26 and 29). In the present study, both true core diameters and apparent diameters were determined from the visual data and the findings are summarized in Table 5 and Figure 43.

A certain amount of variation was found in the measurements of vortex diameters, D^+. This variation is strongly believed to be a result of axial vortex stretching and coalescence which results in the vortices undergoing an evolutionary process during

which sizes and rotational speeds, as well as other characteristics, change with time. Thus, substantial variations in characteristics at a given location can arise since it is impossible to examine each vortex in the same stage of development. Another inherent problem encountered in studying vortices is that they frequently agglomerate (coalesce). When two or more vortices merge together, it is impossible to detect this visually. Thus, many of the determinations that were made may have been of agglomerated vortices, and thus not indicative of the characteristics of a initial, single vortex. This effect is observed not only in the determination of vortex core diameters, but also in the determination of vortex strength which will be discussed in Section 5.D.7.

Figure 43 shows the distribution of average vortex core size at the various y^+ levels. One can see that for all Reynolds numbers tested, the core size, D^+, increases slightly as y^+ is increased. Some slight deviations are seen for each Re_θ, but this may be due to the subjectivity of the measurements and the size of the population (number of samples) obtained. In some cases, the number of samples was indeed quite small, for example, for Re_θ = 1600, there were only three samples used to determine the D^+ value at y^+ = 33. The

mean average diameter for Re_θ = 1020 was calculated to be D^+ = 20, increasing to D^+ = 22 at Re_θ = 1600 and to D^+ = 31 at Re_θ = 2200. Thus the average D^+ value appears to increase with Reynolds number; however, the reason for this is uncertain.

An increase in D^+ with increasing y^+ is consistent with the idea of diffusion and/or coalescence of vorticity. Since several vortices can exist simultaneously at different y^+ levels, it is expected that vortex coalescence of one or more adjacent vortices of like rotation could occur. Although the coalescence process would result in some dissipation of the collective energy, there would be a net increase in both strength and core diameter of the newly coalesced vortex. Further support of this argument is presented in Section 5.D.7 which discusses the circulation strength of the vortices.

Praturi and Brodkey (1978), using stereoscopic visualization of particle motion, determined that axial vortices in turbulent flow were of diameters equal to 50 D^+. This is somewhat higher than the sizes observed in the present study, but again may be consequence of their visualization technique. One recalls the discussion of the difficulty in determining true core diameters using the present hydrogen bubble technique, it is

apparent that what Praturi and Brodkey may have observed in their study were apparent diameters, which would have appeared much larger than the true core diameters.

5.D.6 Axial Vorticity

For selected cases, the vorticity, ω_x^+, could be determined visually from the bubble line patterns. For the same reasons as discussed in Section 5.D.5, only the vorticity in the core is believed to represent an accurate measure of actual vorticity. Outside the core, a determination of vorticity from the bubble line patterns is not possible... only a determination of the tangential velocity, V_θ, can be made. Within a vortex core, $0 < r < r_c$, it was assumed that $V_\theta = \Omega r$, where Ω represents the solid body rotational speed. For bubble line patterns originating in the core of a vortex, vorticity was determined by measuring the angle of rotation and the period over which the rotation takes place. Figure 29 showed a bubble line pattern illustrating the rotation of a vortex core. For that sequence it was determined that the vortex core rotated through π radians in 0.25 seconds. The average angular velocity, Ω, is determined by dividing the angle rotated by the time interval over which the rotation (i.e. $\pi \div 0.25 = 12.6$ rad/sec). Since the vorticity is twice the angular velocity, the above value of Ω yields a

quantitative value for ω_x = 25.2 rad/sec. Once ω_x has been determined, it is non-dimensionalized on wall variables as shown in Appendix 1. Results are shown in Table 5.

A correlation between Re_θ and ω_x^+ is somewhat confusing and no general statement can be made concerning their relationship. In general, however, ω_x^+ was found to vary between $\omega_x^+ = 0.5$ and $\omega_x^+ = 0.2$. Larger valves of vorticity were observed for $Re_\theta = 1020$ while the smallest valves were at $Re_\theta = 2200$. Vorticities between 0.5 and 0.2 can be seen for $Re_\theta = 1600$. Note that the mean vorticity at the wall, ω_z^+, can be given by:

$$\omega_z^+ = \omega_z \nu / U_\tau^2 \qquad \text{where } \omega_z = {}^{\partial u}/_{\partial y}$$

$$U_t = \sqrt{\tau_w / p}$$

$$= ({}^{\partial u}/_{\partial y})_{\text{wall}} (\mu/\rho) \div (\tau_w/p).$$

Now $\tau_w = \mu({}^{\partial u}/_{\partial y})$ so,

$$\omega_z^+ = ({}^{\partial u}/_{\partial y}) * (\mu/\rho) \div (\frac{\partial u}{\partial y}) * (\mu/\rho)$$

$$= 1.0.$$

Thus, ω_x^+ can vary between approximately one-fifth to one-half the magnitude of the mean vorticity at the wall. From their hot film measurements, Eckelmann and Blackwelder (1979) suggested that the strength of the vorticity of the axial vorticities should be an order

of magnitude less than the spanwise vorticity at the wall, which is somewhat less than that found in the present investigation. Their lower value is most likely due to the fact that they had to infer the characteristics of the vortex from wall measurements, and could not measure the characteristics directly.

5.D.7 Circulation Strength of Axial Vortices

Vortex stretching is a dominant characteristic in turbulent boundary layer flows. By assuming that no change occurs in the axis of rotation of the vortex and requiring that the cross-section of the vortex line to be circular so that pressure gradients cannot apply torque to it, angular momentum within a vortex should be conserved as the cross-sectional area changes. Using similar assumptions, the circulation strength of the axial vortices can be determined using readily acquirable data such as tangential velocity, apparent diameters, etc. The circulation strength, Γ^+, is given by:

$$\Gamma^+ = \Gamma / \nu$$

where $$\Gamma = \oint v \cdot ds \quad \text{with } ds = d\theta dr = 2\pi\, dr$$

$$\cong V_\theta \cdot 2\,\pi r\,.$$

Now for $0 < r \leq r_c$, $V_\theta = \Omega r = \omega r/2$.

So $\Gamma = \pi \omega r^2$.

Substituting $\Gamma^+ = \pi \omega r^2/$ for $0 < r < r_c$.

Recall $\omega = \omega^+ U_\tau^2/\nu$ and $r = r^+ \nu/U_\tau$.

So $\Gamma^+ = \pi \omega^+ (r^+)^2$

$= \pi \omega^+ (d^+)^2/4$ for $0 < r < r_c$.

By simple substitution, Γ^+ can be determined in the core of an axial vortex.

Outside the core of a vortex, if the motion is irritational (as for a combined Rankine type vortex), a line integral about the core will yield a value for circulation reflecting the strength of the core alone. Thus:

$\Gamma \cong V_\theta \pi\, 2r_a$ for $r > r_c$

and $V_\theta = \Omega_a r_a$

where r_a = the apparent radius of the rotational motion

Ω_a = the apparent rotational velocity at r_a.

Thus:

$$\Gamma = \Omega_a\, 2\, \pi r_a^2 = \frac{\omega_a \pi\, D_a^2}{4} \text{ since } (\omega_a = 2\Omega_a)$$

and

$$\Gamma^+ = \pi\, \omega_a^+ (d_a^+)^2/4 .$$

Thus, by using hypothetical apparent diameters and vorticities determined <u>outside</u> of the core of the vortex in an irrotational region, it is possible to

obtain a valid estimate of the circulation strength outside of the core. These previous expressions were used to determine circulation strengths, both in the core and, using the apparent sizes and tangential velocities outside the core. The results of these calculations are shown graphically in Figures 44, 45, and 46. In general, it can be seen in Figures 44 and 45 that as y^+ increases, the circulation strength tends to increase. Deviations from this trend may be due to the same problems noted earlier concerning the difficulty in measuring the average characteristics of an evolving vortical structure and the limited sample size available at particular y^+ rotations. It is important to note that a linear curve fit of the data in curves 44 and 45 shows an almost identical correlation of Γ^+ to y^+, which indicates that almost all of the vorticity in the observed vortices must be within the core of the vortex. If that is the case, then this implies that the mechanism for the growth of Γ^+ with y^+ must be a form of vortex coalescence which occurs as the vortices move outward from the surface. Note that if Γ^+ had been found to be a constant at various y^+ locations, this would imply that simple vortex diffusion due to viscous interation with the surrounding fluid would be the dominant

mechanism for vortex growth; however, this was not the case.

The theory of vortex coalescence is further supported by the results shown in Figure 46, which indicates that Γ^+ of the core increases as D^+ in the r core increases. This behavior would be expected, since if two vortices of fixed strength and cross-sectional area merge or coalesce, the strengths should superpose linearly and the diameter of the resultant vortex should grow roughly as the linear superposition of the vortex core areas (in the absense of vortex stretching). Recalling that in Figure 43, D^+ was also shown in to increase with y^+, these findings agree with the Reynolds stress prediction that length scales and Reynolds stress increase with increasing distance from a surface.

An observation which supports the above results and speculation of vortex coalescence was made by Kim (1971) who noted a simultaneous increase in rotational speed as well as apparent vortex diameter as axial vortices (viewed in side view) moved away from a surface. He speculated that this behavior was due to some form of energy transmission to the vortex, however, he was unable to offer some mechanism to account for this observation. The author believes that the mechanism

is a process of vortex coalescence modified by vortex stretching and viscous diffusion.

5.E Transverse Vortices

Using a vertically oriented hydrogen bubble wire, transverse vortices, similar to that shown (T.V. Coordinates) in Figure 47, were observed using side view visualization for Re_θ = 1200. The strength, Γ^+, of these vortices was determined by the same technique discussed in Section 5.D.7 and was found to range from 184 at y^+ = 45 to 518 at y^+ = 75. These figures are reasonably consistent with the Γ^+ values determined for the axial vortices in Section 5.D.7. The transverse vortices' centers typically were observable from y^+ = 45 to y^+ = 75, which are higher y^+ values than those for which most the axial vortex observations were made. However, if one linearly extrapolates the data for Figures 44 and 45, the transverse data is consistent with that of the axial vortices. Thus, the transverse vortices appear to coalesce with other transverse vortices in a similar manner to the axial vortices since their strength also seems to increase with y^+. Again, this is a rational behavior, since Reynolds stresses and length scale have been shown to scale with y^+. It is believed that these transverse vortices are not the same large transverse vortices ($D^+ \cong 100\text{-}200$) as

those studied by Nychas (1973) but rather are vortices which coalesce into those observed by Nychas.

5.F Qualitative Results

5.F.1 Introduction

In Section 5.D, experimental results have been presented demonstrating the existence of pairs of counter-rotating axial vortices (Section 5.D.3). Visual evidence was also shown which indicates that these axial vortex pairs are responsible for pumping low speed fluid away from a boundary to higher y^+ locations in the wall regions. Transverse vortices occurring in the wall region flow were also examined and were found to possess circulation strengths, Γ^+, of essentially the same magnitude as the axial vortices. It is the present belief that the oberved pairs of counter-rotating axial vortices and the transverse vortices are not separate structures, but comprise the components of a stretched and lifted vortex loop of small scale which is an integral element in the turbulence production process.

There is a belief by many observers that the loop vortex (hairpin vortex, horseshoe vortex, etc.) is the predominant coherent structure in the turbulent boundary layer. As early as 1952, Theodorsen proposed the horseshoe vortex to be the main characteristic in

the boundary layer. Later, in the transition experiments of Hama and Nutant (1963), it was theorized that many of the flow characteristics within the boundary layer could be explained by the presence of loop vortices. Others who have speculated that the loop vortex are a key element in turbulent boundary layers are Runstadler et al (1963), Offen and Kline (1973), Smith (1978), Brown and Thomas (1977), and Tu and Willmarth (1966) to name a few. Based on the present results, it is felt that the loop vortex does provide an accurate explanation and perhaps a kinematic model for the flow behavior observed in turbulent boundary layer studies.

The following is a hypothesis of how loop vortices form and their function within a turbulent boundary layer. This is a synthesis based on both quantitative and qualitative information available from the present study, and other limited information available from previous wall region studies.

5.F.2 Definition of the Loop Vortex Model

A schematic representation of a hypothesized loop vortex is shown in Figure 48. Many of the results presented in Sections 5.D and 5.E in this report are consistent with the presence of such loop vortices as

the predominant flow structure in the wall region of a turbulent boundary layer.

The evolution of the loop vortex within a boundary layer flow is extremely complex. Thus, it was felt that the description of such an evolutionary process would be eased by breaking the vortex loop into three different parts, thus facilitating the discussion of the structure and development of each part. Referring to Figure 48, the front of the loop, called Region 1, consists of a transverse vortex, which is believed to link the two axial vortices. This transverse vortex was shown to possess a Γ^+ consistent with that of the axial vortices. The two counter-rotating axial vortices, labelled Region 2, are felt to be the key region influencing the behavior of the wall region and to which most of the results of this investigation apply. Region 3 is the "tail" of the loop vortex which is hypothesized to end in a vorticity sheet and is believed to be the most strongly influenced by the wall friction.

5.F.3 Origin of Loop Vortices

Before discussing the evolutionary process through which loop vortices pass, it is important to establish a hypothesis concerning the origin of such loop vortices. The preliminary investigations of Smith

(unpublished) concerning the flow structure generated by the flow over a hemisphere have provided an indication of how loop vortices can originate. It was observed that a Helmholtz type instability occurring in the separated shear layer developing from the flow over a hemisphere results in the formation of loop vortices essentially identical to those considered in the proposed model of the present investigation. It is believed that the formation of loop vortices in a turbulent flow is the result of the presence of a low speed fluid region (i.e., the low speed streak) which creates the instability conditions, via a shear layer, necessary to spawn loop vortices. The resultant low speed fluid which is lifted between the pair of counter-rotating axial vortices (Region 2) representing the legs of the vortex loop acts to reinforce the low speed streak and thus sustain the instability mechanism (shear layer) and perpetuate the formation of subsequent vortex loops.

5.F.4 Axial Vortices (Region 2)

5.F.4.a Evidence of Low Speed Fluid Lift-Up from the Wall Region

With the use of the three-wire hydrogen bubble wire probe, substantiation of low speed fluid lift-up by CRAV was observed as illustrated in Figure

49. It was observed that as the result of a viscous-inviscid interaction between the wall region fluid and the counter-rotating axial vortices, wall region fluid is "picked up" from the wall through the effects of the vortex flow field. In Figure 49, the effects of two pairs of CRAV, which are present (their approximate location is shown with dotted lines) at "A" and "B" ($y^+ \simeq 24$) on bubble lines generated by three-wire probe are illustrated. It can be observed that each pair of vortices is responsible for a distinct upwelling. At $t^+ = 0$, the bubbles have just left the bubble wires. By $t^+ = 4$, the upwelling is beginning to develop at both "A" and "B". Low speed fluid is observed to have begun to be lifted off the wall by the CRAV at approximately $t^+ = 8.1$. At $t^+ = 12.1$, the lift-up of fluid has been well established. This sequence is essentially the behavior predicted by Walker and Doligalski in their theoretical analysis of the effects of vortices on a viscous boundary.

5.F.4.b Progression of Low Speed Fluid after Lift-Up

Without exception, when a pair of counter-rotating axial vortices was observed, there was a movement of low speed fluid between the two vortices as shown in Figures 34, 35, 36, and 49. Additionally, when a top view was combined with an end view, the

presence of a CRAV in end view was always observed to be associated with the formation of a low speed streak region in top view. Figure 50, which is quite similar to Figure 36, shows the appearance of bubble line patterns when observed in a reference frame moving at $U_{ref} = 0.2U_{\infty}$ ($U^{+}_{ref} = 4.5$). At $t^{+} = 0$, the CRAV lifts low speed fluid away from the surface, which appears as an upwelling at point "A". The same behavior is observed at "B" although this upwelling is in an earlier stage of development. The reason for this variance in stages of development in Figure 50 is believed to be due simply to the temporal and spacial variations in vortex evolution as discussed in Section 5.D. Concentrating on event "A", the low speed fluid is observed to take on the appearance of a horseshoe at $t^{+} = 5.5$. This horseshoe appearance was observed to occur when the bubbles passed the center location of the vortices and were approximately one radius from the vortex center. In the top view ($t^{+} = 5.5$), one can see the axial vortices move together as they mutually interact. As the low speed fluid is lifted past the vortex centers, the CRAV cause the fluid to spread laterally. At $t^{+} = 10.9$, this lateral spreading, termed "mushrooming", has become quite pronounced.

5.F.4.c Axial Vortices on Higher Speed Fluid

In addition to the lifting of low speed fluid away from the surface, high speed fluid was observed to move toward the plate in conjunction with vortex loop behavior. In all observations, the high speed fluid affected by axial vortices was observed to move toward the plate. Often, this movement toward the plate was identified with two counter-rotating axial vortices as seen in Figure 51 (marked "A" and "B"). Note that these two vortices are NOT the legs (Region 2) of one vortex loop, but rather are speculated to be the legs of two adjacent loop vortices, as indicated in Figure 51. As shown, the fluid near the top wire (at $y^+ = 56$) is moving toward the surface between the vortices at "A" and "B". As the fluid impacts the surface, it spreads out laterally. This results in a region of high shear between the low and high speed fluid and the high speed fluid is subsequently slowed. This now low speed fluid is then "swept up" by two adjacent pairs of CRAV and concentrated between each vortex pair as previously discussed, resulting in the formation or reinforcement of low speed regions which subsequently initiate the formation of new vortex loops. These new loops again cause high speed fluid to be brought toward the wall and the process repeats in a cyclical fashion.

5.F.5 Loop Vortices Evolution as a Whole

Figure 52 is the overall, idealized interpretation of how a loop vortex evolves both spacially and temporaly. The origin of loop vortices has been described previously in Section 5.F.3. Once a loop vortex is formed, Region 1 (the region effected by the transverse vortex) begins to rise as shown in Figure 52a. This region is observed to rise at the fastest rate. This is felt to be due to the mutual induction between the transverse portion of the loop and the axial legs in proximity to the transverse portion (i.e. Regions 1 and 2) shown in the top view of Figure 52a. In addition, since the loop must in practice coexist with other loops of corresponding sign of rotation, there will be mutual induction effect from these other loops causing an initial vertical motion. Note also that the transverse vortex keeps the leading portion of the axial legs from moving together as readily as if the legs were of infinite axial extent. The axial length of Region 1 is entirely uncertain.

As Region 1 moves further from the surface, Region 2 begins to move away from the surface as well. The mutual induction effect between the pair of CRAV constituting the vortex legs is most evident in this region. The theory of mutual inductance was supported

quantitatively in Section 5.D.4. Recall that the spacing, Δz^+, between two adjacent CRAV was shown to decrease with increasing y^+ until Δz^+ reached a minimum. After this minimum was reached, Δz^+ began to increase as y^+ increased. It is speculated that as the loop rises (due to induction) it migrates into regions of continually increasing velocity (as y^+ increases) and thus becomes stretched. This subsequent stretching causes the vorticity, ω_x^+, to increase. As ω_x^+ increases, the mutual induction is speculated to accelerate. Thus, different regions along the length of the loop will lift at different rates.

Figure 52c shows that as vortex lifting continues, the vortex legs in Region 2 will continue to squeeze together due to induction effects. The resultant inviscid-viscous action between the vortex legs and low speed fluid adjacent to the surface causes this low speed fluid to be swept rapidly together (in the spanwise direction seen in the end view) and outward as the legs move together and outward. Simultaneously, the entire loop is continually stretched with a subsequent increase in vorticity, ω_x^+. The loop continues to lift as observed in Figures 52d and 52e and the "mushrooming" effect, as described in Section 5.F.4.b, becomes evident.

Region 3 was observed to behave in a most interesting manner. Past observers have been unable to detect the way that the loop vortex closed at its upstream extremes. From observation of the moving reference sequences, the rear of the loop vortex was observed to turn outward, taking on a spanwise orientation as seen in Figure 53. By this, it is meant that the tails of the CRAV become aligned with the z-axis and do not appear to form a closed loop, as many observers have speculated. In addition, as the vortex tubes of the CRAV turn outward, they cease to be rotational, but terminate into a shear layer near the surface. This orientation is not conducive to mutual induction; thus Region 3 does not lift as do Regions 1 and 2, since rotational vorticity does not occur in Region 3.

5.G Other Loop Vortex Hypothesis

It was discussed in Section 5.E that as early as 1952 observers were speculating that loop vortices were a dominant characteristic within turbulent boundary layers. The recent work of Head and Bandyopadhyay (1978), which employed combined smoke visualization and hot wire anemometry, speculates that the loop vortex is the most significant feature of the boundary layer. Their tests, ranging from Re_θ = 1000 to 7000, indicated

that "most large scale features appeared to consist almost solely of random agglomerations of such (horseshoe) vortices." It was noted by Head and Bandyopadhyay that there appeared to be no obvious length scale nor periodicity. Their results further indicated that the spacing between the legs of the horseshoe decrease with increasing Re_θ and that the angle at which these vortices appear is approximately 40° to the horizontal.

Even more recently, Metzler (1980) has hypothesized that the loop vortex is responsible for streak formation. He observed ejections of fluid from near the wall which appeared to originate from low speed streaks in the form of loop-like vortical structures. Further observations showed that groups of three to five vortex loops appeared with a frequency consistent with that of the local bursting frequency. Similar to the present investigation, Metzler observed that the low speed streaks acts as the origin for the formation of one or more loop vortices.

5.H Summary

From the results of the present study, it appears that axial vortices, by inducing movement of low speed fluid away from and high speed fluid toward the surface, are the mechanism for facilitating momentum

exchange in the wall region of a turbulent boundary layer. These axial vortices appear to be part of a predominant feature of the boundary layer...the loop vortex. This loop vortex consists of three basic regions: 1) a pair of counter-rotating axial vortices which pump low speed fluid up between them, 2) a transverse vortex connecting the downstream extremes of the axial vortices and, 3) sheets of vorticity, aligned with the axis perpendicular to that of the flow, at the upstream extreme of each axial vortex.

The loop vortex originates from a flow instability created by the presence of low speed fluid regions (i.e. low speed streaks). Thus, once a loop is formed, the low speed fluid pumped between its legs (axial vortices) perpetuates the condition for spawning more loop vortices by reinforcing the low speed streak regions sustaining the instability mechanism.

The loop having been formed, proceeds through its evolution in which the transverse vortex rises at the fastest rate from the surface. The axial vortices rise and move toward each other through a mutual induction process. The vorticity sheets do not rise since rotational vorticity is not present in these regions.

An increase in the circulation strength of the axial vortices, Γ^+, was observed to occur as y^+ was increased, and is hypothesized to be the result of coalescence of loop vortices in the wall region. This occurred concurrently with an increase in size of the vortex cores, which is in agreement with the observations of Kim (1971).

TABLE 2
Percent of Observed Bubble Pattern Appearances for Re_θ = 1020

	BELOW C^+					ABOVE C^+			
y^+	>2R	2R	1R	1/2R	C^+	1/2R	1R	2R	>2R
2.9	40	48	12	0	0	0	0	0	0
5.7	0	46	50	4	0	0	0	0	0
8.6	0	17	70	4	0	0	0	0	0
11.4	0	0	71	16	13	0	0	0	0
14.3	0	0	68	14	14	4	0	0	0
17.1	0	0	56	16	20	8	0	0	0
20.0	0	0	31	16	25	9	19	0	0
22.9	0	0	32	12	16	16	24	0	0
28.6	0	0	32	18	9	27	14	0	0
34.3	0	0	0	5	29	19	23	19	5

TABLE 3
Percent of Observed Bubble Pattern Appearances for Re_θ = 1600

	BELOW C^+					ABOVE C^+			
y^+	>2R	2R	1R	1/2R	C^+	1/2R	1R	2R	>2R
9.4	13	17	67	3	0	0	0	0	0
14.1	15	0	65	15	5	0	0	0	0
18.8	7	7	52	12	22	0	0	0	0
23.5	0	4	20	28	32	16	0	0	0
28.2	0	0	0	12	20	28	24	16	0
32.8	0	0	0	0	0	12	32	36	20

TABLE 4
Percent of Observed Bubble Pattern Appearances for Re_θ = 2200

	BELOW C^+					ABOVE C^+			
y^+	>2R	2R	1R	1/2R	C^+	1/2R	1R	2R	>2R
12.4	0	5	72	17	6	0	0	0	0
18.5	0	0	65	17	13	5	0	0	0
24.7	0	0	30	22	19	15	14	0	0
30.9	0	0	4	27	18	24	27	0	0
37.1	0	0	0	0	10	35	45	10	0
43.3	0	0	0	0	0	9	48	34	9
49.4	0	0	0	0	0	0	8	63	29

TABLE 5 - Averaged Results

Re_θ	y^+	Δz^+	Sample Size	D^+_{app}	Sample Size	D^+_{core}	ω^+_{core}	Γ^+_{core}	Sample Size	Γ^+_{outer}	Sample Size
1020	2.9	56.8	2	18.3	5	N/A	N/A	N/A	-	125.0	3
	5.7	53.0	7	15.3	6	N/A	N/A	N/A	-	46.9	4
	8.6	35.4	5	17.3	4	N/A	N/A	N/A	-	80.9	4
	11.4	62.3	3	19.0	6	N/A	N/A	N/A	-	113.4	4
	14.3	55.0	9	22.1	15	15.5	0.77	145.9	5	132.2	13
	17.1	48.9	4	20.3	8	20.8	0.43	144.4	8	148.3	7
	20.0	31.4	1	14.9	5	20.8	0.46	155.9	4	-	-
	22.9	91.8	3	27.5	5	N/A	N/A	N/A	-	162.9	2
	28.6	112.5	3	29.1	6	N/A	N/A	N/A	-	175.0	3
	34.3	N/A	-	39.0	7	25.9	0.48	253.7	6	N/A	-
1600	9.4	58.3	4	19.5	5	18.7	0.27	73.8	3	94.9	6
	14.1	57.5	7	32.4	5	22.3	0.29	114.0	4	207.5	4
	18.8	50.0	8	23.8	5	23.1	0.38	158.8	6	179.7	5
	23.5	44.9	5	29.1	10	25.9	0.32	168.3	9	188.3	8
	28.2	55.3	6	20.0	7	20.0	0.43	135.9	8	176.4	5
	32.8	62.4	3	22.7	7	22.5	0.45	179.2	3	223.8	6
2200	6.1	68.5	7	24.4	13	N/A	N/A	N/A	-	119.7	11
	12.4	59.8	6	32.1	10	27.4	0.20	118.7	1	185.9	8
	18.5	01.7	10	41.5	17	35.8	0.22	221.8	3	203.8	13
	24.7	56.0	5	35.7	9	31.2	0.26	195.2	5	199.3	7
	30.9	51.1	3	36.3	7	33.0	0.22	186.9	4	239.2	5
	37.0	67.3	4	44.2	6	N/A	N/A	N/A	-	238.0	5
	43.3	60.0	2	49.2	6	N/A	N/A	N/A	-	248.0	5
	49.4	85.9	2	47.3	3	N/A	N/A	N/A	-	N/A	-

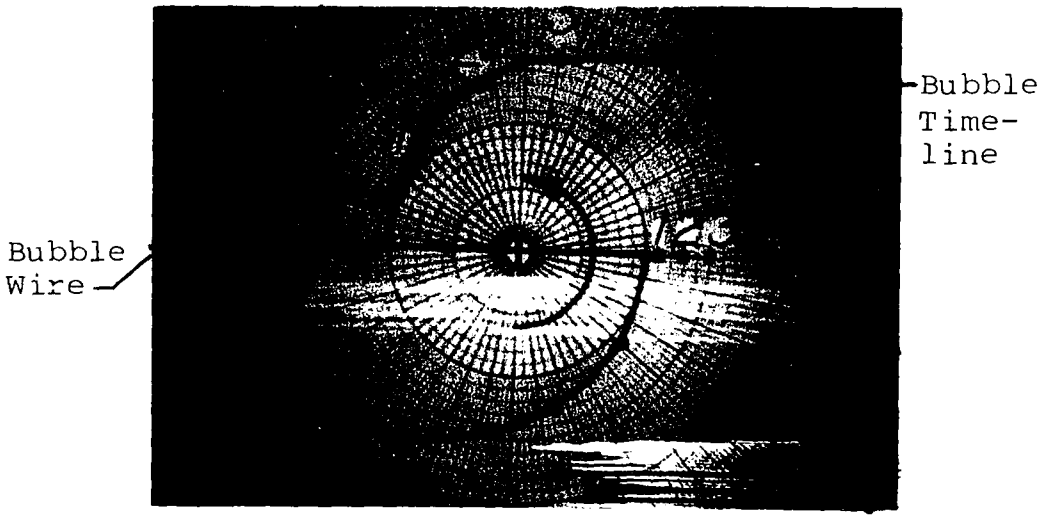

FIGURE 26a- Simulation of the bubble pattern which would result if the wire passed through the center of an axial vortex. The core has rotated 180° in a counterclockwise sense.

FIGURE 26b- Hydrogen bubble pattern resulting when the wire passes through the center of an axial vortex. The wire is located at $y^+=23$. $Re_\theta=1600$.

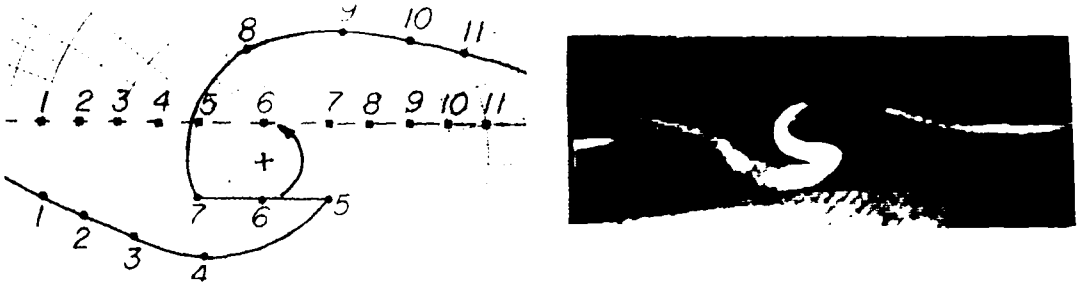

a) Bubble wire located 1/2 radius from vortex center.

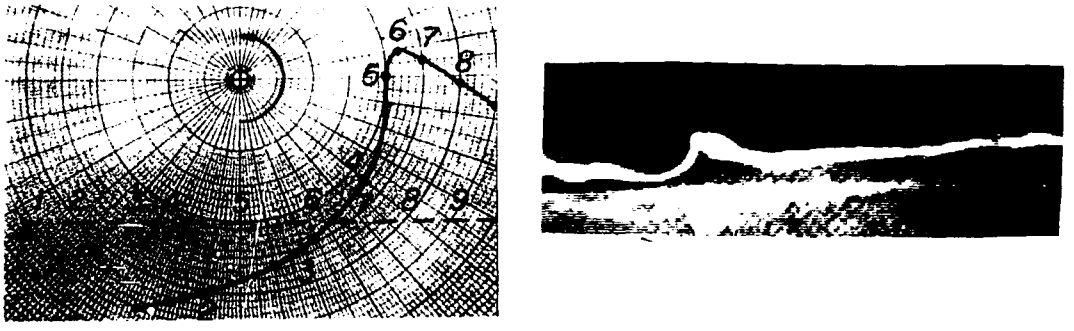

b) Bubble wire located 1 radius from vortex center.

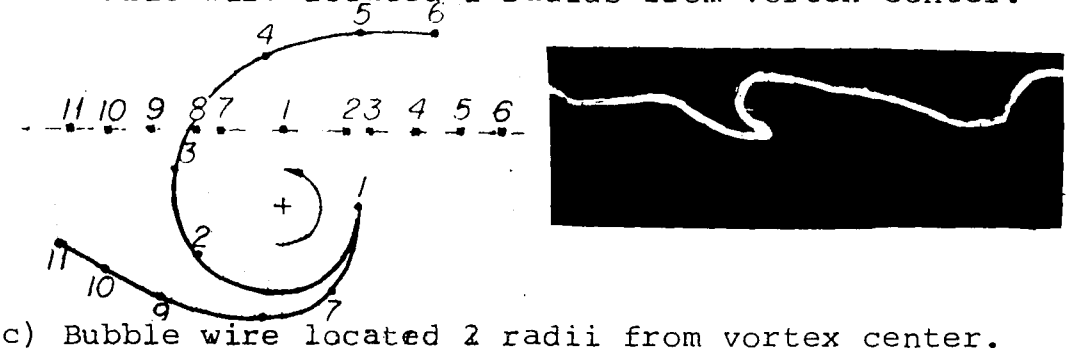

c) Bubble wire located 2 radii from vortex center.

d) Bubble wire located 3 radii from vortex center.

FIGURE 27 - Bubble line pattern simulations and corresponding observed bubble patterns for core rotation of 180°.

a) t=0 sec. (0)

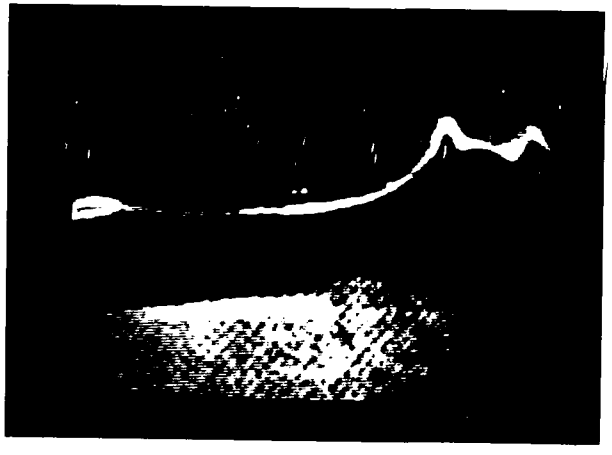

b) t=0.08 sec. (2.8)

c) t=0.17 sec. (5.6)

d) t=0.25 sec. (8.2)

FIGURE 28 - Sequence showing a bubble line pattern which appears as an upwelling. Note that the bubble pattern is similar to Figure 27c where the wire is two radii from the vortex center. Re_θ =1020, wire is at y^+=34. Times in parentheses are $\Delta t U_\tau/\nu$.

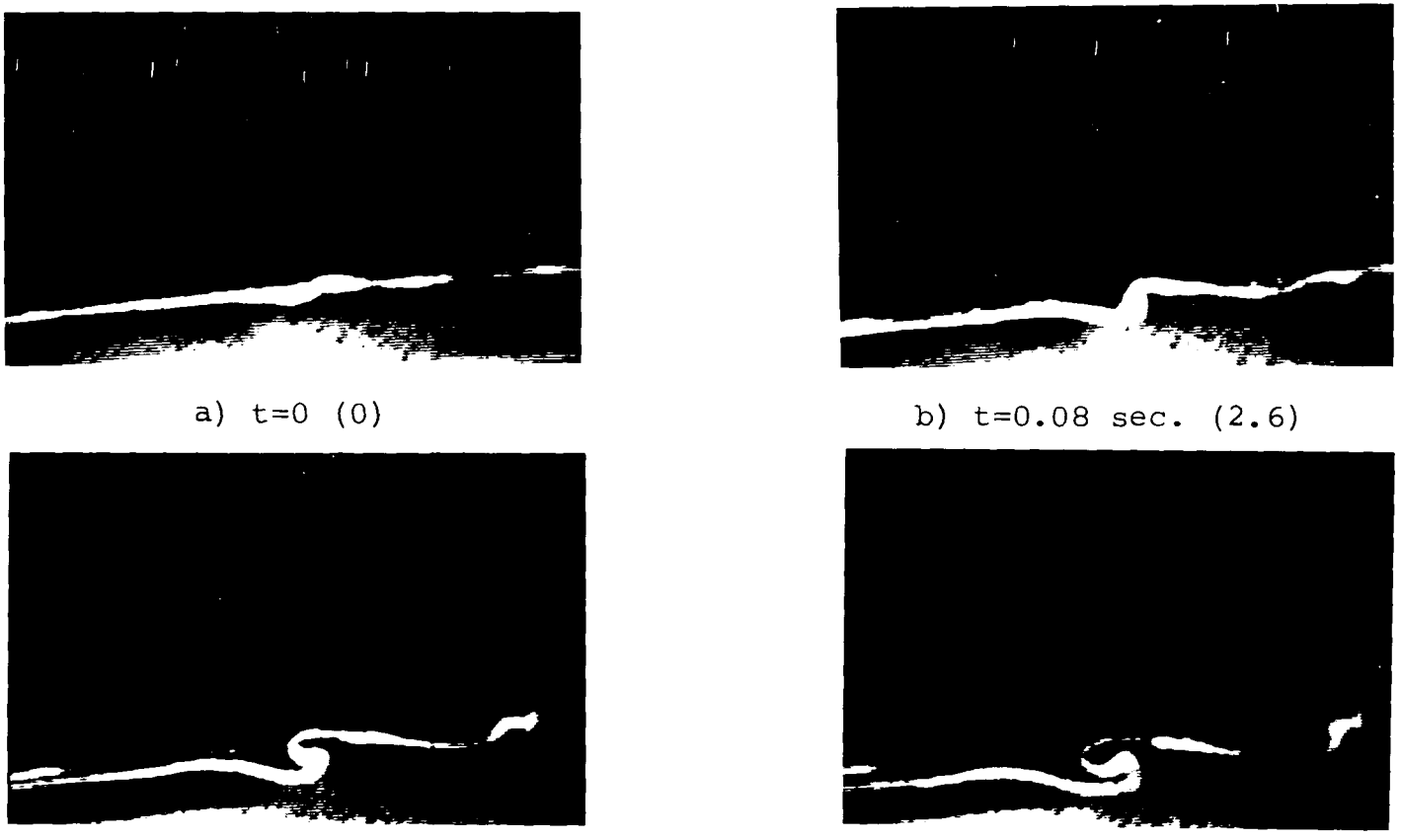

a) t=0 (0)

b) t=0.08 sec. (2.6)

c) t=0.17 sec. (5.6)

d) t=0.25 sec. (8.2)

FIGURE 29 - Sequence showing a bubble line pattern which reveals a rotating axial vortex structure. The bubble wire is beleived to pass through a vortex center as in Figure 26. $Re_\theta = 1020$, wire is at $y^+ = 14$. Numbers in parentheses are $t^+ = \Delta t U_\tau / \nu$.

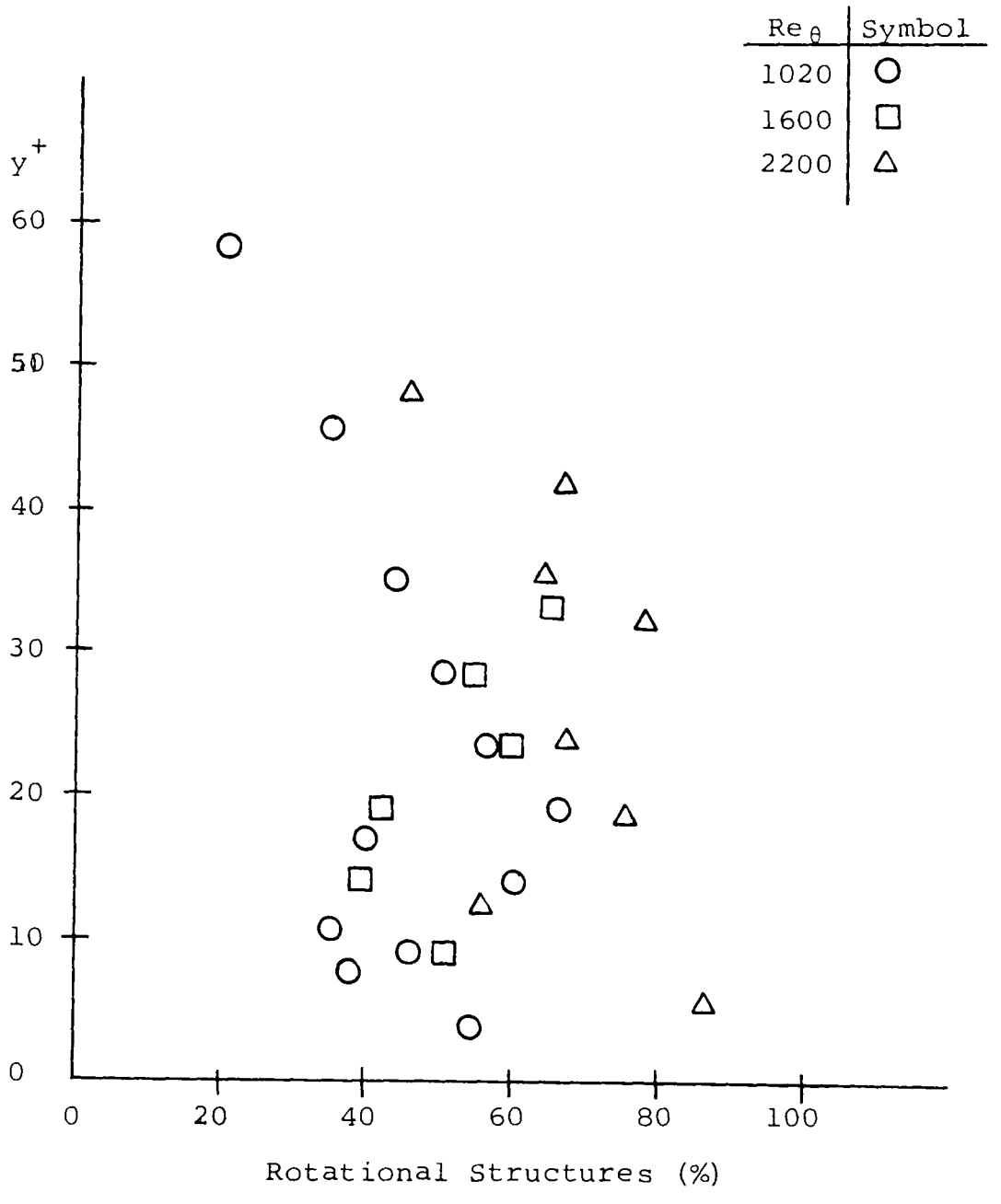

FIGURE 30- Percentage of Observed Rotating Axial Structures vs. y^+ Location of Bubble Wire.

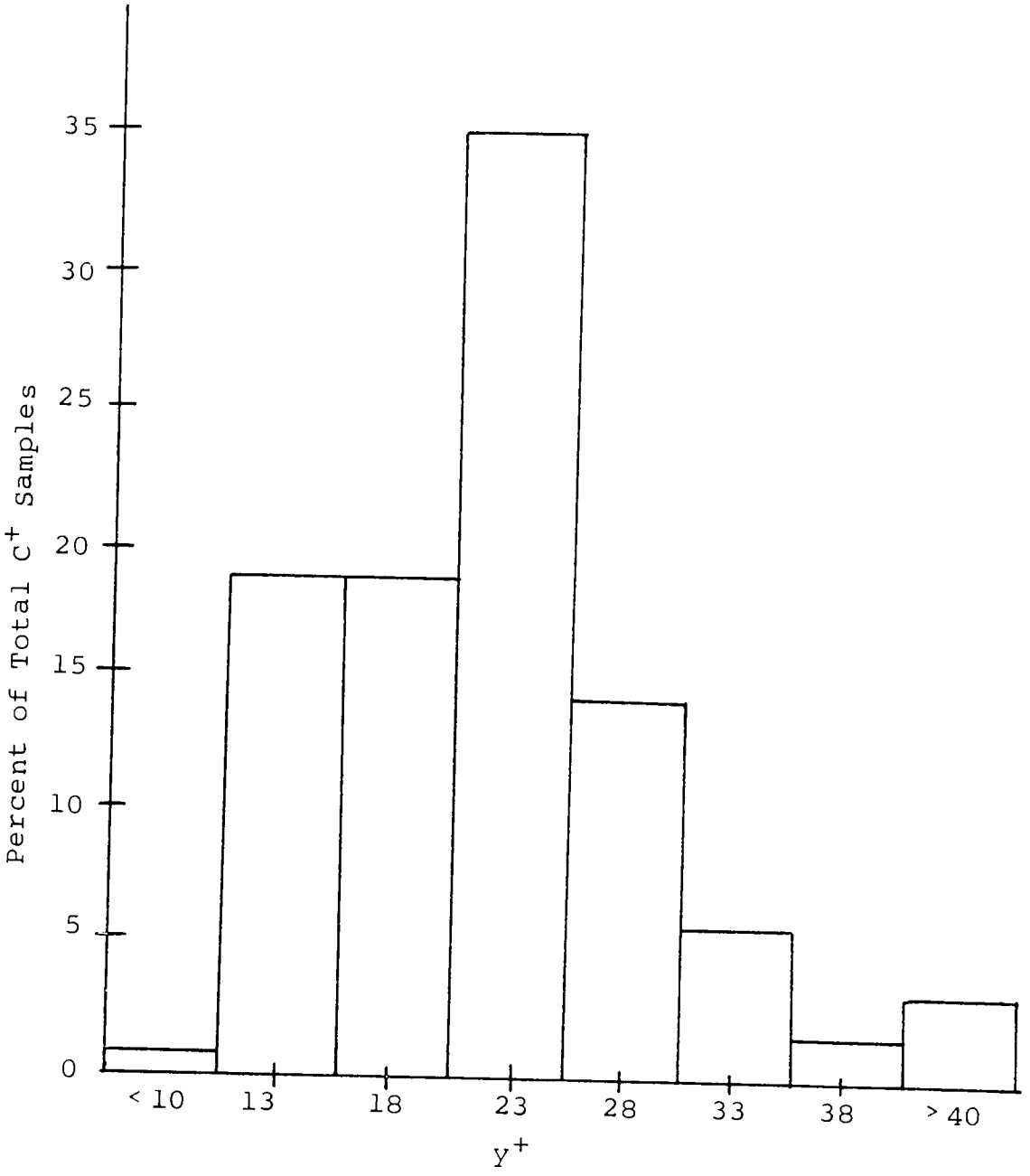

FIGURE 31 - Estimated C^+ for Re_θ =1020.

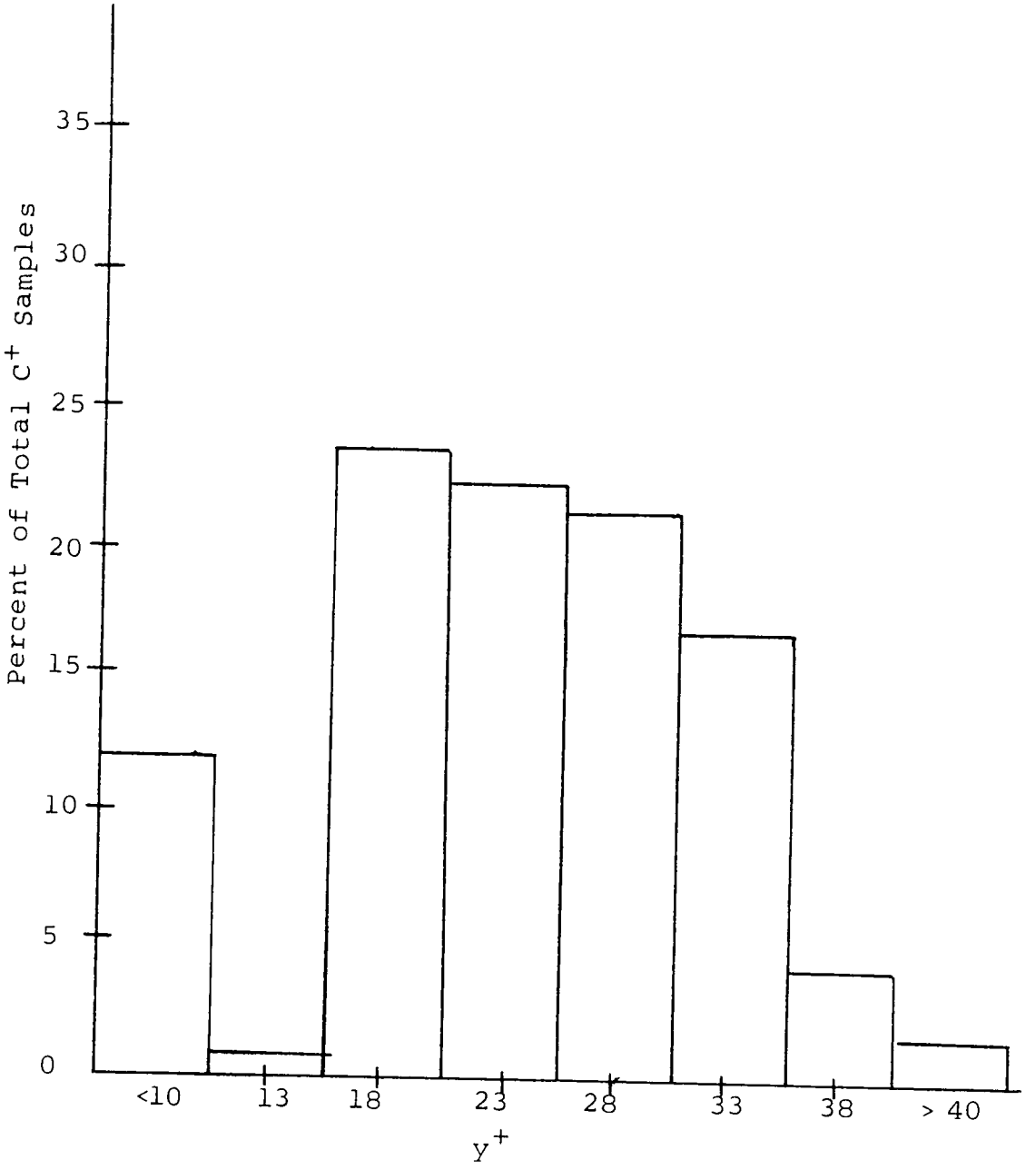

FIGURE 32- Estimated C^+ for Re_θ=1600.

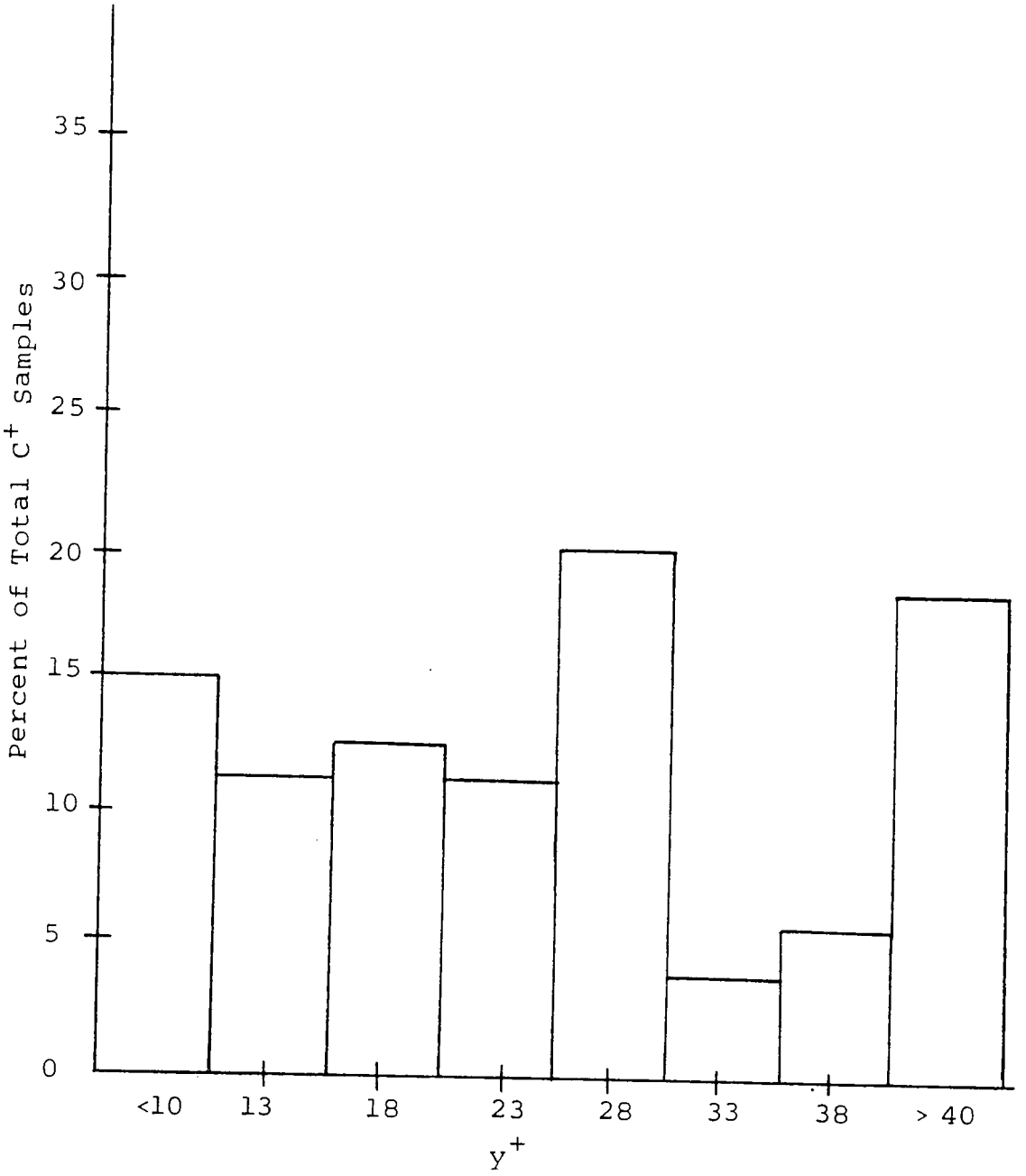

FIGURE 33 - Estimated C^+ for Re_θ=2200.

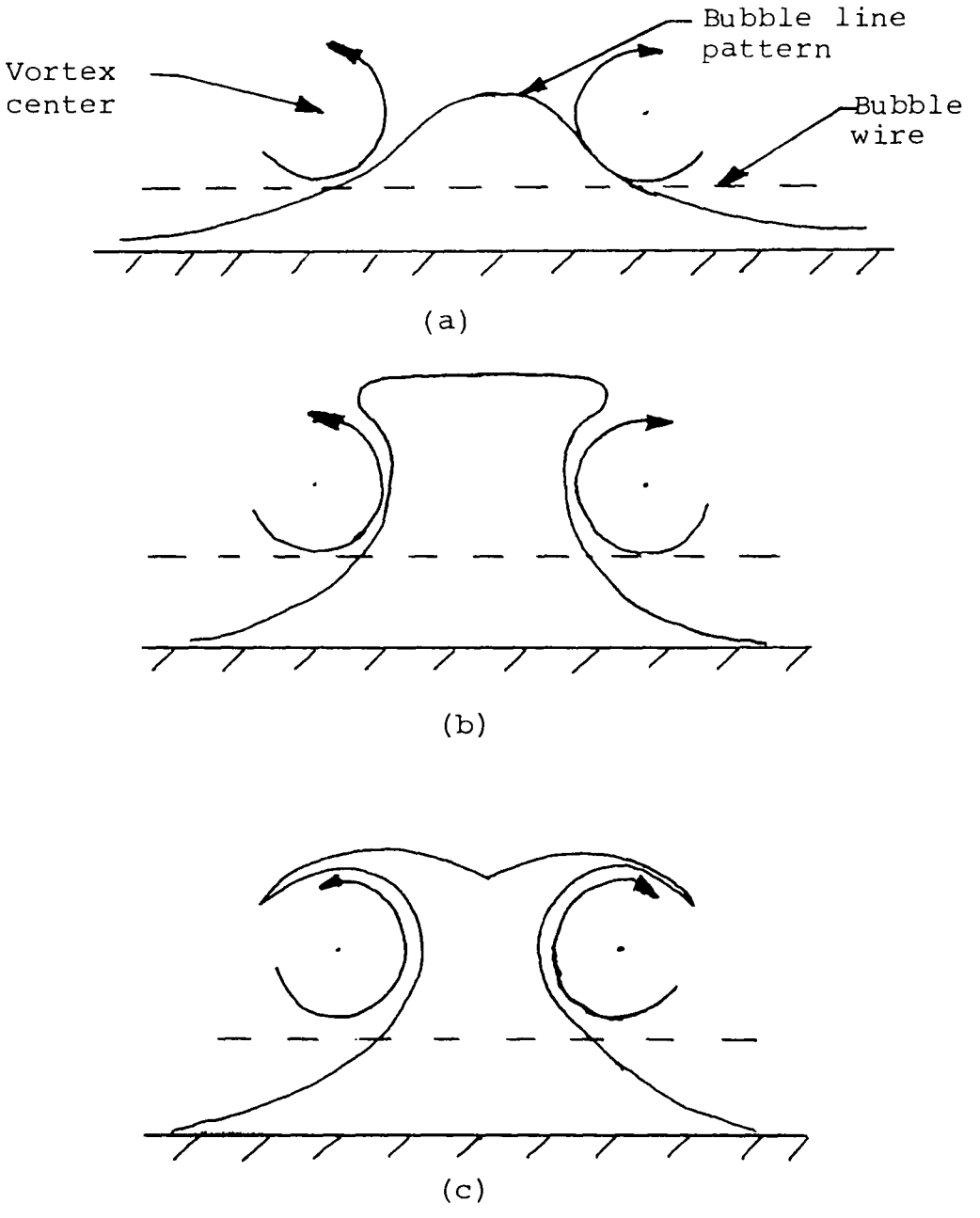

FIGURE 34 - Sketch showing the development of the bubble pattern when under the influence of a pair of counter-rotating vortices.

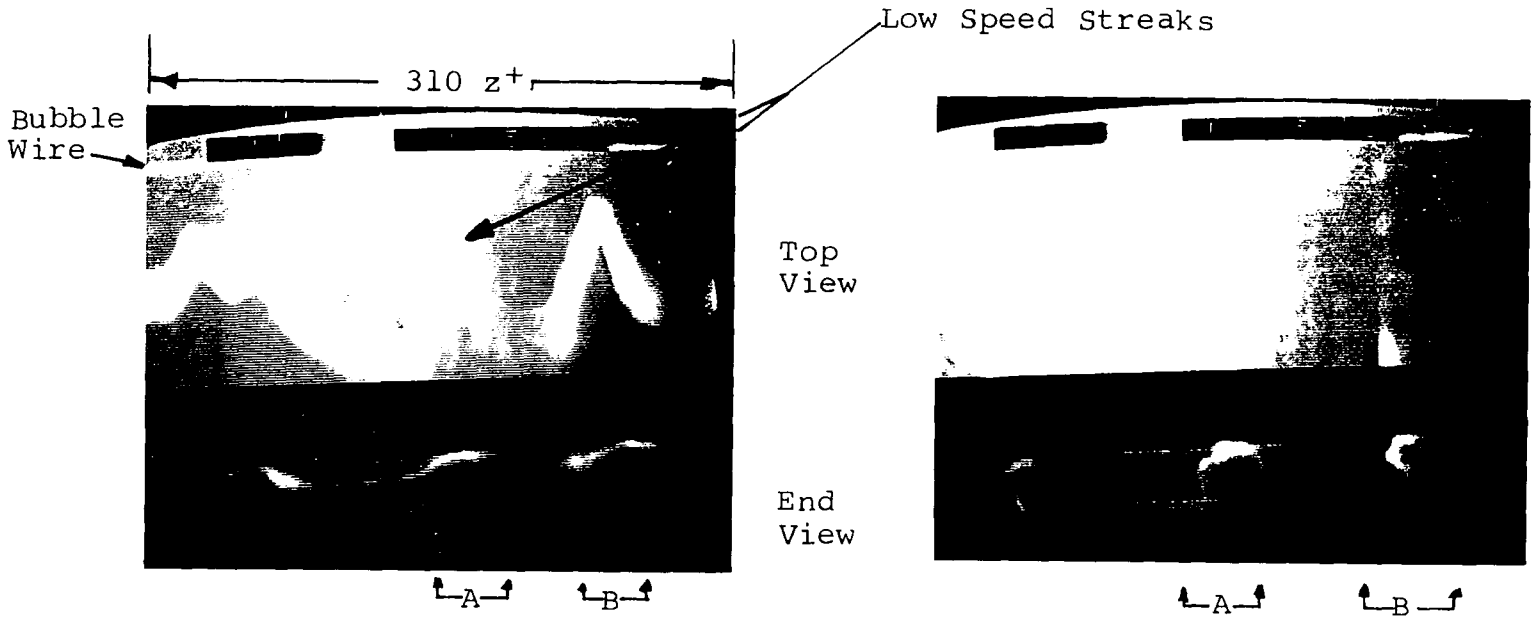

a) t=0 sec (0)

b) t= 0.16 sec (13.9)

FIGURE 35 - Combined top and end view showing the development of two pairs of counter-rotating axial vortices (at "A" and "B"). Note that a low speed streak in the top view corresponds to each pair of counter-rotating vortices. Flow is top to bottom in the top view and out of the page in the end view. Re_θ =1600, wire is at y^+= 14.

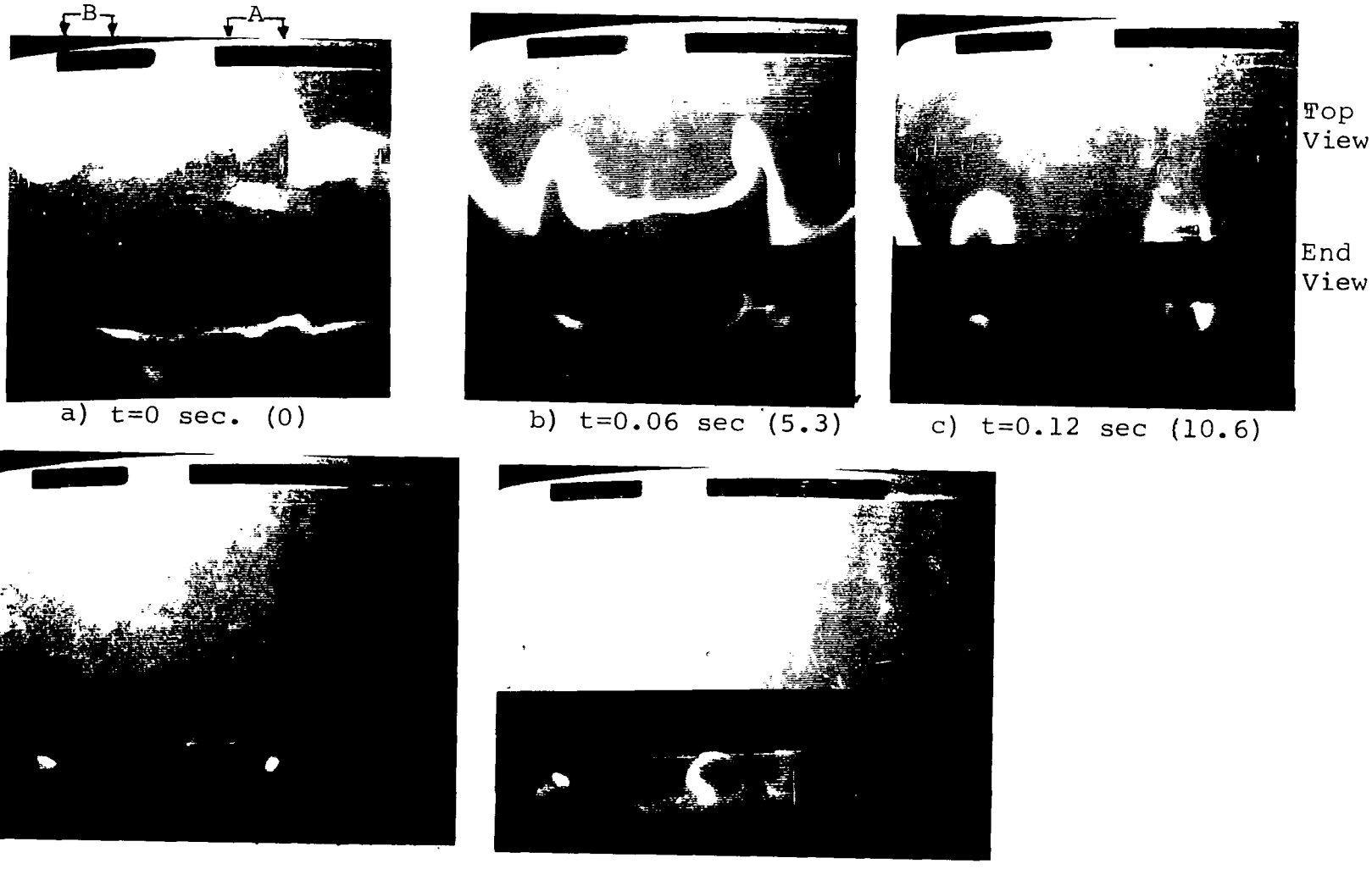

FIGURE 36 - Combined top and end views showing the development of two pairs of counter-rotating axial vortices. Flow is top to bottom in top view and out of the page in the end view. Re_θ =1600, wire is at y^+=14.

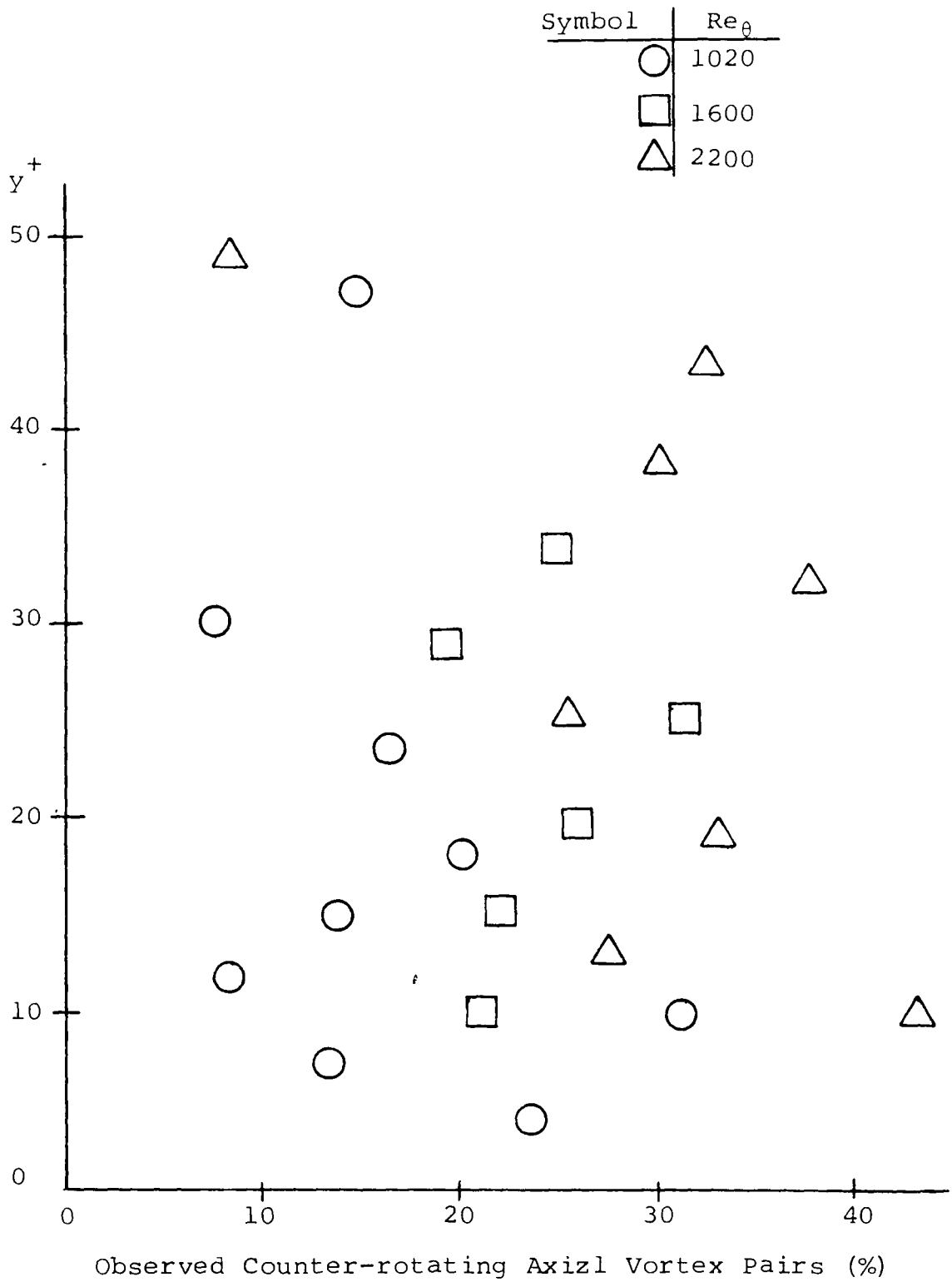

FIGURE 37 - Observed Counter-rotating Axial Vortex Pairs vs. Distance of Bubble Wire from the Surface.

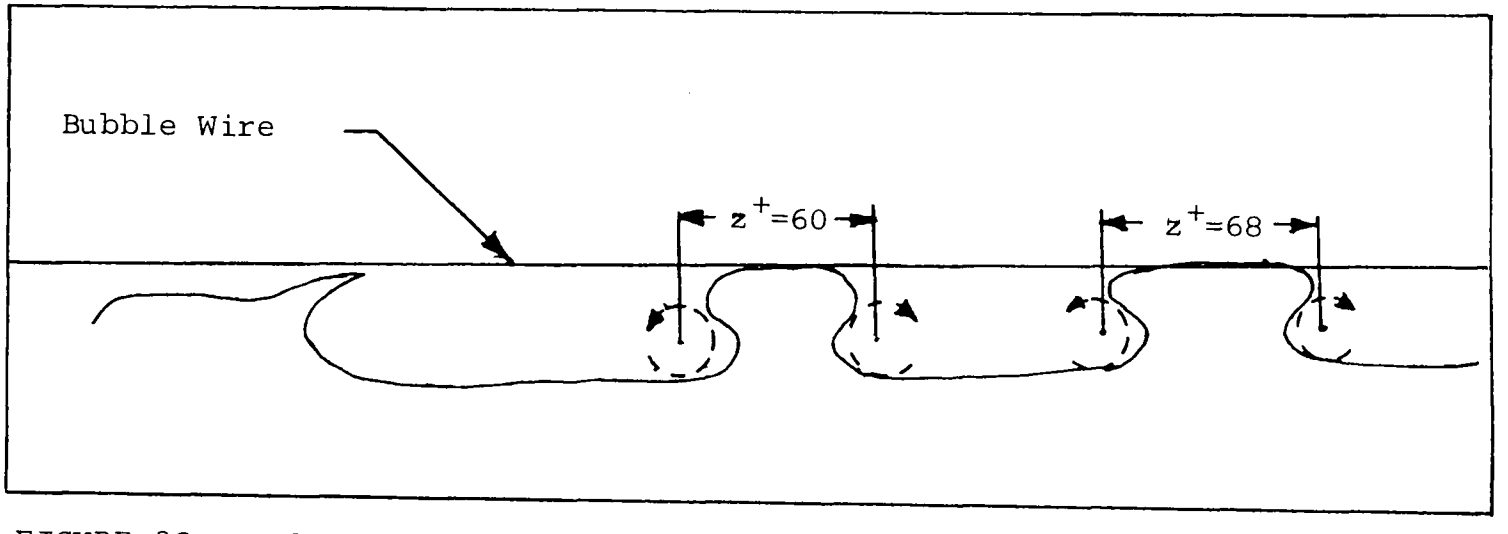

FIGURE 38 - Bubble line pattern sketched from the video screen showing the manner in which the spacing, z^+, between a pair of counter-rotating axial vortices is determined. Dotted lines show relative location and size of vortices. $Re_\theta = 1600$, wire is at $y^+ = 14$.

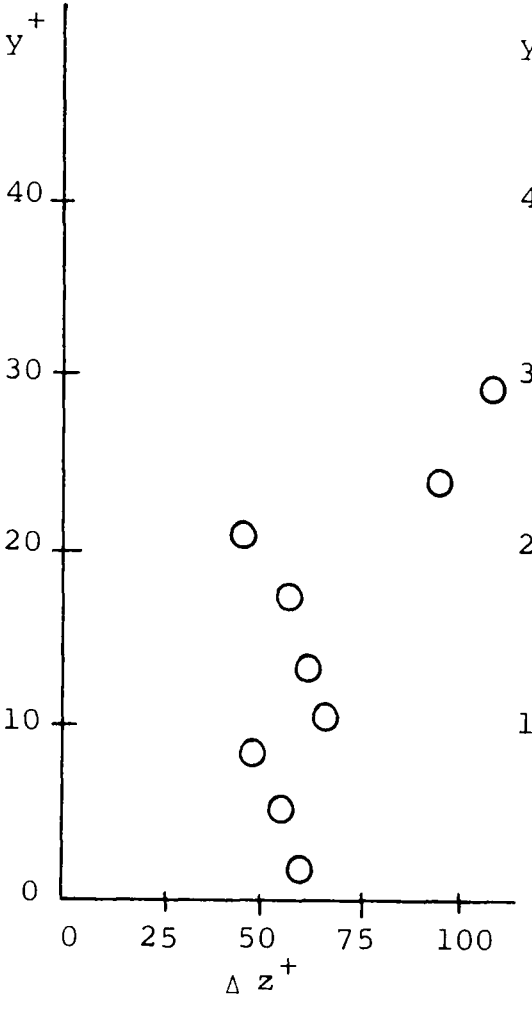

FIGURE 39 - Average Axial Vortex Spacing vs. y^+ Location of Bubble Wire. Re_θ= 1020.

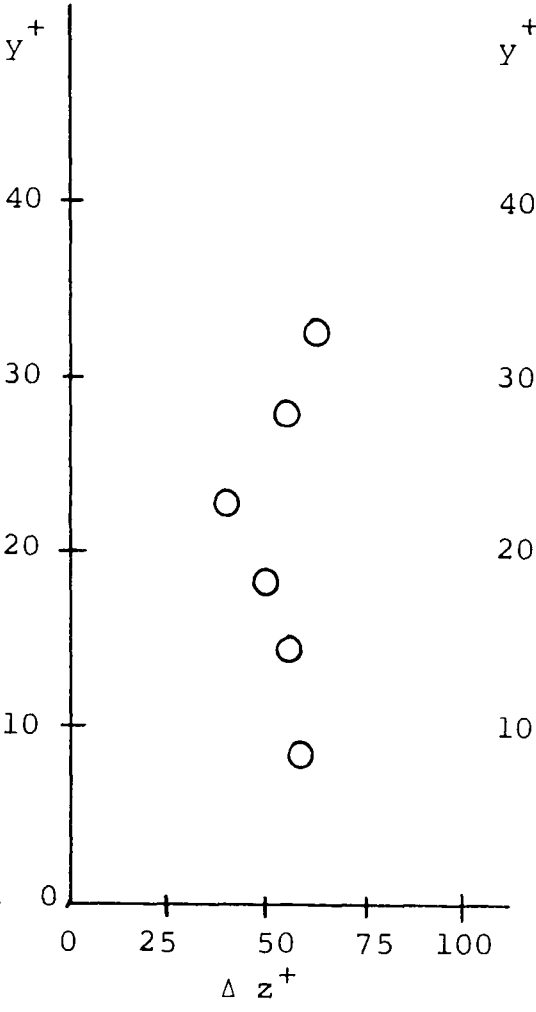

FIGURE 40-Average Axial Vortex Spacing vs. y^+ Location of Bubble Wire. Re_θ = 1600.

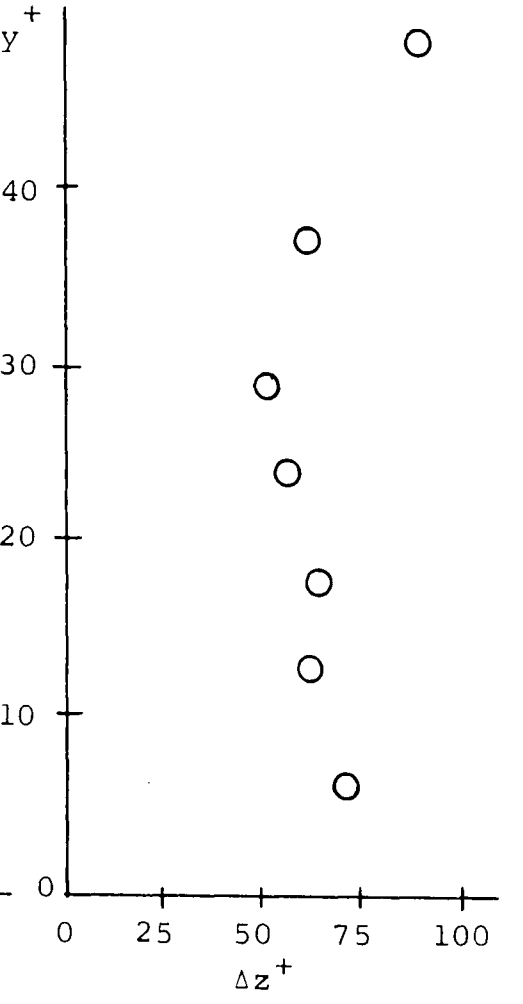

FIGURE 41-Average Axial Vortex Spacing vs. y^+ Location of Bubble Wire. Re_θ= 2200.

FIGURE 42- End view of bubble pattern obtained using the three wire hydrogen bubble probe showing the effects of an axial vortex. Re_θ=1020 and wires are $28y^+$ apart with the lowest being at y^+=6.

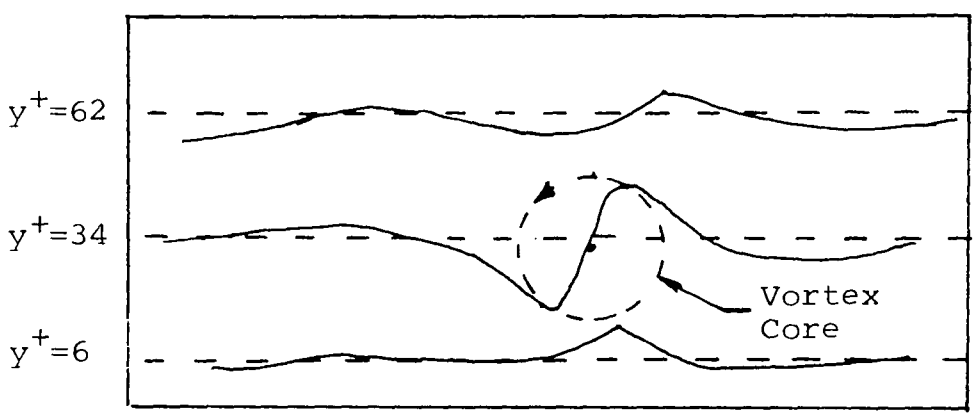

Sketch showing the relative size and location of the vortex core in the above figure. Note the similarity between the bubble pattern on the bottom wire and that of Figure 26d.

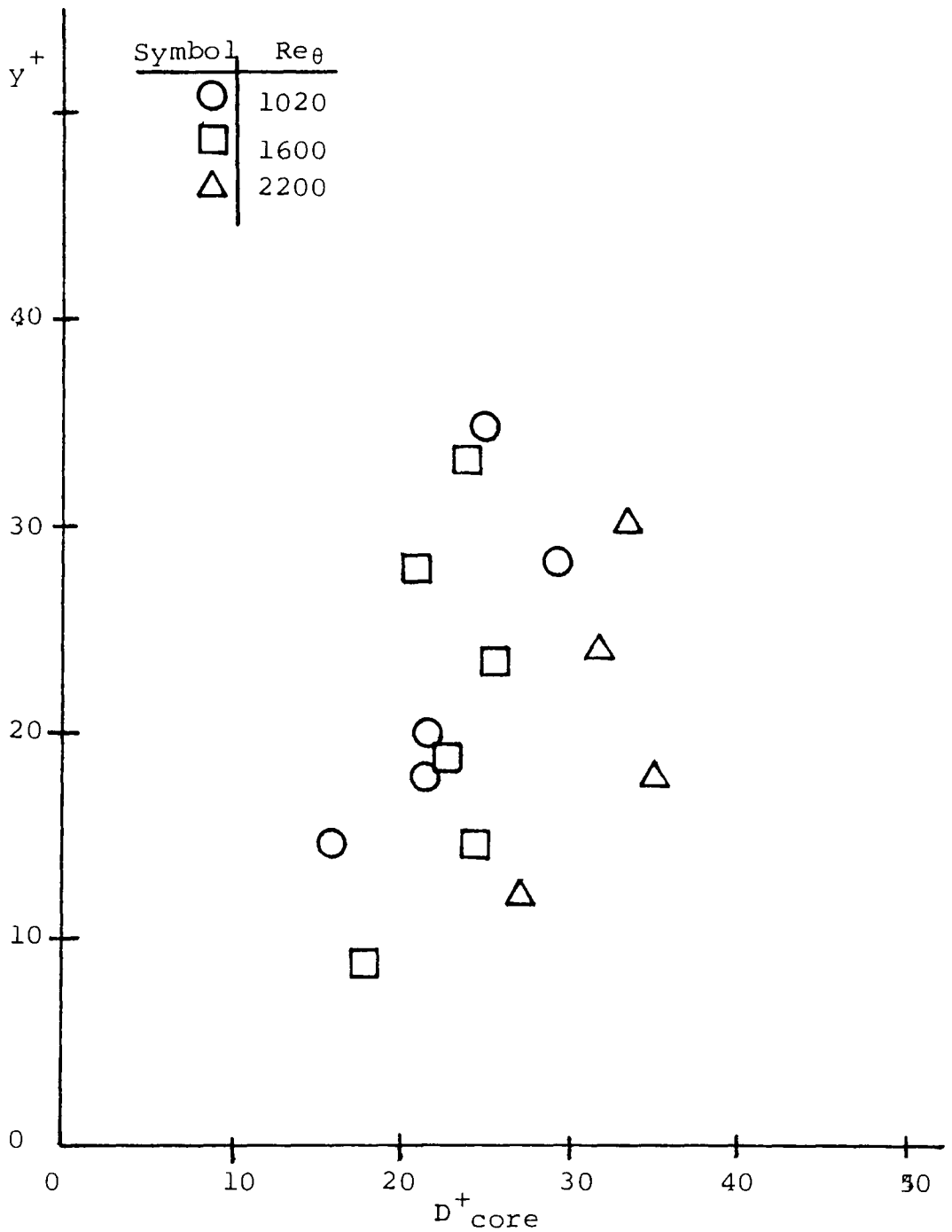

FIGURE 43- Axial Vortex Core Size vs. Distance from the Surface

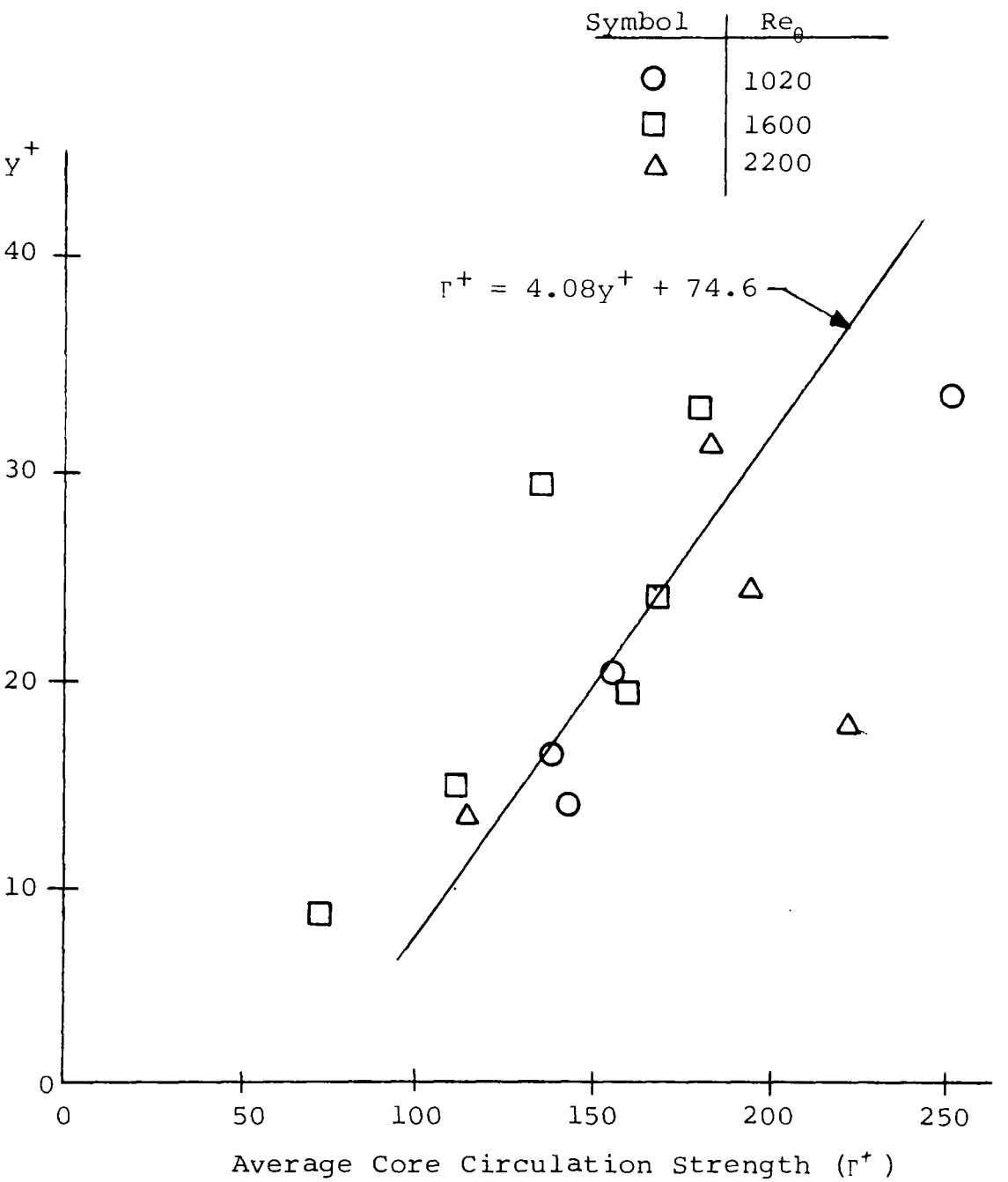

FIGURE 44- Bubble wire location versus Circulation strength determined by measurement of the vortex core.

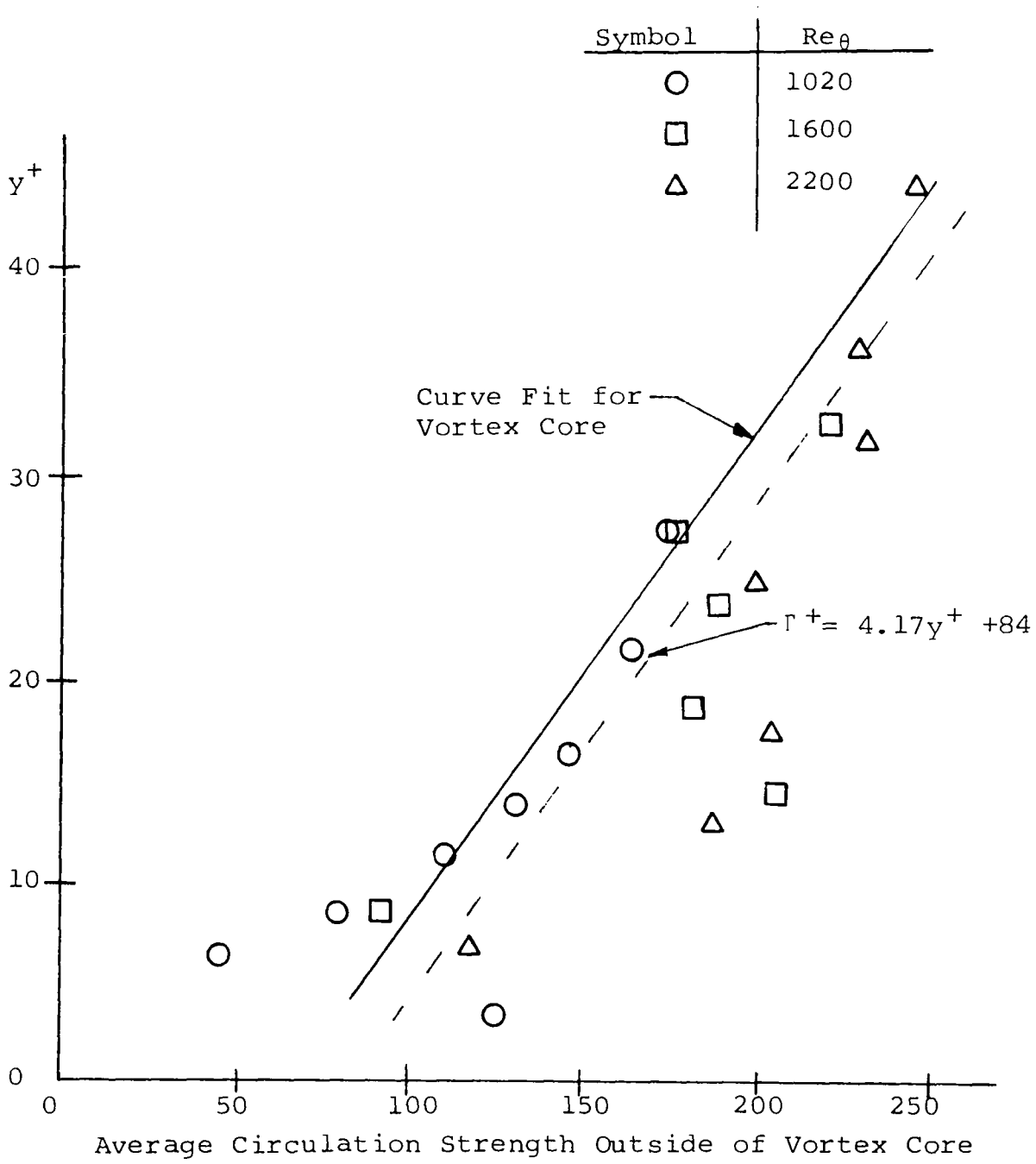

FIGURE 45- Bubble wire location versus Average circulation strength as determined from measurements outside of the vortex core.

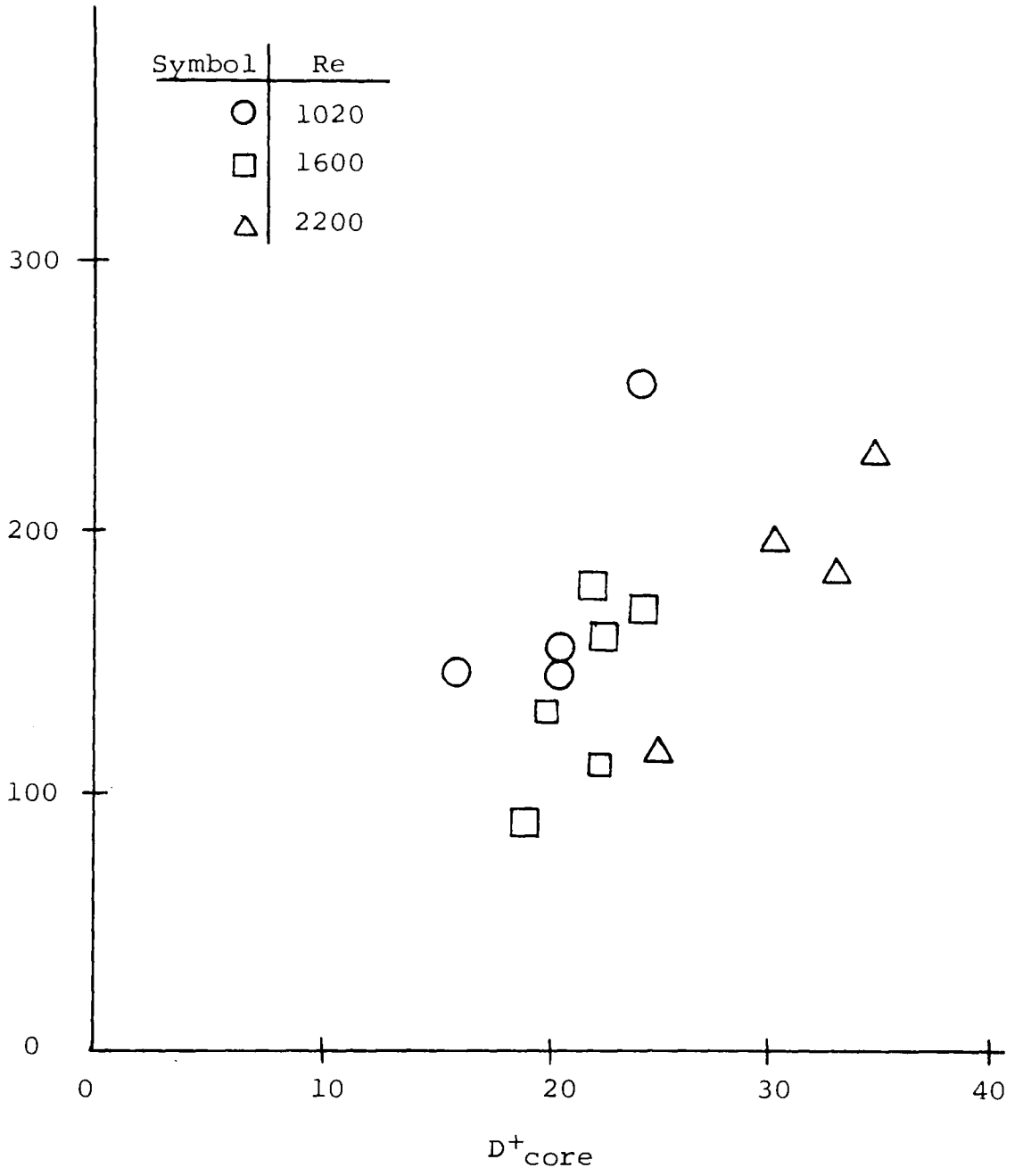

FIGURE 46- Axial Vortex Core Size vs. Vortex Core Strength

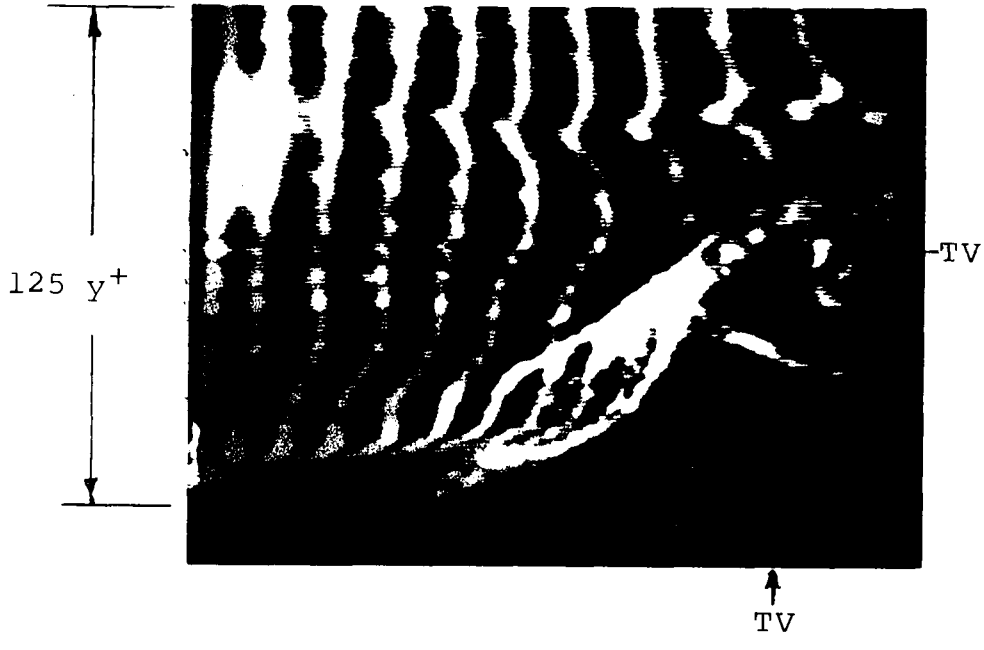

FIGURE 47- Side view of a transverse vortex. Vortex is located at the intersection of "TV-TV" and is approximately at $y^+=60$. $Re_\theta=2200$.

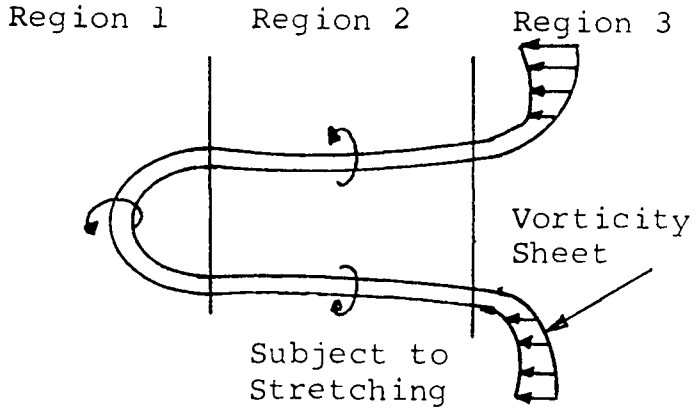

a) Top View

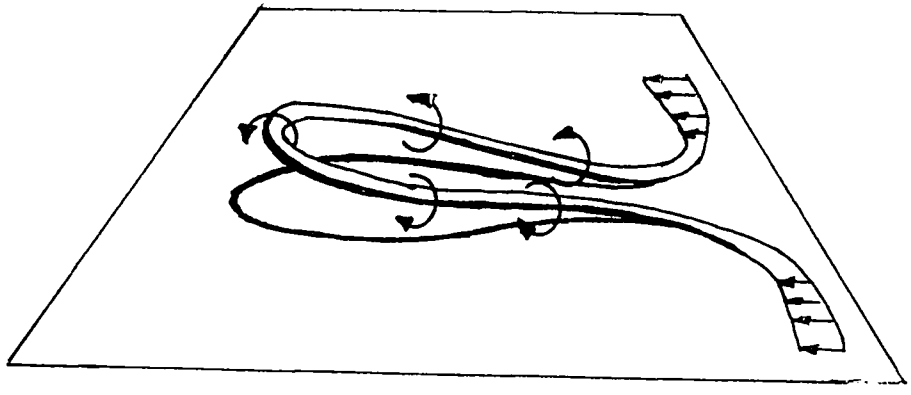

d) Perspective View

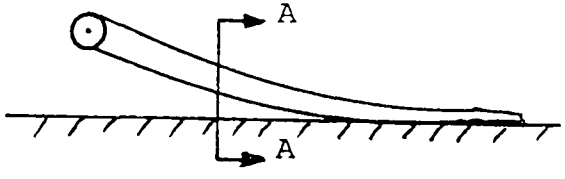

b) Side View

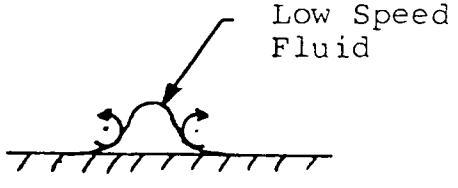

c) View A-A

FIGURE 48 - Hypothisized Loop Vortex Model

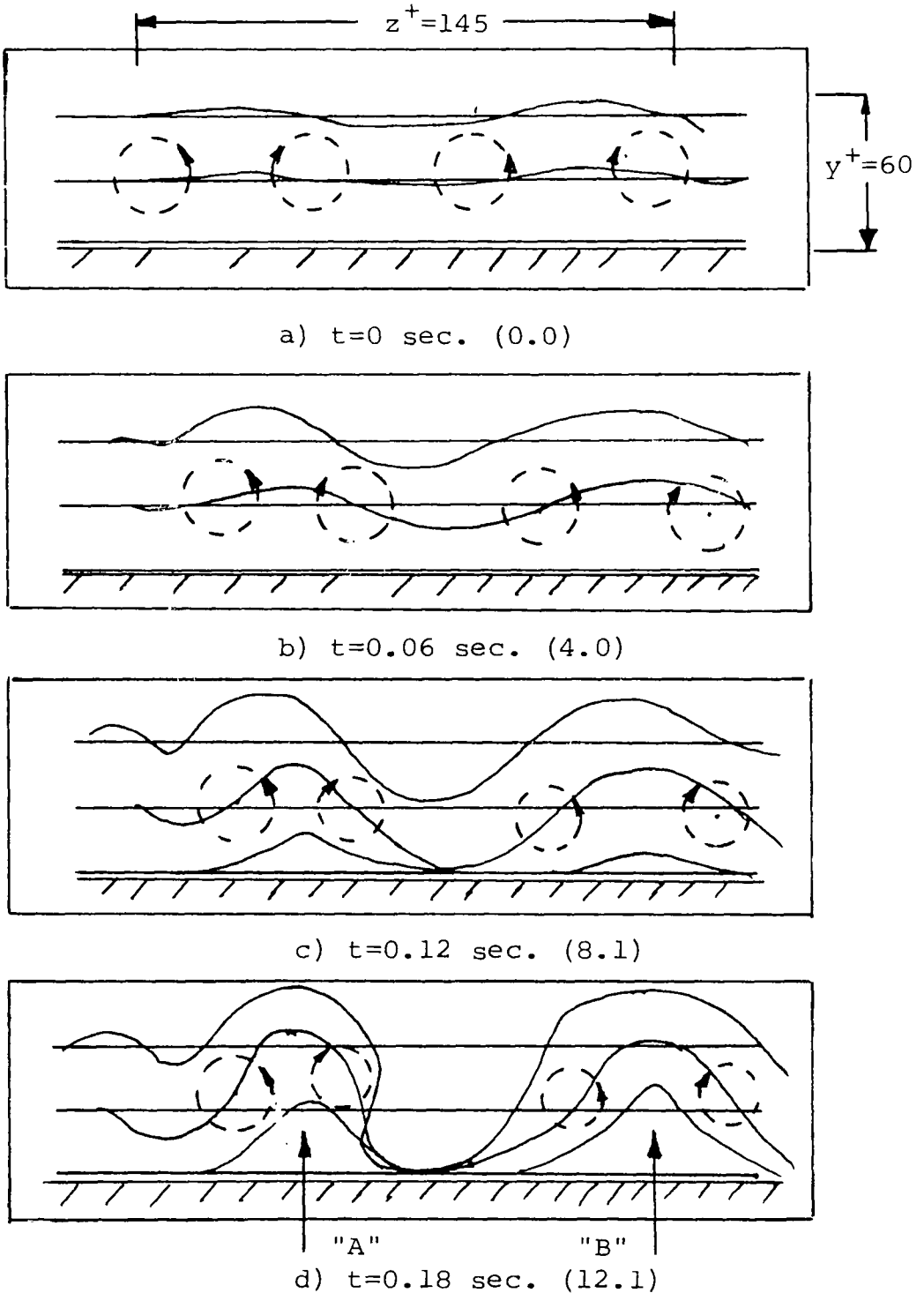

FIGURE 49- Sequence showing the "pick-up" of low speed fluid from the surface. Re_θ=1600. The bottom wire is at y^+=2, with the others being $28y^+$ apart. Dotted line shows relative location of axial vortices. (Tracing from video screen)

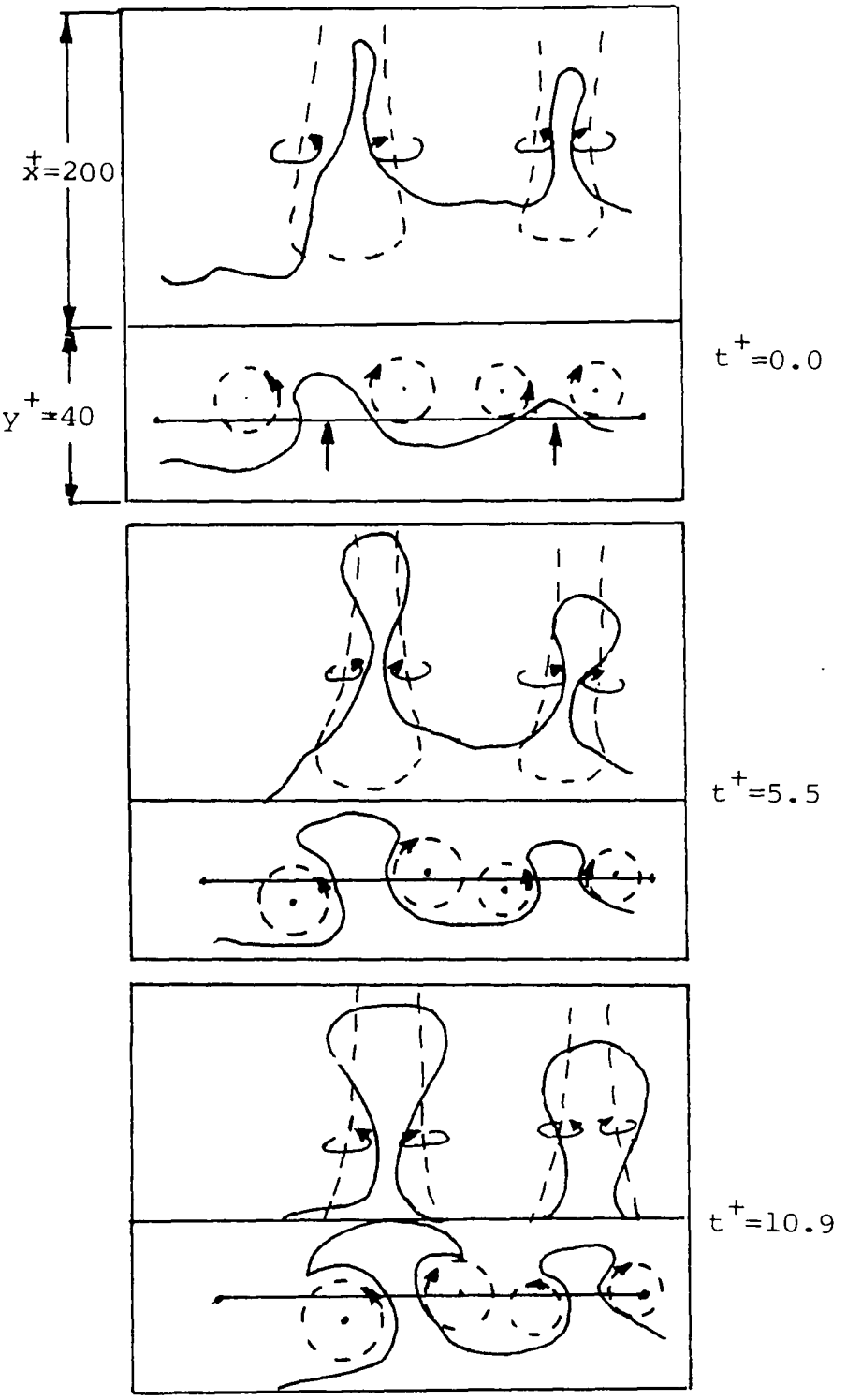

FIGURE 50- Combined top and end view of counter-rotating axial vortices in a moving reference frame ($U_{ref}=0.2U_\infty$). $Re_\theta=1600$ and bubble wire is at $y^+=14$. Dotted lines show relative location of vortices. (Tracing of bubble pattern from video screen).

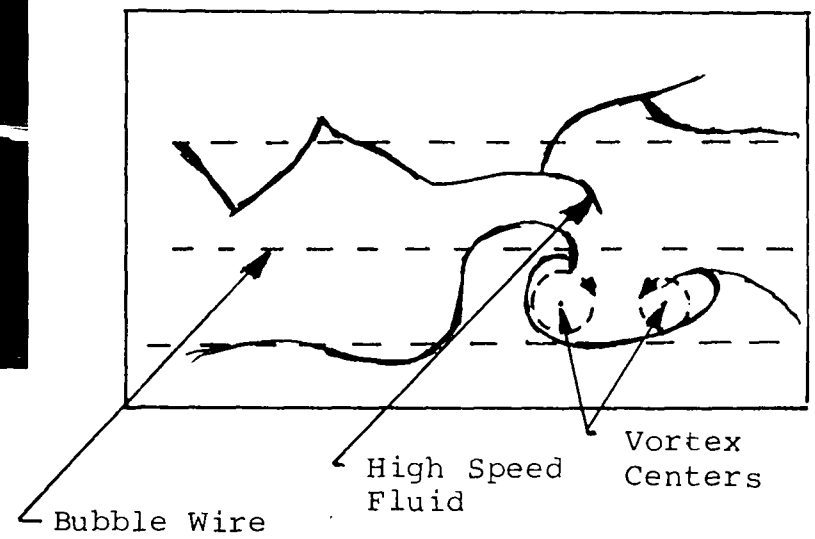

FIGURE 51- High speed fluid moving toward the surface between two adjacent axial vortices of adjacent loop vortices. Wire is at $y^+=2$, $Re_\theta=1020$.

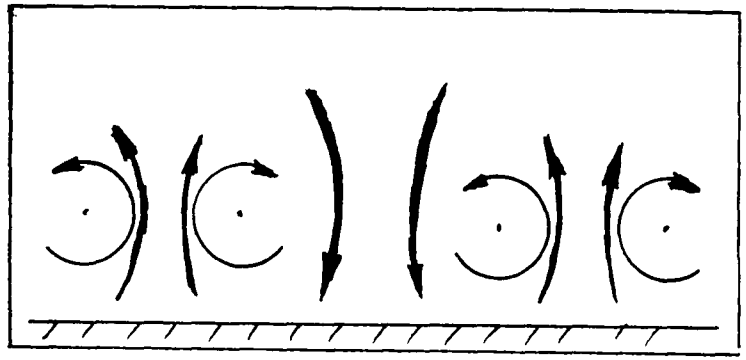

Idealized representation of two adjacent counter-rotating axial vortex pairs picking low speed fluid up from the surface and bringing high speed fluid to the surface.

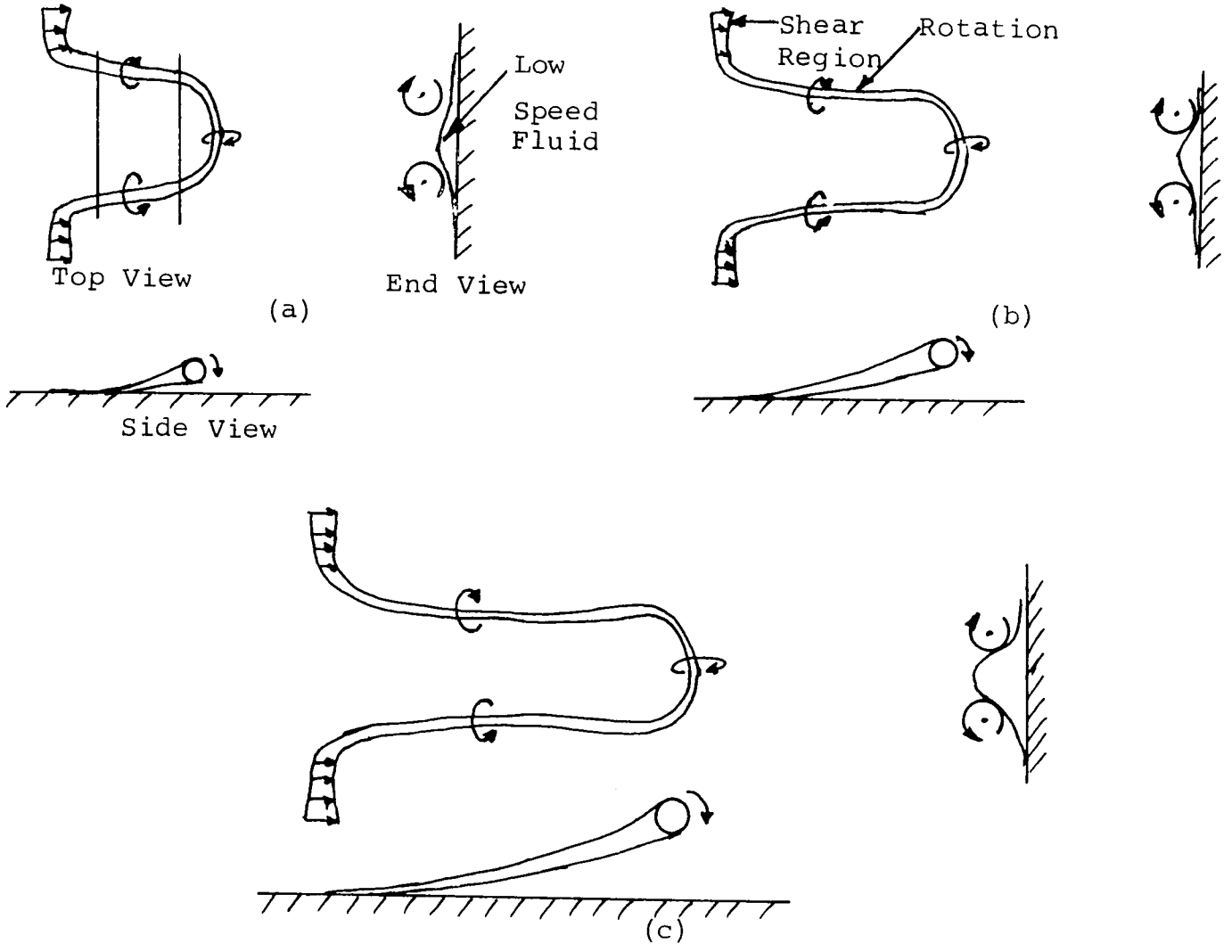

FIGURE 52 - Evolution of a Loop Vortex

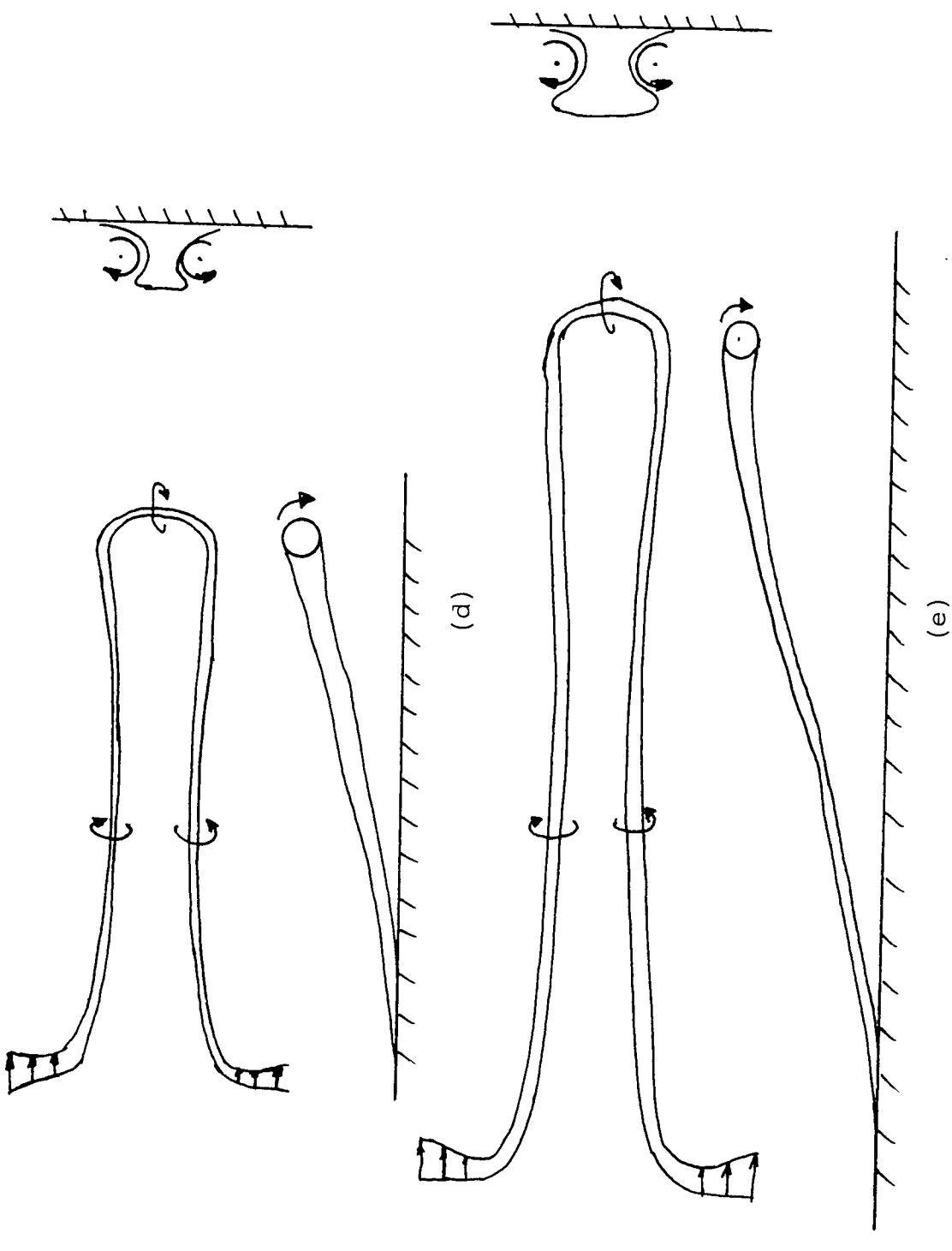

FIGURE 52- continued

SECTION 6

SUMMARY AND CONCLUSIONS

6.A Introduction

This section summarizes the most predominant observations of the present study and draws conclusions regarding the characteristics of axial vortex structures in turbulent boundary layers. A brief description of a hypothesized loop vortex model, which is consistent with the present findings, is also given.

6.B. Statistical Characteristics

1. 40% or more of the observed bubble line patterns appeared as rotating structures for $y^+ < 60$, while the remainder appeared as upwellings or downward motions. It is speculated that these upwellings and downward motions are merely the appearance taken on by the bubble patterns when the bubble wire is farther from the vortex core.
2. Between 9% and 40% of the observations appeared as pairs of counter-rotating axial vortices, with this percentage increasing as Re_θ increased for constant y^+. This increase is

speculated to be due to the greater depth of field and shorter time-scales at higher Re_θ.

6.C Physical Characteristics

1. The location of the vortex centers were determined to vary from $11 < y^+ < 37$ with the highest frequency of observed centers being for $22 < y^+ < 26$. An indirect method of determining center locations yielded results consistent to those of direct visualization.
2. The spacing, ΔZ^+, between pairs of counter-rotating axial vortices was observed to vary over a range of $35 < \Delta Z^+ < 110$ with the minimum spacing generally occurring in the region where most vortex centers were observed, $22 < y^+ < 26$.
3. Vortex core sizes, D^+, were observed to vary between $15 < D^+_{core} < 36$, with D^+ being a monotonically increasing function of y^+.

6.D Rotational Characteristics

1. Mean vorticity in the observed vortex core was determined to vary over an approximate range of $0.2 < \omega_x^+ < 0.5$.
2. The circulation strength, Γ^+, in the vortex coil was determined to vary from $73 < \Gamma^+_{core} < 254$. Γ^+_{core} appears to increase with both y^+

and D^+, which is speculated to be due to a process of vortex coelesence.

3. Comparison of linear curve fits of Γ^+ vs. y^+ obtained both within vortex cores and outside the core region indicate that the bulk of the vorticity in axial vortices is concentrated in the core.

4. The valued circulation strength for transverse vortices observed in the region $40 < y^+ < 100$, appears consistent with the corresponding strength of the axial vortices.

6.F Hypothetical Model and Supporting Observations

1. Since the circulation strength of the transverse vortex appears consistent with that of the axial vortices, a stretched and lifted loop vortex model was hypothesized which is consistent with these observed characteristics. The model consists of a leading transverse vortex coupling a pair of counter-rotating axial vortices which each end in a vorticity sheet at the surface.

2. Using a three-wire bubble probe, it was observed that low speed fluid from the region near the wall is lifted and brought up between a pair of counter-rotating axial vortices.

3. Higher speed fluid farther from the wall is observed to be induced toward the surface by the action axial vortices from adjacent loop vortices.

4. It is hypothesized that the higher speed fluid induced toward the surface is strongly decelerated by viscous action and spreads laterally by the action of the axial vortices. This decelerated fluid is then concentrated between the legs of the counter-rotating vortex pairs, reinforcing and/or forming the low speed streaks. After being concentrated, the now low speed fluid is lifted between adjacent pairs of counter-rotating axial vortices and results in a shear interface with the higher speed, outer region fluid, initiating new loop vortices which perpetuate the inflow-deceleration-streak formation process.

REFERENCES

1. Bakewell, H.P. and Lumley, J.L., "Viscous Sublayer and Adjacent Wall Region in Turbulent Pipe Flows", Phys. of Fluids, Vol. 10 (1967), p. 1880

2. Bark, F.H., "On the Wave Structure of the Wall Region of a Turbulent Boundary Layer", J.F.M., Vol. 70 (1975), p. 229

3. Blackwelder, R.F. and Eckelmann, H. "Streamwise Vortices Associated with the Bursting Phenomenon", Journal of Fluid Mechanics, Vol. 94, Pt. 3 (1979), pp. 577-594

4. Blackwelder, R.F. "The Bursting Process in Turbulent Boundary Layers", Proc. Workshop on Coherent Structure of Turb. Boundary Layers, C.R. Smith and D.E. Abbott, eds., 1978, pp. 211-222

5. Blackwelder, R.F. and Eckelmann, H., "Spanwise Structure of the Bursting Phenomenon", Berlin Symposium on Turbulence, 1977

6. Bradshaw, P., (ed.) Topics in Applied Physics - Turbulence, Vol. 12, Springer-Verlag, N.Y. 1978

7. Bradshaw, P., An Introduction to Turbulence and Its Measurement, Pergamon Press, Oxford, 1971

8. Brodkey, R.S., "Flow Visualization and Simultaneous Anenometry Studies of Turbulent Shear Flows", Proc. Workshop on Coherent Structure of Turbulent Boundary Layers, C.R. Smith and D.E. Abbott, eds., Lehigh University, 1978

9. Brown, G.L. and Thomas, A.S.W., "Large Structures in a Turbulent Boundary Layer", Phys. of Fluids, Vol. 20, No. 10, Pt. II (October 1977)

10. Coles, Donald, "A Model for Flow in the Viscous Sublayer", Proc. Workshop on Coherent Structure of Turb. Boundary Layers, C.R. Smith and D.E. Abbott, eds., 1978

11. Coles, D. and Barker, S.J., "Some Remarks on a Synthetic Boundary Layer" in Turbulent Mixing in Non-Reactive and Reactive Flows, S.N.B. Monthly, ed., Plenum Press, 1975

12. Corino, E.R. and Brodkey, R., "A Visual Investigation of the Wall Region in Turbulent Flow", Journal of Fluid Mech., Vol. 37, Pt. 7 (1969)

13. Cornelius, K., Takeuchi, K., and Deutsch, S., "Turbulent Flow Visualization: A Technique for Extracting Accurate Quantitative Information", 1976

14. Cornelius, K. and Takeuchi, K., "Description of Proposed Flow Visualization Study", Interdepartmental Communication, Lockheed Georgia Co., March 31, 1977

15. Corrsin, S., "Some Problems in Turbulent Shear Flows", Naval Hydrodynamics Bulletin #515

16. Doligalski, T.L., Smith, C.R., and Walker, J.D.A., "Production Mechanism for Turbulent Boundary Layer Flows", Prog. in Aeronautics and Aerospace Science, in press

17. Eckelmann, H., Nychas, S., Brokey, R., and Wallace, J., "Vorticity and Turbulence Production in Paltein Recognized Turbulent Flow Structures", Phys. of Fluids, Vol. 20, #10 (1977), pp. 225-231

18. Falco, R.E., "Some Comments on Turbulent Boundary Layer Structure Inferred from the Movements of a Passive Contaminant", AIAA 12th Aerospace Science Meeting, February 1974, AIAA Paper #74-99

19. Falco, R.E., "Coherent Motions in the Outer Region of Turbulent Boundary Layers", Phys. of Fluids, Vol. 20, #10 (1977)

20. Falco, R.E., "A Personal and Provocative Review of the Current State of Knowledge of Turbulent Boundary Layer Structure", Stanford Workshop, 1978

21. Falco, R.E., "Structural Aspects of Turbulence in Boundary Layer Flows", Proceedings of 6th Biennial Symposium on Turbulence, Rolla, Missouri, October 1979

22. Ferrell, J.K., Richardson, F.M., and Beatty, K.O. Jr., "Dye Displacement Technique for Velocity Distribution Measurements", Industrial and Engineering Chemistry, Vol. 47 (1955), p. 29

23. Grass, A.J., "Structural Features of Turbulent Flow Over Smooth and Rough Boundaries", Journal of Fluid Mechanics, Vol. 50, Pt. 2 (1971)

24. Hama, F.R. and Nutant, J., "Detailed Flow Field Observations in the Transition Process in a Thick Boundary Layer", Instit. of Fluid Dynamics, University of Maryland, 1963

25. Hatziavramidis, D.T. and Hanratty, T.J., "Interpretation of the Turbulent Flow in the Viscous Wall Region as a Driven Flow", Report for Office of Naval Research, NR 062-858, January 1978

26. Head, M.R. and Bandyopadhyay, P., "Combined Flow Visualization and Hot Wire Measurements in Turbulent Boundary Layers", Proc. Workshop on Coherent Structure of Turbulent Boundary Layer, C.R. Smith and D.E. Abbott, eds., Lehigh University, 1978

27. Helmig, M. and Sluijter, C.G., "Stroboscopic Recording with Television", Proceedings of the 10th International Congress on High Speed Photography, Nice, 1972

28. Johnson, R.R. and Yoo, J.K., "Experiments on the Structure of Turbulent Shear in Pipe Flows of Water", Phys. of Fluids, Vol. 19, No. 9 (1976)

29. Kim, H.T., Kline, S.J., and Reynolds, W.C., "An Experimental Study of Turbulence Production Near a Smooth Wall in a Turbulent Boundary Layer with Zero Pressure Gradient", Stanford Report, MD-20, 1968

30. Kim, H.T., Kline, S.J., and Reynolds, W.C., "The Production of Turbulence Near a Smooth Wall in a Turbulent Boundary Layer", Journal of Fluid Mech., Vol. 50, Pt. 1 (1971), pp. 133-160

31. Kline, S.J., Reynolds, W.C., Schraub, F.A., and Runstadler, P.W., "The Structure of Turbulent Boundary Layers", Journal of Fluid Mech., Vol. 30, Pt. 4 (1967), pp. 741-773

32. Kline, S.J., "The Role of Visualization in the Study of the Structure of the Turbulent Boundary Layer", Proc. Workshop on Coherent Structure of Turb. Boundary Layers, C.R. Smith and D.E. Abbott, eds., 1978

33. Kline, S.J. and Falco, R.E., "Summary of the Second Research Specialists Workshop on Coherent Structures in Turbulent Boundary Layers", Michigan State University, July 1979

34. Kreplin, A.P. and Eckelmann, H., "Propagation of Perturbations in a Viscous Sublayer and Adjacent Wall Region", J.F.M., Vol. 95, Pt. 2 (1979), pp. 305-322

35. Landahl, M.T., "Drag Reduction by Polymer Addition", Applied Mechanics, Proceedings of the 13th International Congress of Theoretical and Applied Mechanics, Moscow, August 1972, E. Becker and G.K. Mikhailow, eds., Springer-Verlag, Berlin, 1973, pp. 775-802

36. Landahl, M.T., "Wave Breakdown and Turbulence", SIAM J. Applied Mathematics, Vol. 28 (1975), p. 735

37. Landahl, M.T., "Dynamics of Boundary Layer Turbulence and the Mechanism of Drag Reduction", Phys. of Fluids, Vol. 20, No. 10, Pt. II (1977), p. 555

38. Laufer, J. and Badri Narayanan, M.A., "Mean Period of the Turbulent Production Mechanism in a Boundary Layer", Phys. of Fluids, Vol. 14, No. 1 (1971), p. 182

39. Lee, M.K., Eckelmann, H., and Hanratty, T.J., "Identification of Turbulent Wall Eddies through the Phase Relation of the Components of the Fluctuating Velocity Gradient", J.F.M., Vol. 66, Pt. 1 (1974), pp. 17-33

40. Levi, Enzo, "Eddy Production Inside Wall Layers", Journal of Hydraulic Research, Vol. 16, No. 2, pp. 107-122 (1978)

41. Lezius, Dietrich, "Water Tank Study of the Decay of Trailing Vortices", AIAA Journal, Vol. 12, No. 8 (August 1974), pp. 1065-1070

42. Loehrke, R.I. and Nagib, H.M., "Control of Free Stream Turbulence by Means of Honeycombs: A Balance Between Suppression and Generation", ASME Paper #76-FE-2, 1976

43. Morel, T., "Design of Two-Dimensional Wind Tunnel Contractions", ASME Paper #76-WA/FE-4, 1976

44. Metzler, S., "Processes in the Wall Region of a Turbulent Boundary Layer", Master's Thesis, Lehigh University, in press

45. Nagib, H., "Computer Analysis of Flow Visualization Records Obtained by Smoke-Wire Techniques", Proceedings of Dynamic Flow Conference, 1978

46. Nychas, S.G., Hershey, H.C., and Brodkey, R.S., "A Visual Study of Turbulent Shear Flow", Journal of Fluid Mech., Vol. 61, Pt. 3 (1973), pp. 513-540

47. Offen, G.R. and Kline, S.J., "Experiments on the Velocity Characteristics of 'Bursts' and on the Interactions between the Inner and Outer Regions of a Turbulent Boundary Layer", Report MD-31, Thermosciences Div., Mech. Engr. Dept., Stanford University, 1973

48. Offen, G.R. and Kline, S.J., "Combined Dye-Streak and Hydrogen Bubble Visual Observation of a Turbulent Boundary Layer", J. Fluid Mech. 62 (1974), p. 223

49. Praturi, A.K. and Brodkey, R.S., "A Stereoscopic Visual Study of Coherent Structure in Turbulent Shear Flow", Journal of Fluid Mechanics, Vol. 89, Pt. 2 (1978), pp. 251-272

50. Rao, K.N., Narasimha, R., and Badri Narayanan, M.A., "The 'Bursting' Phenomenon in a Turbulent Boundary Layer", J.F.M., Vol. 48 (1971), p. 339

51. Rubesin, M.W., "The Role of Coherent Structure in Turbulent Boundary Layer Analysis", Proc. Workshop on Coherent Structure of Turbulent Boundary Layers, C.R. Smith and D.E. Abbott, eds., 1978

52. Runstadler, P.W., Kline, S.J., and Reynolds, W.C., "An Experimental Investigation of the Flow Structure of the Turbulent Boundary Layer", Report MD-8, Stanford University, 1963

53. Schlicting, H., Boundary Layer Theory, McGraw-Hill Book Co., U.S.A., 1960

54. Schraub, F.A., Kline, S.J., et al, "Use of Hydrogen Bubbles for Quantitative Determination of Time Dependent Velocity Fields in Low Speed Water Flows", Journal of Basic Engr. (1965), pp. 429-444

55. Smith, C.R., "Visualization of Turbulent Boundary Layer Structure Using a Moving Hydrogen Bubble-Wire Probe", Proc. Workshop on Coherent Structure of Turbulent Boundary Layers, C.R. Smith and D.E. Abbott, eds., 1978

56. Smith, C.R., Huston, S.L., and Brown, J.J., "Coherent Structure of a Turbulent Boundary Layer in a Convected Reference Frame", Report for AFOSR TR-77-0093

57. Townsend, A.A., "The Structure of Turbulent Shear Flow", Cambridge University Press, London, 1956

58. Tu, B.J. and Willmarth, W.W., "An Experimental Study of Turbulence Near the Wall through Correlation Measurements in a Thick Turbulent Boundary Layer", Tech. Report #02920-3-T Dept. of Aerospace Engr., University of Michigan, 1966

59. Wallace, J., Eckelmann, H., and Brodkey, R., "The Wall Region in Turbulent Shear Flow", Journal of Fluid Mech., Vol. 54, Pt. 1 (1972), pp. 39-48

60. Wallace, J., Brodkey, R., and Eckelmann, H., "Pattern Recognized Structures in Bounded Turbulent Shear Flows", Journal of Fluid Mech., Vol. 83, Pt. 4 (1977), pp. 673-693

61. White, F.M., Viscous Fluid Flow, McGraw-Hill, U.S.A., 1974

62. Willmarth, W.W., "Structure of Turbulence in Boundary Layers", Advances in Applied Mech., Vol. 15, Acad. Press, 1975

63. Willmarth, W.W., "Survey of Multiple Sensor Measurements and Correlations in Boundary Layers", Proc. Workshop on Coherent Structure in Turbulent Boundary Layers", C.R. Smith and D.E. Abbott, eds., 1978

64. Willmarth, W.W. and Bogar, T.J., "Survey and New Measurements of the Turbulent Structure Near the Wall", Phys. of Fluids, Vol. 20, No. 10, Pt. II (1977), p. 59

65. Winant, C.D. and Browand, F.K., "Vortex Pairing: The Mechanism of Turbulent Mixing Layer Growth at Moderate Reynolds Number", Journal of Fluid Mech., Vol. 63, 1974

Appendix 1 - Sample Calculations

Calculation of Shear Velocity, u_τ

x= 370.8 cm from channel entrance

U_∞= 12.5 cm/sec

$Re_x = U_\infty x/\nu$

= (12.5 cm/sec)(370.8cm)/ 0.00994 cm^2/sec

= 4.66×10^5

$Re_\theta = 0.0142\ (Re_x)^{6/7}$

= 1020.6

$u_\tau = 0.477\ U_\infty / \ln(0.06Re_x)$ (from White, 1974)

=0.582 cm/sec

Calculation of Dimensionless Spatial Perameters

Example: y^+

y= 0.25 cm from surface

$y^+ = yu_\tau/\nu$

= (0.25 cm)(0.582 cm/sec)/(0.00994 cm^2/sec)

= 14.6

Example: D^+

The measured diameter is 2.06 cm but this is after being magnified by video system so a scale factor is obtained by calibration :

Scale factor = 12.7 cm on screen/ 2.38 cm on measuring device

= 5.3

The actual diameter, D_{act}, is:

$D_{act} = D_{meas} /$ scale factor

$= 0.39$ cm

$D^+ = Du_\tau/\nu$

$= 22.8$

This same type of calculation is applied to all other spatial variables such as x, z, etc.

Calculation of Dimensionless Vorticity

$\omega = 2\Delta\theta/t$

$= \pi$ rad/ (50 frames/ 120 frames/sec)

$= 15.1$ rad/sec

$\omega^+ = \omega\nu/ (u_\tau)^2$

$= 0.46$

Calculation of Dimensionless Time

$t^+ = tu_\tau^2/\nu$

$= 0.42$ sec $(0.582$ cm/sec$)^2/(.00994$ cm^2/sec)

$= 14.3$

APPENDIX 2

UNCERTAINTY ANALYSIS OF RESULTS

A. Introduction

A certain amount of uncertainty exists in the results due to limitations of the experimental technique. The uncertainty, σ_I, in a particular quantity can be determined from:

$$\sigma_I = \left[\Sigma\left(\frac{\partial I}{\partial_{xi}}\,\sigma_{xi}\right)^2\right]^{1/2}$$

Where σ_{xi} are the uncertainty intervals with respect to x_i.

This expression can be reduced to:

$$\frac{\sigma_I}{I} = \left[\Sigma\left(\frac{\sigma_{xi}}{xi}\right)^2\right]^{1/2}$$

B. Uncertainty in D^+

Using sequence 211 frame 2850, $D^+ = DU_\tau/\nu$

$$\text{so}\quad \frac{\sigma_{D^+}}{D^+} = \left[\left(\frac{\sigma_{Dactual}}{Dactual}\right)^2 + \left(\frac{\sigma_{u_I}}{U_\tau}\right)^2 + \left(\frac{\sigma_\nu}{\nu}\right)^2\right]^{1/2}$$

but Dact = Dmeas/scale factor(s)

$$\text{Therefore}\ \left(\frac{\sigma_{Dactual}}{Dact}\right) = \left[\left(\frac{\sigma_{Dmeas}}{Dmeas}\right)^2 + \left(\frac{\sigma_s}{S}\right)^2\right]^{1/2}$$

in this example 12.7 cm measured on the screen is actually 2.38 cm in real size so the scale factor S = 12.7 cm/2.38 cm or 5.3:1.

σ_{Dmeas} = 0.08 cm which is the smallest division on the measuring device

σ_s = 0.071 cm, the distance between scan lines on the video unit.

Therefore $\frac{\sigma_{Dact}}{D} = \left[\left(\frac{.08\ cm}{3.02\ cm}\right)^2 + \left(\frac{.071\ cm}{5.3}\right)^2\right]^{1/2}$

$= \pm 0.030$

$\frac{\sigma_{u_\tau}}{U_\tau} = \pm 0.041$ (from Metzler, 1980)

$\frac{\sigma_\nu}{\nu} = \pm 0.018$ (from Metzler, 1980)

Finally

$\frac{\sigma_{D^+}}{D^+} = \left[(0.030)^2 + (0.018)^2 + (0.041)^2\right]^{1/2}$

$= \pm 0.054$ or $\pm 5.4\%$

C. Uncertainty in ω^+

$\omega^+ = \omega\nu/U_\tau^2$

$\frac{\sigma_{\omega^+}}{\omega^+} = \left[\left(\frac{\sigma_\omega}{\omega}\right)^2 + \left(\frac{\sigma_\nu}{\nu}\right)^2 + 4\left(\frac{\sigma_{u_\tau}}{U_\tau}\right)^2\right]^{1/2}$

$\omega = \Delta\theta/\Delta t$

so $\frac{\sigma_\omega}{\omega} = \left[\left(\frac{\sigma_{\Delta\theta}}{\Delta\theta}\right)^2 + \left(\frac{\sigma_{\Delta t}}{\Delta t}\right)^2\right]^{1/2}$

$\sigma_{\Delta\theta}$ = one-half smallest division on measuring device

$= 0.13$ rad

$\frac{\sigma_{\Delta\theta}}{\Delta\theta} = \left(\frac{0.13}{\pi/2}\right) = 0.083$

Now t = # frames/120 frames/sec

$\frac{\sigma_{\Delta t}}{\Delta t} = \left[\left(\frac{\sigma\text{-\# frames}}{\text{frames}}\right)^2 + \left(\frac{\sigma\text{-frame rate}}{\text{frame rate}}\right)^2\right]^{1/2}$

σ-# frames = 0 since it is possible to stop at any frame desired.

$\frac{\sigma\text{-frame rate}}{\text{frame rate}} = \pm 0.005$ from manufacturer's specs

Therefore $\frac{\sigma_{\Delta t}}{\Delta t} = \pm 0.003$

Now $\frac{\sigma_\omega}{\omega} = \left[(0.083)^2 + (0.005)^2\right]^{1/2}$

$= \pm 0.083$

Finally $\frac{\sigma_{\omega^+}}{\omega^+} = \left[(0.083)^2 + (0.018)^2 + 4\,(0.041)^2\right]^{1/2}$

$= \pm 0.094$ or $\pm 9.4\%$

D. Uncertainty in Δz^+

Using sequence 209, frame 4553 with $\Delta z^+ = \Delta z u_\tau / \nu$

$$\frac{\sigma_{\Delta z}}{\Delta z^+} = \left[\left(\frac{\sigma_{\Delta z_{act}}}{\Delta z_{act}}\right)^2 + \left(\frac{\sigma_{U_\tau}}{U_\tau}\right)^2 + \left(\frac{\sigma_\nu}{\nu}\right)^2\right]^{1/2}$$

$$\frac{\sigma_{\Delta z_{act}}}{\Delta z_{act}} = \left[\left(\frac{\sigma_{\Delta z_{meas}}}{\Delta z_{meas}}\right)^2 + \left(\frac{\sigma_S}{S}\right)^2\right]^{1/2}$$

$$= \left[\left(\frac{0.08\ \text{cm}}{7.06\ \text{cm}}\right)^2 + (0.013)^2\right]^{1/2}$$

$$= \pm 0.017$$

Now $\frac{\sigma_{\Delta z^+}}{\Delta z^+} = \left[(0.017)^2 + (0.018)^2 + (0.041)^2\right]^{1/2}$

$= \pm 0.048$ or $\pm 4.8\%$

E. Uncertainty in Γ^+

$\Gamma^+ = \pi \omega^+ (D^+)^2/4$

$$\frac{\sigma_{\Gamma^+}}{\Gamma^+} = \left[\left(\frac{\sigma_{\omega^+}}{\omega^+}\right)^2 + 4\left(\frac{\sigma_{D^+}}{D^+}\right)^2\right]^{1/2}$$

$$= \left[(0.094)^2 + 4\,(0.054)^2\right]^{1/2}$$

$= \pm 0.108$ or $\pm 10.8\%$

APPENDIX 3 - BIOGRAPHY

The author was born on February 6, 1956 in Silver Spring, Maryland. He is the son of Myron and Phyllis Schwartz. He graduated from Lehigh University in January 1979 with a Bachelor of Science degree in Mechanical Engineering. He was accepted as a graduate student of Lehigh University in the Mechanical Engineering Department, and while there conducted research on Turbulent Boundary Layer Structure as a Research Assistant under the guidance of Dr. C. R. Smith. Presently, he is a Project Engineer in the Research and Development Department at Fuller Company in Catasauqua, Pennsylvania. He graduated from Lehigh University with a Master of Science in Mechanical Engineering on May 31, 1981.